Results From Two Studies in Seismology: I. Seismic Observations and Modeling in the Santa Clara Valley, California II. Observations and Removal of the Long-Period Noise at the Monterey Ocean Bottom Broadband Station (MOBB)

by

David Dolenc

Grad. (University of Ljubljana, Slovenia) 1995
M.S. (University of California, Berkeley) 2001

A dissertation submitted in partial satisfaction of the
requirements for the degree of
Doctor of Philosophy

in

Earth and Planetary Science

in the

GRADUATE DIVISION
of the
UNIVERSITY OF CALIFORNIA, BERKELEY

Committee in charge:

Professor Douglas S. Dreger, Chair
Professor Barbara Romanowicz
Professor Steven D. Glaser

Fall 2006

The dissertation of David Dolenc is approved:

Chair Date

Date

Date

University of California, Berkeley

Fall 2006

Results From Two Studies in Seismology:
I. Seismic Observations and Modeling in the Santa Clara Valley, California
II. Observations and Removal of the Long-Period Noise at the Monterey Ocean Bottom Broadband Station (MOBB)

Abstract

Results From Two Studies in Seismology:
I. Seismic Observations and Modeling in the Santa Clara Valley, California
II. Observations and Removal of the Long-Period Noise at the Monterey Ocean Bottom Broadband Station (MOBB)

by

David Dolenc
Doctor of Philosophy in Earth and Planetary Science

University of California at Berkeley

Professor Douglas S. Dreger, Chair

Results from two projects are presented in this work. Following brief introductory Chapter 1 that provides general background, Chapter 2 describes the influence of the Santa Clara Valley (SCV) basin structure on the propagation of teleseismic waves. Teleseismic P-waves recorded during the 1998 deployment of the 41-station seismic array are used in the analysis. Observations are compared to synthetics computed by 3D finite-difference simulations using the University of California, Berkeley (UCB) and the U.S. Geological Survey (USGS) 3D velocity models.

Chapter 3 includes further study of the ground-motion amplification in the SCV using microseisms recorded by the SCV seismic array in 1998. The obtained results are compared to the local earthquake amplification.

Chapter 4 presents results of the 3D simulations using the most recent version of the USGS velocity model for the greater San Francisco Bay Area. Results are compared to 1998 SCV seismic array observations and to simulations presented in Chapter 2.

Results presented in Chapters 2 to 4 all show strong correlations between basin depth reported in the USGS 3D seismic velocity model and different relative measures of ground motion parameters. The teleseismic, local earthquake and microseism observations are also found to be strongly correlated with one another. Since the results suggest that all three datasets are sensitive to the basin structure, they can be used to improve the 3D velocity model. I started to develop a simultaneous inversion of the teleseismic, local, and microseism observations to refine the seismic velocity model. Chapter 5 presents preliminary results and future plans.

Results from the second project are included in Chapters 6 to 9. Chapter 6 provides information about the Monterey ocean bottom broadband seismic station (MOBB). It explains why seismology is moving into the oceans, describes the MOBB location, provides details about the instruments that comprise the MOBB, and describes the deployment. Examples of data and preliminary analysis are also included.

Chapter 7 presents observations of infragravity waves at MOBB. Combined with the information from the ocean buoys, the MOBB data show that the infragravity waves in the longer than 20 s period band are mainly locally generated from shorter-period ocean waves. Two types of the observed infragravity band signal modulation are presented and possible mechanisms for the modulation are discussed. Also included is the analysis of the ocean bottom seismic data from the temporary Oregon ULF/VLF deployment that also indicates that the infragravity waves are primarily locally generated.

Chapter 8 describes analysis of data from another ocean bottom station. KEBB is located offshore Washington, in deeper water and further offshore than MOBB. Results suggests that in this case the infragravity waves are generated from shorter period ocean waves in the coastal region and not locally at KEBB.

Chapter 9 focuses on the removal of the long-period background as well as signal-generated noise from the MOBB data. Methods used to improve signal-to-noise ratio for the ocean bottom seismic data are presented.

Professor Douglas S. Dreger
Dissertation Committee Chair

To Tamara, the love of my life.

Contents

List of Figures

List of Tables

Acknowledgements

I am grateful to my committee members for their support and directions throughout my years at Berkeley. Doug Dreger was an outstanding advisor. I deeply admire Doug's work in seismology and am honored to have had a chance to learn from him. Barbara Romanowicz opened the door for me to join the MOBB project team. I am thankful to Barbara for this unique opportunity and a chance to participate in her global seismology group. I was lucky to have Steve Glaser as my outside-of-the-department committee member. His rock mechanics class was a wonderful addition to my Berkeley experience.

In addition to the work presented here, I also had a privilege to work with Bob Nadeau on the exciting discovery of the tremors on the San Andreas Fault as well as on the study of the micro-seismicity in the SAFOD target region. I thank Bob for this great opportunity.

The best thing about being a seismology student at Berkeley has been the ability to interact and learn from people in the Berkeley Seismological Laboratory. I owe a great thank you to each and everyone that was part of this team during my years at Berkeley, and especially to Bob Uhrhammer, Lind Gee, Doug Neuhauser, Pete Lombard, and Charley Paffenbarger.

In my work I used the finite-difference code E3D written by Shawn Larsen from the Lawrence Livermore National Laboratory. Shawn's help with running the E3D on different computer platforms as well as his numerous suggestions on how to better utilize the E3D code were invaluable.

My work on the MOBB ocean bottom data could not be possible without the MBARI's MOBB team that installed and maintained the MOBB station. I am in particular grateful to Paul McGill, Debra Stakes, and Tony Ramirez.

In addition, I am thankful for the funding support and generous help of the following people, without whom this work would not be possible. The Santa Clara Valley work was supported by the USGS grants 99HQGR0057 and 00HQGR0048, and was conducted at the UC Berkeley Seismological Laboratory. The Hellman Faculty Fund is acknowledged for partial support. Work was performed under the auspices of the

U.S. Department of Energy by the Lawrence Livermore National Laboratory under contract number W-7405-ENG-48. The computer simulations were performed on a 32-node Linux cluster at the UC Berkeley Seismological Laboratory and on the supercomputer Fujitsu VPP700E at the Institute of Physical and Chemical Research (RIKEN) in Japan. The UC Berkeley velocity model developed by Christiane Stidham and the USGS ver. 2 and USGS SF06 velocity models developed by the U.S. Geological Survey were used. The USGS ver. 2 velocity model was provided by Robert Jachens of the U.S. Geological Survey. Data recorded during the Santa Clara Valley seismic experiment (SCVSE) as well as instrument calibrations were made available by Allan Lindh of the U.S. Geological Survey. Propagator matrix program written by Lane Johnson of the Lawrence Berkeley National Laboratory was used to calculate the transfer function of the sedimentary layers.

The MOBB instrumentation, deployment, and maintenance were supported by the Lucile and David Packard Foundation funds to the Monterey Bay Aquarium Research Institute (MBARI), the NSF grant OCE9911392, and UC Berkeley funds to UC Berkeley Seismological Laboratory. The data from the Oregon ULF/VLF experiment were provided by Peter Bromirski of the Scripps Institution of Oceanography. The KEBB data was provided by William Wilcock and Andrew Barclay of the University of Washington and was collected with a grant from the W. M. Keck Foundation to John Delaney at the University of Washington to support prototype experiments for Project NEPTUNE, a network of interactive undersea observatories that will monitor the physical, chemical and biological processes of a single tectonic plate in the northeast Pacific Ocean. Theoretical ocean tides were computed using the program package SPOTL [*Agnew*, 1996]. I thank Michael Longuet-Higgins for directing my attention to the interaction between gravity waves and tidal currents as a possible mechanism for the observed modulation of the infragravity signal. Ocean wave data were obtained from the National Data Buoy Center.

Chapter 1

Introduction

One of the most important roles that seismology has in today's world is to identify regions of high seismic risk and provide reliable ground motion estimates for possible future events. Studies of past earthquakes and seismicity can help us identify faults, provide constraints on the size and mechanism of the expected earthquakes, and learn about the subsurface structure.

Numerous earthquakes have shown us that stronger ground motions can be expected over the basins. Slow seismic velocities of the shallow basin sediments as well as the basin structure both contribute to the trapping of the seismic energy. Seismic wave reverberations in the basin as well as focusing and interference effects of the basin edge [e.g., *Pitarka et al.*, 1996, *Kawase*, 1996] can all contribute to stronger and longer ground shaking. Santa Clara Valley (SCV) is an example of the alluvial basin. It is located south of the San Francisco Bay, under the heavily populated San Jose metropolitan area. It is surrounded by the active San Francisco, Hayward, and Calaveras faults that are all expected to generate large earthquakes in the future [*Working Group on California Earthquake Probabilities*, 2003]. It is therefore important to have a reliable velocity model of the SCV basin and the surrounding region that can be used to estimate expected amplitudes as well as duration of shaking in this area.

In the first study included in this work I investigated ground-motion amplification in the SCV using the data recorded during the 1998 Santa Clara Valley Seismic Experiment (SCVSE), a deployment of the 41 short-period seismometers. My goal was to learn more about the SCV structure using the recorded teleseismic, local earthquake, and microseism observations. I also used finite-difference code E3D to simulate some of the observations and evaluated three 3D velocity models for the region. Results showed that strong correlations exist between basin depth reported in the USGS 3D seismic velocity model and different relative measures of ground motion parameters such as teleseismic arrival delays, P-wave amplitudes, wave energy, local earthquake S-wave amplitudes, and periods of microseism horizontal to vertical spectral ratio peaks. The teleseismic, local earthquake, and microseism observations were also found to be strongly correlated with one another. The obtained empirical relationships calibrated to S-wave velocity could further be used to estimate local-earthquake S-wave amplification at new sites by temporarily deploying instrumentation to record microseism and teleseismic data. By relating new observations to a continuously operated reference station and using the empirical relationships, site-specific amplification characteristics as well as basin depth could be determined.

Since the results showed that all three datasets (teleseismic, local earthquake, and microseism) are sensitive to the basin structure, they could also be used to improve the 3D velocity model. I started to develop a simulataneous inversion of the teleseismic, local, and microseism observations to refine the USGS 3D seismic velocity. I use 3D elastic finite-difference code E3D to simulate the teleseismic, local, and microseism wavefields for the models with the increasing levels of complexity in the basins. I will use the obtained wavefields to invert for the velocity structure within the basins, while the basin geometry as defined in the USGS model is held fixed. Preliminary results with the synthetic test example and using the teleseismic data show that the procedure works and that target model is obtained within a few iterations.

The three main faults that surround the SCV are some of the most studied faults in the world. Yet there are other less known faults in the region that have produced large earthquakes in the past. One of them is San Gregorio fault that parts from the San Andreas fault outside of the San Fancisco Bay. It then runs to the south and is mainly located offshore. One of the reason why this fault is less known is because most of the smaller events are not well recorded on the distant land stations. This results in poor location and source mechanism determination for most offshore events. The only way to learn more about the offshore faults and seismicity is to install seismometers on the ocean bottom, closer to the faults on which they occur. Ocean bottom broadband stations will also help us better understand processes along all major types of oceanic plate boundaries as well as provide a global station coverage needed for the studies of global scale dynamic processes in the earth's interior.

In the second study included in this work I analyzed the long-period noise recorded at the Monterey Ocean Bottom Broadband station (MOBB) and two other ocean bottom stations located offshore Oregon and Washington. The underwater environment requires seismic station design and installation that is very different from what is used on land. One of the main challenges of extending the seismic networks into the oceans is to provide quality broadband observations at a still reasonable price. In my work I focused on the long-period noise that can be observed at the buried ocean bottom stations like MOBB. The main source of long-period noise are infragravity waves, ocean surface waves with periods longer than the wind-driven waves and the swell. I explored ways of removing this noise from the seismic observations by subtracting the coherent signals derived from the pressure measurements.

It has also been shown that the infragravity waves play a role in the generation of the Earth's hum [*Rhie & Romanowicz*, 2004; *Tanimoto*, 2005]. Earth's background free oscillations are generated in the oceans through a cascade of coupling mechanisms that involve storms, short-period ocean waves, infragravity waves, and their coupling to the seafloor. Ocean bottom stations like MOBB can be used to study the properties of the infragravity waves and should help us better understand the generation of Earth's hum.

I compared the infragravity waves signal from the three ocean bottom stations to the energy of the short-period ocean waves recorded at the local buoys. Results showed that the infragravity waves are generated from the short-period ocean waves in the nearshore region. A more detailed analysis of the infragravity waves signal observed at MOBB revealed two types of modulation. The first one is in-phase with tides which is possibly a result of the nonlinear exchange of energy between the short-period waves and tidal currents. The second one, a longer-period modulation of the infragravity signal, is found to be best correlated with the energy of the 12-14 s period ocean waves. It is interesting to note that the same period ocean waves are also the source of the microseisms noise at the double frequency, at 6-7 s [*Longuet-Higgins*, 1950].

Chapter 2

Basin structure influences on the propagation of teleseismic waves in the Santa Clara Valley, California

This chapter was published in *Bulletin of the Seismological Society of America* [*Dolenc et al.*, 2005a] with the title 'Basin structure influences on the propagation of teleseismic waves in the Santa Clara Valley, California'.

Summary

We have investigated ground-motion amplification in the Santa Clara Valley (SCV) using teleseismic P waves observed during the 1998 deployment of 41 short-period seismometers. The Santa Clara Valley Seismic Experiment (SCVSE), [*Lindh et al.*, 1999; *Fletcher et al.*, 2003] recorded many local and regional earthquakes, as well as seven large (M_W>6.4) teleseisms. Measured teleseismic P-wave arrival-time delays, relative P-wave amplification, and P-wave energy were used in the analysis. The relative P-wave amplification is found to correlate strongly with the arrival-time delays. In addition, the P-wave energy is found to correlate with the observed teleseismic delays. We also compared observed P-wave arrival-time delays and P-wave amplification with synthetics computed by using 3D finite-difference simulations of the teleseismic wave field to model these parameters using both the University of California, Berkeley (UCB) [*Stidham et al.*, 1999; *Stidham*, 1999] and the U.S. Geological Survey (USGS) [*Brocher et al.*, 1997; *Jachens et al.*, 1997] 3D velocity models. The results indicate that arrival-time delays on the order of ±0.25 sec correlate strongly with the reported basin depths in the two models. We find that the correlation between the arrival-time delays and basin depth is strongest for the USGS model. However, the UCB velocity model yields wave amplification that better matches the data. The finite-difference simulations indicate that, in general, the observations may be reproduced by either of the 3D velocity models, although refinements to the proposed 3D structure for the SCV are needed.

2.1 Introduction

The Santa Clara Valley (SCV) is an alluvial basin located south of the San Francisco Bay. It includes two elongated basins, the Cupertino basin in the west and the Evergreen basin in the east. The sediments overlaying the Franciscan basement are mainly Pliocene to Quaternary alluvial gravels and sands [*Wentworth et al.*, 1997]. The proximity of the SCV to the active San Andreas, Hayward, Calaveras, Sargent, and Rodgers Creek faults, and its location beneath the heavily populated San Jose metropolitan area, have resulted in an increased interest to better delineate the SCV structure. Several studies have focused on the hazard associated with the two elongated and possibly deep basins. Studies by *Frankel and Vidale* [1992], *Stidham et al.*, [1999], *Stidham* [1999], *Frankel et al.*, [2001], *Hartzell et al.*, [2001], and *Fletcher et al.*, [2003] are all examples of these efforts. Using a 3D velocity model of the region, *Stidham et al.* [1999] successfully modeled the strong-motion wave field of the 1989 Loma Prieta earthquake. However, one of the concerns raised by the study was the limited sampling of sites located over the SCV. *Stidham* [1999], in her thesis work, examined several 3D velocity models in the simulation of small to moderate local earthquakes. These studies demonstrated the sensitivity of the synthetic seismograms to basin heterogeneity, to the velocity contrasts across the major strike-slip faults of the region, and to the deep crustal structure.

To address some of these concerns, the Santa Clara Valley Seismic Experiment (SCVSE) was carried out by the U.S. Geological Survey (USGS), University of California, Berkeley (UCB), and Incorporated Research Institutions for Seismology Program for Array Seismic Studies of Continental Lithosphere (IRIS PASSCAL). In the experiment, 41 seismic stations were deployed across the SCV from June through November 1998 (Fig. 2.1). The array recorded a number of local, regional and teleseismic earthquakes. Seven of the teleseismic events (Table 2.1, Fig. 2.2) had high signal-to-noise levels, allowing detailed analysis.

Teleseismic waves are well suited to investigating 3D details of a local velocity structure as previous studies in the Salt Lake Basin [*Olsen & Schuster*, 1995; *Olsen et al.*, 1995] and observations in the Seattle basin [*Pratt et al.*, 2003] have shown. Because the distance from the event is large compared with the aperture of the array, the seismic wave field is essentially uniform as it arrives beneath the region of study. The source contributions and the near-source and mantle-travel paths are also essentially the same for all the SCV stations. We may therefore assume that the differences in the observed teleseismic waveforms are caused by differences in crustal structure beneath the recording array.

In this paper we present results of analyses of teleseismic P-wave arrival-time delays, relative P-wave amplification, P-wave energy, seismic waveforms, and basin converted arrivals with the objective of testing proposed 3D velocity models for the SCV region and to determine whether the teleseismic wave field can delineate 3D basin structure to use as a basis for improving velocity models.

2.2 Data Processing

The locations of the SCVSE seismic stations we use are shown in Figure 2.3. The stations provided good coverage of the SCV. All the stations except station 160 were situated on SCV alluvium. Station 160, in the eastern part of the Evergreen basin, was placed on Mesozoic rocks. Station MHC, a permanent station of the Berkeley Digital Seismic Network (BDSN) located on hard Mesozoic rocks east of the SCV, was used in addition to SCVSE seismic stations as a reference hard-rock site. None of the SCVSE seismic stations were located in the San Francisco Bay mud.

Mark Products L-22D seismometers with 2-Hz natural frequency from the USGS and IRIS PASSCAL as well as L-4C seismometers with 1-Hz natural frequency from the USGS were used together with three-channel 24-bit RefTek 72a-07s recorders. Global Positioning System (GPS) receivers were connected to the recorders to keep the internal clock accurate. Data were sampled continuously at 50 Hz. The USGS instruments have been individually calibrated and the measured parameters should be accurate to within ±5%. For the PASSCAL instruments, nominal values were used, which were accurate to within 15% [*Lindh et al.*, 1999]. For the analysis, the vertical-component ground-velocity records were processed by deconvolving the reported instrument-response parameters [*Lindh et al.*, 1999] and filtering between 0.1 to 0.5 Hz using a four-pole acausal Butterworth bandpass filter. We found that the short-period instruments recorded the teleseismic P waves with excellent signal-to-noise ratios to a minimum frequency of 0.1 Hz. S waves were not well recorded because of the limited instrument response. The low-pass filter was applied to remove the higher frequency cultural noise from the urban environment.

2.3 Observations

For a given event, the waveforms can differ greatly at the stations of the array. Figure 2.4 illustrates the differences in the amplification of the initial P-wave and in the development of the P-wave coda at four sites. Station 120 was located over the Cupertino basin, station 238 over the deep part of the Evergreen basin, and station 186 south of the Cupertino basin (see Fig. 2.3). In each case the record from station PG2, located on the bedrock ridge between the two SCV basins, is shown for comparison. The station 186 record is very similar to that of PG2. The amplitudes of their first P-wave arrivals are almost identical and they both lack the large-amplitude, extended coda wave field observed at stations 120 and 238.

For the analysis, we made measurements on the teleseismic data that included P-wave arrival times, amplitudes of the initial P waves, and P-wave energy. We first measured the relative P-wave arrival-time delays across the SCV in which arrival-time delays are with respect to a reference station assumed to be located outside the basins. Although essentially the same results were obtained by using stations MHC or 186 as a reference, in the following we use station 186 as it is one of the SCV array stations. P-wave amplitudes on station 186 were consistently small, the P-wave coda short, and both the UCB and USGS velocity models agree that it is located outside the SCV basins. Station 160 was an alternative candidate for a reference station, as it was the only SCV array station located on rock. We rejected it since the Evergreen basin extends to the east of it in both models.

The arrival times were determined by cross-correlating the first quarter-cycle of the initial P waveform. Nearly identical results were obtained using the first half-cyle, and very similar results were obtained when the entire P waveform was cross-correlated. A planar trend in arrival time was then fit to the data and removed, giving the travel-time residual for each station. The residuals for event 4 clearly outline the deep basins and intervening bedrock ridge (Fig. 2.5a). The range in the arrival-time delays is ±0.25 sec, in which the positive delays correspond to later arriving P waves. The P-wave amplification with respect to station 186 also correlates with the SCV structure (Fig. 2.5b). The range in P-wave amplification is found to be from 0.8 to approximately 1.5 with respect to station 186. Similar results were obtained for all seven events.

2.4 UCB and USGS version 2 velocity and density models

The UCB and the USGS models cover the area from the latitude of Monterey, California to just north of San Pablo Bay, and from the Pacific coast to the Great Valley in the east. The USGS model has P- and S-wave velocity and density defined at each point within the model, and the UCB model has the three variables parameterized. Figure 2.6 shows cross sections of the two models along the lines A, B, and C indicated in Figure 2.3.

The UCB model [*Stidham*, 1999; *Stidham et al.*, 1999] was created as a simple model that incorporates the main geologic blocks present in the wider San Francisco Bay area. In addition to shallow alluvial basins, it includes velocity contrasts across the strike-slip faults. The bedrock consists of layers that vary with depth in the upper crust and are homogeneous below a midcrustal discontinuity located at 17 km depth [*Jachens et al.*, 1995]. The depth of the midcrustal reflector and of the Moho were taken from the BASIX study [*Brocher et al.*, 1994] and from broadband waveform modeling [*Dreger & Romanowicz*, 1994]. The extent of alluvium in the model was determined from seismic reflection studies and from the borehole and gravity surveys. In the SCV region, depth to the bedrock was determined mainly by the interpretation of gravity anomalies. The slowest shear wave velocity in the model is 1 km/sec and the model does not include topography.

The USGS model used in this study is the second revision of the San Francisco Bay area 3D velocity model [*Brocher et al.*, 1997; *Jachens et al.*, 1997] developed by Jachens and others at the USGS from a careful conversion of known geology into seismic velocity and density. The model extends to 28.5 km depth and includes the mafic lower crust and the mantle. It was constructed by using surface geology, gravity inversion data, seismic refraction data, and borehole logs. It also does not include topography. Although the basins may extend deeper than 6 km, the authors assumed that below this depth the seismic velocities are indistinguishable from those of the basement. Version 2 of the model incorporates velocity contrasts across the faults. The model grid spacing in the upper 625 m is 125 m. At intermediate depths, down to 6 km, the grid spacing is 250 meters. From there to the deepest extent of the model, 28.5 km, grid points are 500 m apart. The slowest shear-wave velocity in the model is 83 m/s.

The basin depths in the UCB model are well defined contrasts between the uniform basin velocities and the faster bedrock (Fig. 2.6). The basin depths for the USGS model were determined by comparing the velocity and density of the vertical profile at each site to the vertical profile of a non-basin site. The depth at which there is no difference in P- and S-wave velocity and density was taken as the basin depth.

The UCB and the USGS model cross sections are shown in Figure 2.6. The structure around and under the basins is similar in both models and they both have bedrock velocity gradients. The deep structure in the two models is also very similar.

Some of the more important differences between the two models are as follows. The

UCB model has uniform P- and S-wave velocities (1.75 and 1 km/sec), and density ($2g/cm^3$) within the basins. The USGS model has basin velocities and density that increase with depth. In the UCB model the maximum basin depth is 2 km in the eastern and 1.5 km in the western basin. In the USGS model the maximum basin depth is 6.5 km in the eastern and 4.5 km in the western basin. Although the basins in the USGS model are much deeper, the regions with slow velocities are shallow and their depths are comparable to the UCB model. The deepest grid layer in the USGS model that includes S-wave velocities slower or equal to 1 km/sec, is at 1.5 km depth. By this measure, the basins in the USGS model are shallower than in the UCB model. In the UCB model the two basins have a very simple geometry. In the USGS model the two basins have an irregular shape, which is a result of the gravity inversion mapped into the model. In the UCB model the western basin does not extend as far south as it does in the USGS model, and in the UCB model the Cupertino and Evergreen basins are not as wide as in the USGS model.

The UCB model was designed for use with the E3D finite-difference code [*Stidham et al.*, 1999] and no changes were made to the model for the purpose of this study. Before the USGS model was used with the finite-difference code, the top section of the model was resampled and the bottom section of the model was interpolated to a uniform 250-m grid spacing. Because the surface layer was not yet available when we began our study, the layer at 125 m was used as the surface layer. Because of computational limitations, the slowest velocities in the model were increased to a minimum S-wave velocity 1 km/sec. The slowest P-wave velocity was 1.75 km/sec. The velocity increases affected the model down to 1.5 km depth. A high-resolution run was also performed in which the grid spacing was 125 m and the slowest P- and S-wave velocities were 0.9 and 0.52 km/sec, respectively, affecting the model to a depth of 250 m.

2.5 Modeling

Although a ray approach could be used efficiently for the purpose of estimating arrival-time delays and P-wave amplitudes, we used an elastic finite-difference technique to calculate synthetic waveforms because of our interest in modeling converted arrivals, which are seen to contribute significantly to the observed seismic waveforms (see Fig. 2.4).

The elastic finite-difference code E3D [*Larsen & Schultz*, 1995] used in this study is accurate to the fourth order in space and to the second order in time. It utilizes a regularly spaced grid that is staggered in both space and time for the six-component stress and three-component velocity fields. Stress-free surface conditions and absorbing boundary conditions [*Clayton & Engquist*, 1977] were used, and a 'sponge' boundary layer [*Cerjan et al.*, 1985] was applied to minimize reflections from the model boundaries. Attenuation and topography were not included in the modeling.

Most of the modeling was performed using a 250-m grid spacing and a minimum shear-wave velocity of 1 km/sec. At five grid points per wavelength, frequencies up to 0.8 Hz were simulated with minimal grid-dispersion effects [*Lavander*, 1988]. In our analysis we compared simulations and observations in the 0.1- to 0.5-Hz passband. At 0.5 Hz maximum frequency there are eight grid points per wavelength giving greater accuracy. We performed a high resolution run in which the grid spacing was reduced to 125 m, giving 16 grid points per wavelength at 0.5-Hz maximum frequency. The synthetics from the 250-m and 125-m grid runs were nearly identical in 0.1- to 0.5 Hz-passband.

The size of the largest model was 115 × 115 × 80 km with more than 67.0×10^6 grid points. Each simulation required approximately 3.5 GB of memory. To examine the importance of the slow velocities defined in the USGS model, we calculated a few high-resolution simulations with 125-m grid spacing and minimum P- and S-wave velocities of 900 and 520 m/sec. The model for the high-resolution runs had more than 536.0×10^6 grid points, and required approximately 28 GB of memory.

Most of the computations were performed on the vector parallel supercomputer Fujitsu VPP700E (32 processors, 64-GB memory) at the Institute of Physical and Chemical Research (RIKEN) in Japan. A typical run using a 250-m grid spacing was completed in 1 hr. Smaller models and shorter test runs were calculated on a Sun Enterprise 3000 computer (3 processors, 4.75-GB memory) at the Berkeley Seismological Laboratory.

To model the plane wave from the teleseismic events, we used a disc of point sources spaced 1.25 km apart in the deepest homogeneous layer of the velocity model, representing the upper mantle. The time history for each compressional point source had a Gaussian pulse shape. For each event the disc was oriented in space to have the backazimuth and incident angle of the incoming P wave. By modeling the plane orientation with a horizontal layer of sources delayed in time, we were able to decrease the model depth to 40 km, reducing memory requirements and calculation time. Although the boundaries were absorbing, they still reflected some energy, resulting in undesirable late arrivals, mainly because some of the sources used to simulate the plane wave were close to the model boundaries. In the modeling, care was taken to reduce late arrivals by increasing the model dimensions, tapering the point sources, and using a few grid-point thick 'sponge' boundary layer [*Cerjan et al.*, 1985]. The maximum amplitudes of the late arrivals that were due to the finite model dimensions and the finiteness of the approximated plane wave were estimated by simulations using a homogeneous model of the same dimensions and were found to be less than 15% of the first pulse (Fig. 2.7).

2.6 Results

2.6.1 P-wave arrival delays, amplification, and energy

All seven teleseismic events were forward modeled with the E3D code with both the UCB and the USGS models. The measured travel-time residuals and relative amplitudes at all stations show only small variations between the individual events leading to the conclusion that the orientation of the incoming plane wave has little influence on basin response. The results for both the observed and the simulated travel-time residuals averaged over all events are presented in Figure 2.8a, where panels A, B, and C correspond to the sections indicated in Figure 2.3. The measurements made on the synthetics were obtained in the same manner as in the observations. The mean values and standard deviations using the seven events are given for each station as a function of the distance across the SCV. The results for the observed and simulated amplitude analyses are presented in Figure 2.8b. The observations show that average amplitude on station 238, located over the Evergreen basin, is 46% larger than the observed amplitude at station PG2 that was located between the two basins. Average amplitude at station 120, located over the Cupertino basin, is 54% larger than at station PG2.

The sinusoidal signal across the basins and basement ridge is observed in both the data and the synthetics, for travel-time residuals as well as amplitudes. However, the observed data (gray) has larger variance than the synthetics. This means that parameters other than angle of incidence and azimuth have a significant impact on site response. This might be caused by large-scale structure in the lower crust or Moho or by unknown point scatterers in the actual earth.

On the one hand, UCB model matches the observations better because it has larger overall variation and range in the amplitudes and travel-time residuals. On the other hand, the shape of the observed time residuals in the northeast and the southwest corners of the cross section B is better captured by the USGS model (see Fig. 2.8a, panel B). This indicates that the Evergreen and the Cupertino basin may be wider than currently modeled in the UCB model. The USGS model matches better the width of the negative time residuals presented in the middle part of the cross section B, suggesting that the ridge between the two basins is wider than assumed by the UCB model. The variations in time residuals in the southwest edge of cross section C are better matched by the USGS model, in which the Cupertino basin extends further to the south than in the UCB model.

The average time residuals for all of the teleseismic events as a function of basin depth in the USGS and the UCB model are presented in Figure 2.9a,b. For both models positive delays correlate with greater basin depth. The USGS model with a more detailed basin geometry produces a more systematic and superior correlation of basin depth and P-wave arrival-time delay. The time residuals for the USGS model increase with increasing basin depth until about 2 km depth. Then, as the depth increases, the travel-time residuals remain more or less the same. This indicates that the slow velocities in the shallow layers contribute most to the delay. Although the basins are deep, the velocity at depth is very similar to that of the neighboring bedrock, so it has little influence on the travel time. For the UCB model the scatter is much larger, which is likely because of the relatively coarse structure of the model, but a correlation with depth can still be observed as the data and synthetics for the stations located above the basin deeper than 0.8 km show an increase in the travel-times residuals (Fig. 2.9b).

The relative amplification for the seven events as a function of basin depth in the USGS and the UCB model is presented in Figure 2.9c,d. In this case, the general trend with greater basin depth is not as clear as it was for the travel-time residuals. The correlation between the modeled P-wave amplitude and basin depth for the UCB model is seen to be good for depths less than 600 m, and for greater depths the average amplification is seen to be flat. For the USGS model the range of the modeled P-wave amplifications is much smaller, as already seen in Figure 2.8b. The correlation between the modeled P-wave amplitude and the USGS model basin depth can be seen for depths less than 1.8 km, but is much less pronounced than for the UCB model. This is because of continuous reduction in velocity throughout the basins in the USGS model. The UCB model, on the other hand, has a strong impedance contrast between the basin and the basement.

To investigate the importance of the slow velocities in the USGS model, we performed a few high-resolution runs with 125-m grid spacing and minimum P- and S-wave velocities of 900 and 520 m/sec [*Dolenc*, 2001]. This changed the travel-time residuals only slightly (average change was 0.01 sec), because the inclusion of slower velocities affected only the top three grid points. In general, the relative amplitudes increased; however, the increased amplification did not account for the observations (average change was 2.4%). This indicates that the peak values, measured at relatively long periods ($T > 2sec$), are largely unaffected by the very slow shallow structure and that to the first order they are sensitive to the basin/basement impedance contrast and the basin geometry.

Judging by results from the study of travel-time residuals the spatial extent and basin geometry of the USGS model is superior. However, a comparison of the relative amplitude shows that the USGS model does not explain the range of observed amplifications. The UCB model seems to explain the relative P-wave amplification reasonably well. The relative amplification increases from zero to 600 m basin depth, at which point it is fairly constant (see results for UCB model in Fig. 2.9d). This is expected because the basins in the UCB model have a constant velocity and the basin/basement impedance is therefore also fairly constant. Thus the increase in amplification for small basin depths ($< 600m$) must be a basin edge effect. Over the deepest parts of the basin, the amplification is caused entirely by the basin/basement impedance contrast because there is no internal amplification in the basin. Finally, the spatial correlation of time residuals agrees better with the USGS model, and, therefore, revisions to the SCV velocity model should start with the basin geometry specified in the USGS model, with perhaps a less pronounced internal basin velocity gradient.

To measure the energy of the incoming P wave, we squared and integrated 120 sec of the vertical waveforms after the P-wave arrival at each station. Figure 2.10 shows the ratio of the P-wave energy at each station to that at station 186, averaged over all seven teleseismic events. The correlation between the increased wave energy and the outline of the Cupertino and the Evergreen basin in the USGS model is excellent. The intervening bedrock ridge also shows up prominently with lower levels of P-wave energy. The average for the seven events is shown because no systematic variation in P-wave energy with respect to event backazimuth and incident angle of the primary P wave was observed [*Dolenc*, 2001]. Station 238, located over the Evergreen basin, shows a 228% increase in energy relative to station PG2 that was located between the two basins. Station 120, located over the Cupertino basin, shows a 267% increase in energy relative to station PG2.

Figure 2.11 compares the USGS basin depth, UCB basin depth, P-wave amplification, and P-wave energy, all as functions of the observed teleseismic P-wave arrival-time delay. The bottom two panels in Figure 2.11 compare just the observations and do not use any information from the two models. For the teleseismic observations the results for the seven events were averaged. The basin uncertainty is shown as 20% of the basin depth. This value is given for the USGS model [*Jachens et al.*, 1997] and is used for the UCB model. Figure 2.11 demonstrates the correlation of all the observables with respect to the reported basin depth, which suggests that the teleseismic observations may be used to refine basin structure. It also suggests that it may be possible to deduce site amplification characteristics that are applicable to local earthquake basin excitation from the observed teleseismic arrival-time delay and relative amplitude.

The correlations also allow for regressions to obtain equations to predict time residuals, relative amplitudes, and relative P-wave energy. Figure 2.12. shows the observed values averaged over the seven teleseismic events as a function of the USGS model basin depth. Stations located above the basin that was shallower than 3 km show a linear relationship between the observed variables and the basin depth. The obtained linear equations fit reasonably well as indicated by the R^2 values. Coefficients of the line fit and their standard errors are included in Figure 2.12.

2.6.2 Waveform modeling

So far we only used synthetic waveforms to model P-wave arrival-time delay, amplitude, and energy. In the next section we focus on the waveform comparison. The synthetic and recorded waveforms for event 4 at stations 120, 238, 186, and PG2 are presented in Figure 2.13. Event 4 was selected because the beginning of the record is simple with strong and clear P- and pP-wave arrivals.

The instrument response has been removed and the waveforms have been bandpass filtered between 0.1 and 0.5 Hz with an acausal, 4-pole Butterworth filter. The synthetics were constructed by summing the primary P-wave response with the pP-wave response. The pP-delay time and relative amplification of -1.4 measured at station MHC were used to scale the synthetics. Final synthetics for all the stations were shifted by the same time, and the amplitudes for all stations were scaled by the same amount so that the P-wave arrivals for station 186 coincided for data and synthetics. Thus, the comparison between the observations and synthetics for stations other than 186 demonstrate model predictions in terms of both time and amplitude. The synthetics agree with the data in terms of amplification and coda generation, but good phase agreement of later arrivals was not possible at all stations. However, phase agreement with the first arrival is very good. Considering that the synthetics are computed solely from the basin response to incident P and pP, the agreement is quite remarkable.

The waveforms show similarities based on location. Shown are representative stations of the two basins, the region outside the basins, and the ridge in between the basins.

Station 120 was located over the Cupertino basin in the UCB as well as in the USGS model. The observations show amplification of the P and pP phase as well as large-amplitude P-wave coda. These observations are better matched with the UCB model synthetics.

Station 238, located over the Evergreen basin, shows large observed P- and pP-wave amplifications and P-wave coda amplitudes. Overall, the UCB synthetics model the observed waveforms much better.

Station 186 was located outside the Cupertino basin in both models. The observations and synthetics from both models are simple and agree in terms of small P-wave amplifications and P-wave coda amplitudes.

Station PG2, located between the two basins in both models, shows small amplitudes that are well modeled by both velocity models. The observed P-wave coda amplitudes are larger then predicted by the two velocity models.

The data recorded at stations above the basins (e.g., stations 120 and 238 in Fig. 2.13) show strong converted arrivals between the P and pP waves. These phases are also present in the UCB model synthetics but are much smaller when the USGS model is used. The time delay of the first converted arrival following the P wave on station 120 is 4 sec.

To estimate travel-time delays for some of the converted arrivals, we used a cross-section of the UCB model across the SCV through station 120 and an incident P-wave perpendicular to the basin bottom (Fig. 2.14). In the UCB model, the depth of the basin under station 120 is $h = 1.4km$, and the dip of the Cupertino basin in the west is $\alpha = 16.3^o$. The results listed in Table 2.2 indicate that candidate phases for the first converted arrival observed in the data and in the UCB synthetics include PsSSS, PsPSS, and PpSSS.

The UCB model synthetics better match the observed converted arrivals. This suggests that a sharp basin/bedrock velocity contrast that is present in the UCB model is needed to explain the observations. Observations of converted arrivals in the data and the UCB model synthetics indicate that basin-induced converted arrivals could further be used to estimate the sediments thickness. A study by *Chen et al.* [1996] showed that in the case of a wide basin with little lateral variations, S to P converted waves could be used to determine sediments thickness and average shear-wave velocity.

Figure 2.15 shows the observed waveforms (top) for event 4 recorded on stations 120, 238, 186, and PG2. Shown below are the synthetics calculated by using the UCB model and its variations. From top to bottom they are: the original UCB model, an increase in the P-wave velocity in the basins by 25%, an increase in the S-wave velocity in the basins by 25%, and the UCB model without the basins. The synthetics were constructed as described for Figure 2.13.

The results show that the synthetics obtained with the original UCB model best match the observations. The 25% P-wave velocity increase in the basins resulted in smaller amplitudes of the secondary arrivals. The 25% S-wave velocity increase in the basins had a similar effect, but it reduced even further the amplitudes of the late arrivals. As expected the UCB model with the SCV basins removed (bottom) resulted in simple waveforms at all stations. Only increases in wave velocity were examined as decreasing seismic velocities in the model would greatly increase memory requirements while maintaining the same maximum computed frequency of the synthetic seismograms.

2.7 Conclusions

Our analysis of the teleseismic P waves of seven events recorded by the SCVSE demonstrates the influence of the SCV basins on the timing and amplitudes of primary arrivals, and on the generation of a converted wave field. Observed P-wave arrival-time delays are on the order of $\pm 0.25 sec$ and show the spatial extent of the basins. These arrival-time delays were found to correlate strongly with other observations such as primary P-wave amplification (Fig. 2.11c) and seismic wave energy (Fig. 2.11d). In fact, a companion paper investigating microseism amplification and dominant period [*Dolenc & Dreger*, 2005] reveals that these observations are also strongly correlated to the teleseismic arrival-time delays. This diverse data set is strongly influenced by basin structure and indicating that it may be used to invert for refined seismic velocity models.

We also find that the arrival-time delays are correlated with the basin depth as specified in the two 3D seismic velocity models proposed for the region (Figs. 2.11a,b). The correlation is better for the USGS model. Simulated P-wave fields match these observations but, at the same time, indicate that additional modeling is needed to explain the full range of the observations. For example, the spatial correlations indicate that the geometry of the USGS model is superior in terms of the southern extent of the western Cupertino basin, the eastern extent of the eastern Evergreen basin, and the structure of the bedrock ridge between the two deep basins. However, the spatially simpler UCB model tends to explain the primary P-wave amplification and converted arrivals better, which appears to be caused by the sharp contrast between basin and basement seismic wave velocity in that model. These results suggest that future work should focus on using the USGS basin geometry with a less strong internal velocity gradient and a sharp internal interface to produce strong converted arrivals.

The teleseismic observations presented in this article and the empirical relationships that have been obtained between the observables and basin depth may be combined with similar empirical relationships for microseism observables and local earthquake low-frequency ($f < 0.3 Hz$) S-wave amplification characteristics. This is described in *Dolenc and Dreger* [2005]. With such relationships calibrated to S-wave amplification it will be possible to estimate local-earthquake S-wave amplification at new sites by temporarily deploying instrumentation to record microseism and teleseismic data.

Relating such new observations to a continuously operated reference station (e.g., MHC for the SCV) offers hope that it will be possible to identify site-specific amplification characteristics relatively easily and also interpolate basin structure using the empirically determined relationships.

Table 2.1: List of the selected teleseismic events from the Harvard Moment Tensor catalog.

Event No.	Region	Lat.	Lon.	Date (mm/dd)	Time	M_W	Depth (km)
1	Kermadec Islands	-30.51	-178.71	07/09	14:45:49	6.9	154
2	Santa Cruz Islands	-10.91	166.09	07/16	11:56:42	7.0	100
4	Near Coast of Central Chile	-32.30	-71.67	07/29	07:14:29	6.4	58
6	Near Coast of Ecuador	-0.57	-80.48	08/04	18:59:29	7.1	26
7	Bonin Islands Region	28.99	139.47	08/20	06:41:10	7.1	426
8	Off Coast of Central America	11.58	-88.55	08/23	13:57:17	6.7	15
10	Near Coast of Central Chile	-29.56	-71.97	09/03	17:38:05	6.5	34

Table 2.2: Travel-time delays for some of the converted arrivals relative to P wave at station 120. UCB model cross section across the SCV was used in the calculation (see Fig. 2.14).

Phase	dt (sec)	Phase	dt (sec)
PpP	1.3	PpPPP	1.9
PpS	1.9	PpPPS	2.8
PsP	1.7	PpPSS	3.3
PsS	2.4	PsPPS	2.9
		PpSSS	3.6
		PsPSS	3.5
		PsSSS	3.8

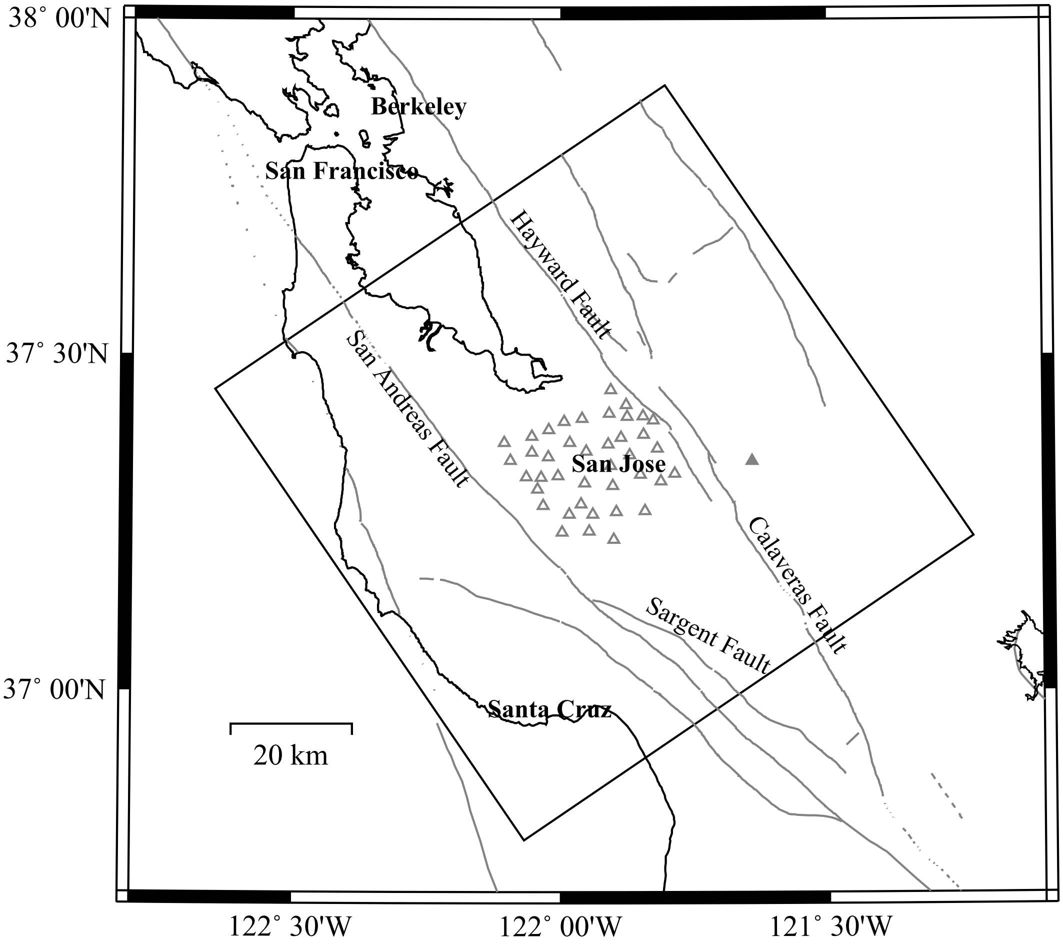

Figure 2.1: Location of the temporary SCV seismic array south of the San Francisco Bay. Open triangles indicate SCVSE seismic stations and the filled triangle indicates permanent station MHC of the Berkeley Digital Seismic Network. The box shows the size of the model used in the E3D finite-difference simulations. Gray lines are the active faults in the region.

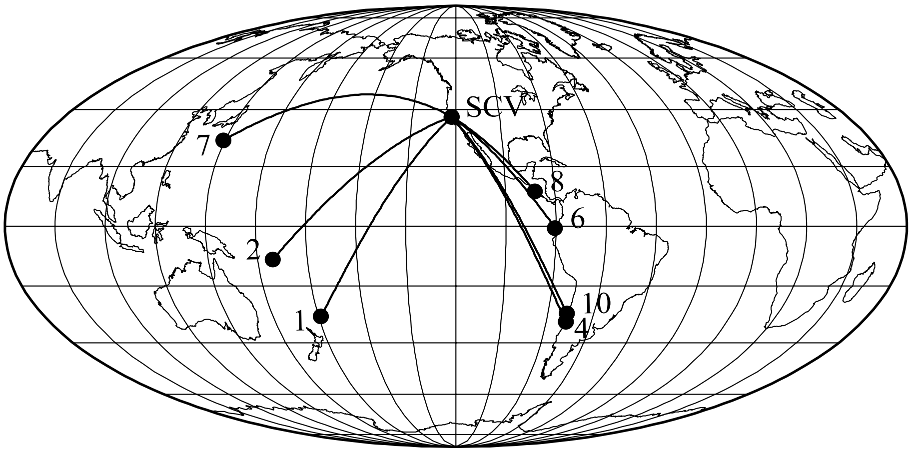

Figure 2.2: Locations of the teleseismic events used in this study.

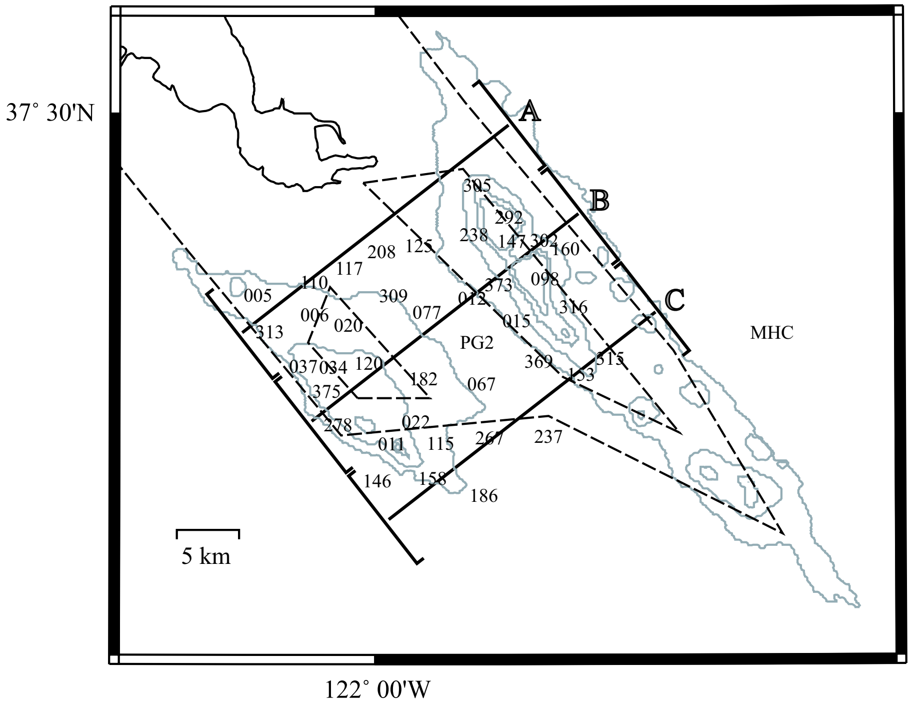

Figure 2.3: Closer look at the SCV region. Numbers indicate SCVSE seismic stations. Dashed lines denote the contours of the basins from the UCB model at the surface and at the 1-km depth. Contours of the basins from the USGS model at 1 km, 3 km, 5 km, and 6 km depth are shown in gray. The region of interest was divided into sections A, B, and C. The UCB and the USGS velocity model cross sections along lines A, B, and C are shown in Figure 2.6.

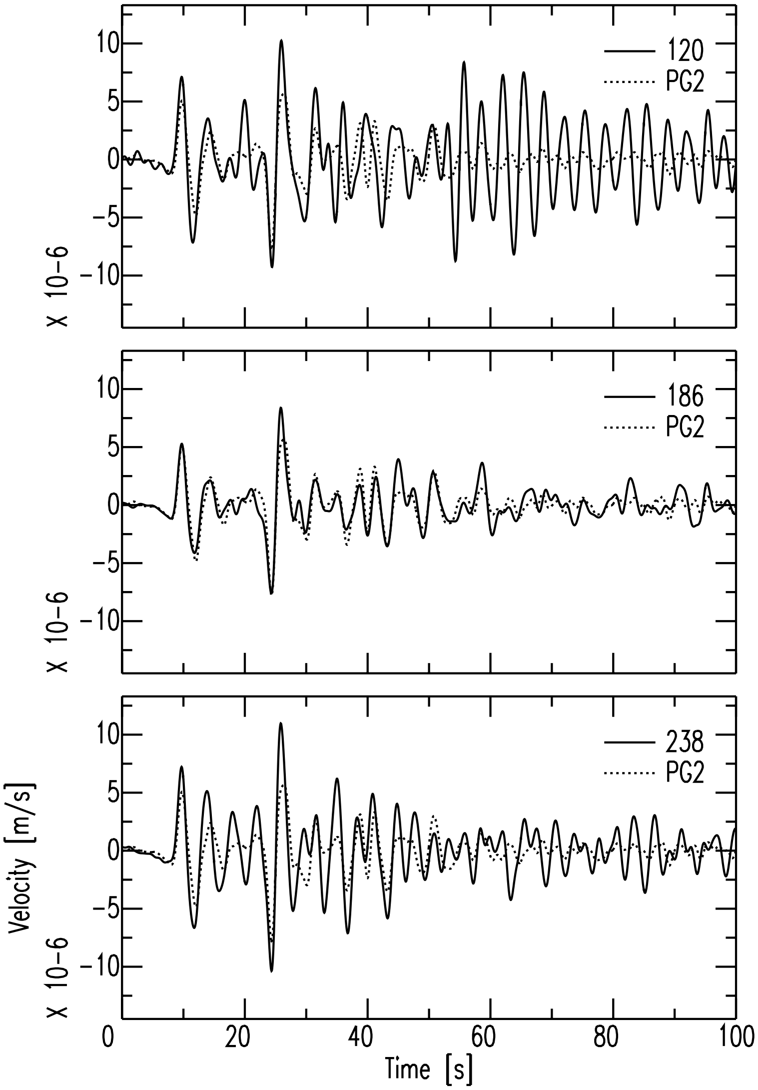

Figure 2.4: Vertical velocity seismograms for event 4 recorded on the SCV stations 120, 186, and 238. Also shown in all three panels is station PG2 (dotted). The first arrival is a P wave followed by a pP wave about 15 sec later. See Figure 2.3 for station locations.

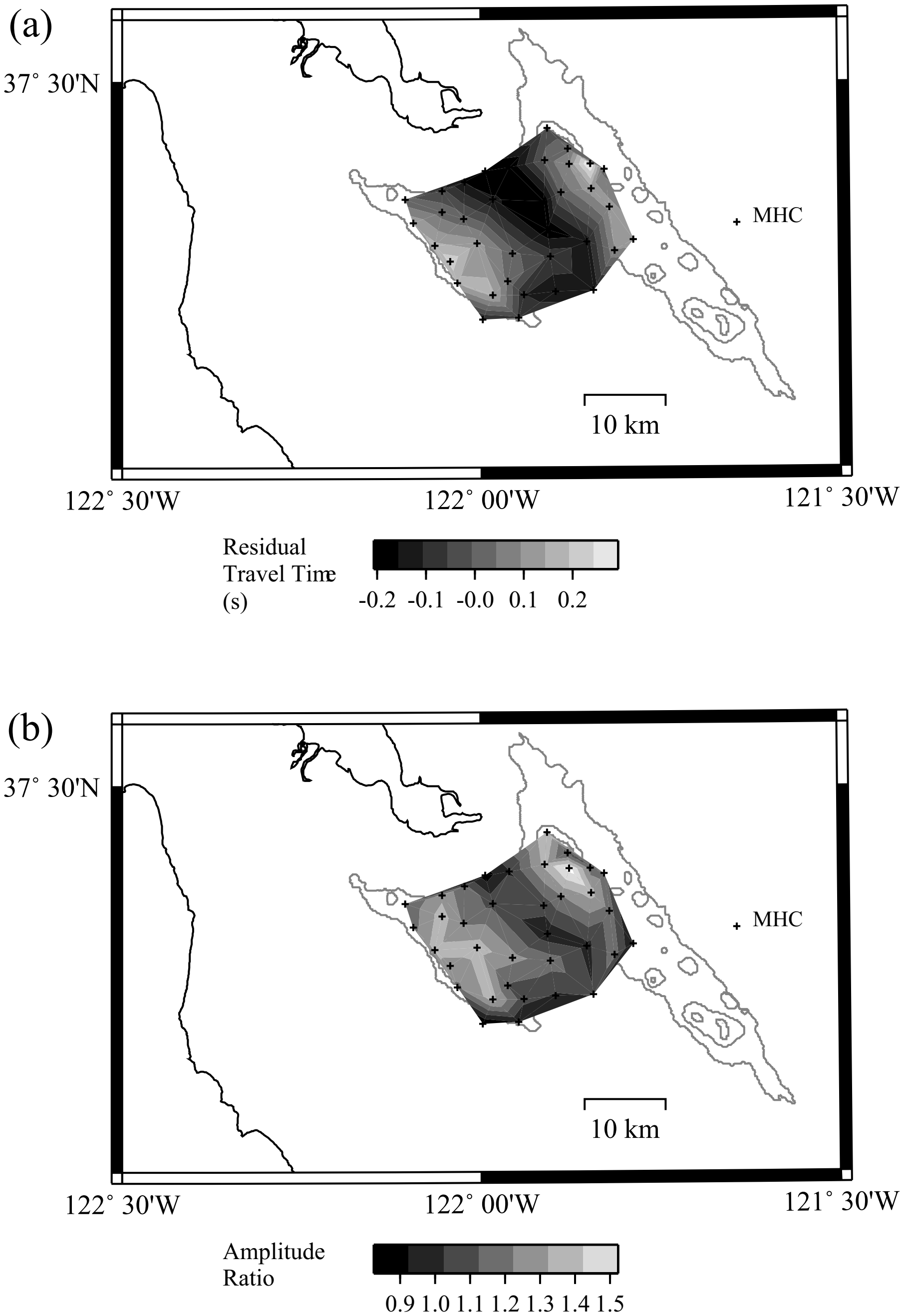

Figure 2.5: (a) Observed P-wave residuals for the event 4. (b) Observed P-wave amplitudes for the event 4 relative to reference station 186. Station 186 was located south of the Cupertino basin (see Fig. 2.3). Contours of the basins from the USGS model at 1 km, 3 km, 5 km, and 6 km depth are shown in gray.

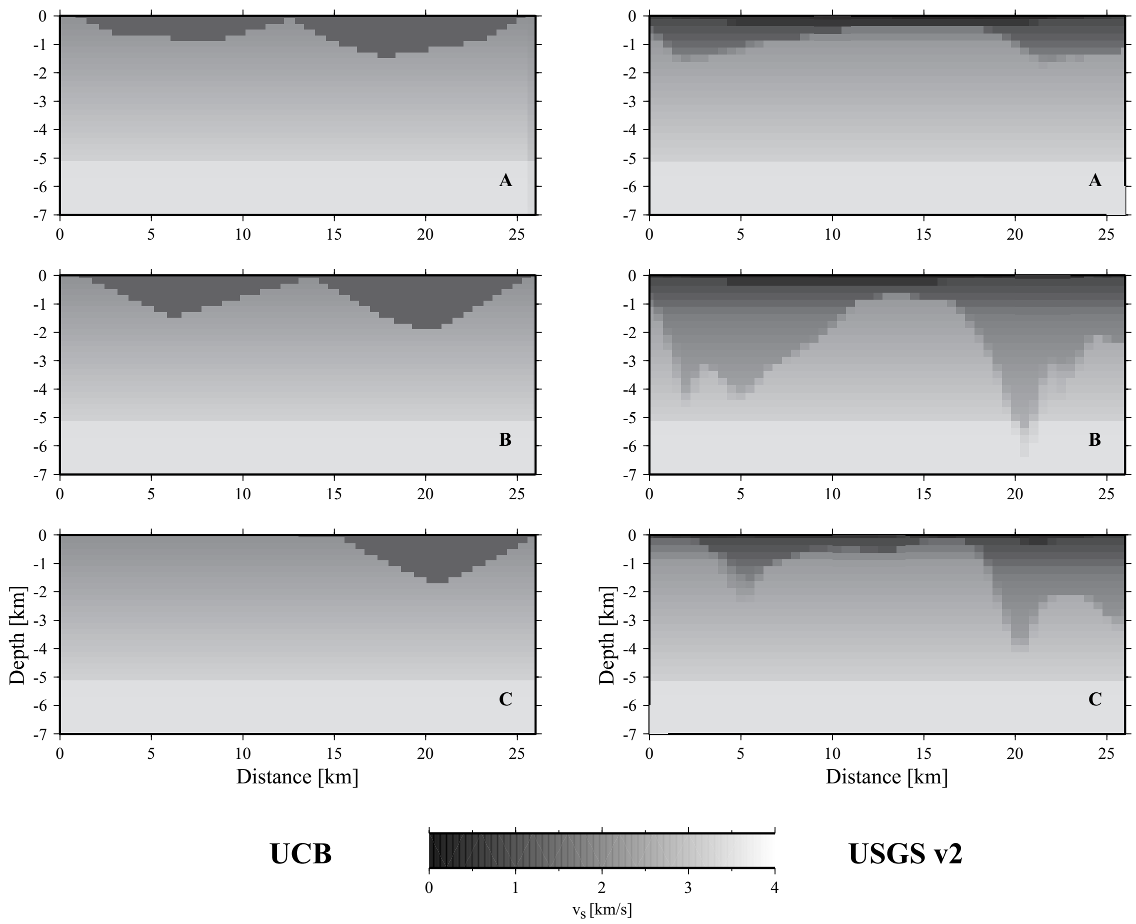

Figure 2.6: Cross sections of shear-wave velocities from the UCB and the USGS models across the SCV basins, along the lines A, B, and C shown in Figure 2.3.

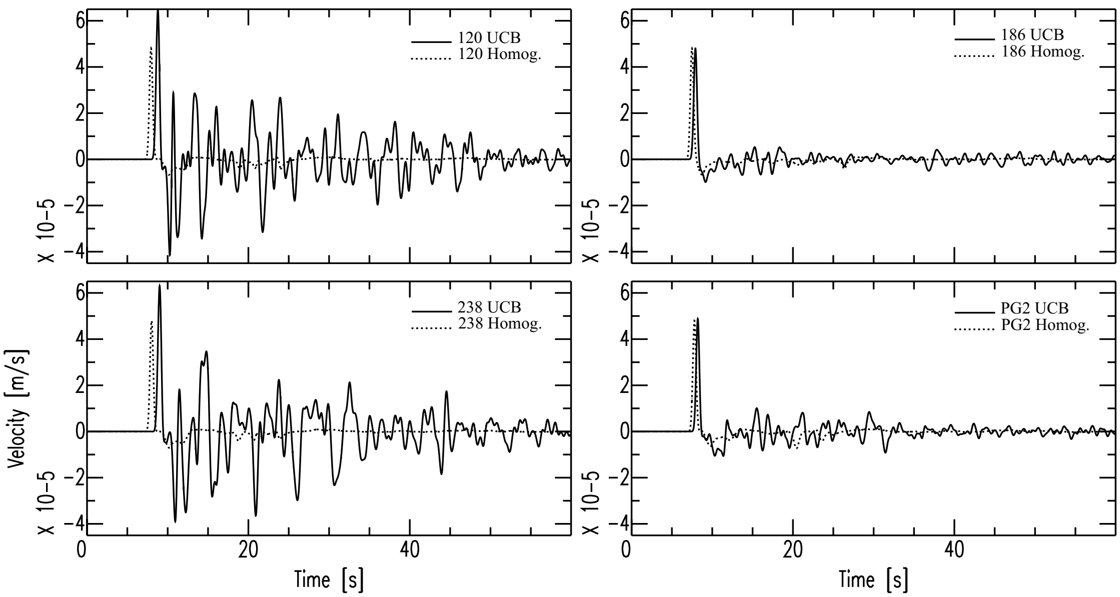

Figure 2.7: Synthetic waveforms for the UCB (solid) and for the homogeneous model (dotted) for the P wave of the event 4 on stations 120, 238, 186, and PG2. Late arrivals in the homogeneous model are due to the finite model dimensions and finite plane wave approximation.

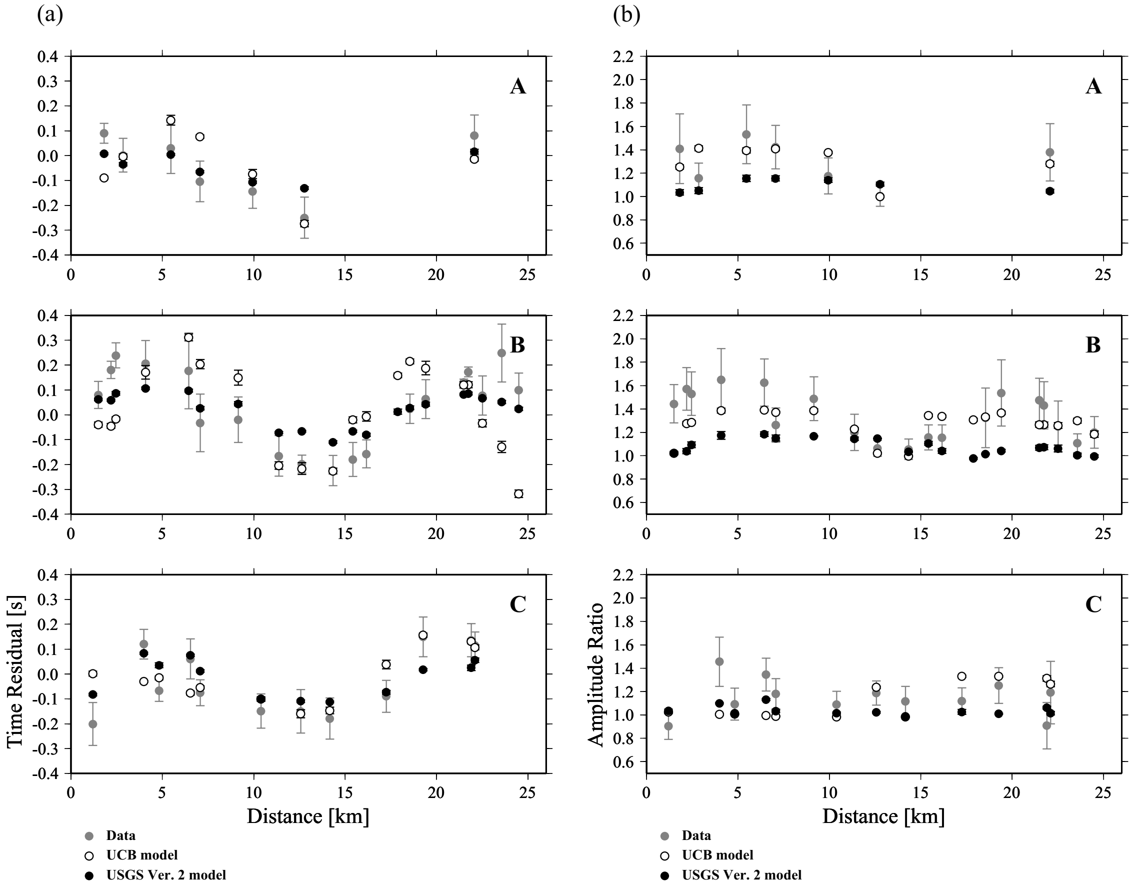

Figure 2.8: (a) Travel-time residuals for the observed and simulated waveforms across the profiles A, B, and C shown in Figure 2.3. The mean values and standard deviations for the seven teleseismic events are shown. (b) Relative amplitudes for the observed and simulated waveforms. Presented values are relative to station 186, located south of the Cupertino basin (see Fig. 2.3). The mean values and standard deviations for the seven teleseismic events are shown. Waveforms have been bandpass filtered between 0.1 and 0.5 Hz.

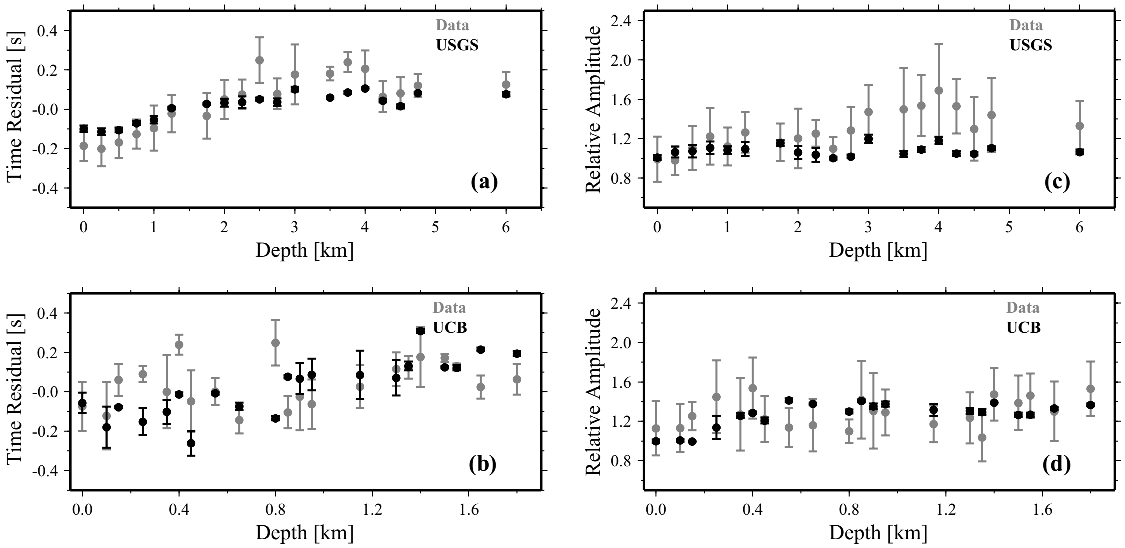

Figure 2.9: Travel-time residuals averaged over all events as a function of basin depth for the observed (gray) and synthetic (black) data for the USGS (a) and the UCB model (b). Also shown are the relative amplitudes averaged over all events for the observed (gray) and synthetic (black) data for the USGS (c) and the UCB model (d). In addition, the results for all stations with the same basin depth were averaged; therefore only one value is presented for each depth.

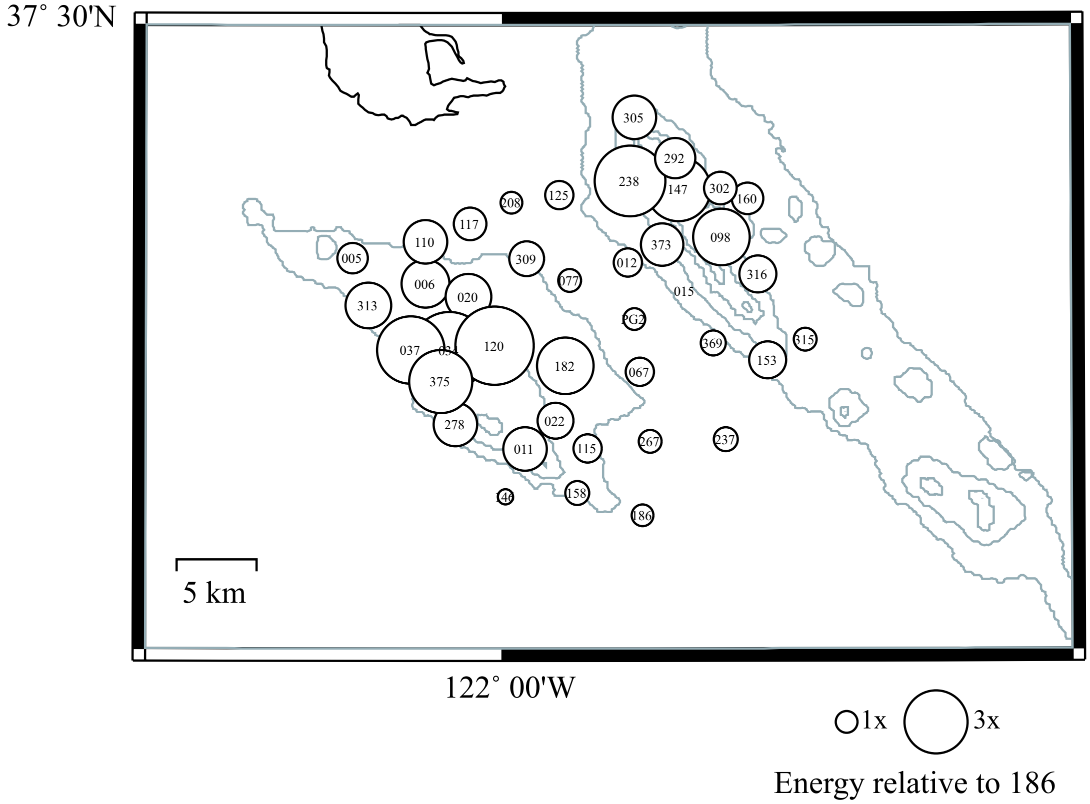

Figure 2.10: The average P-wave energy for the seven teleseismic events relative to station 186. Contours of the basins from the USGS model at 1 km, 3 km, 5 km, and 6 km depth are shown in gray.

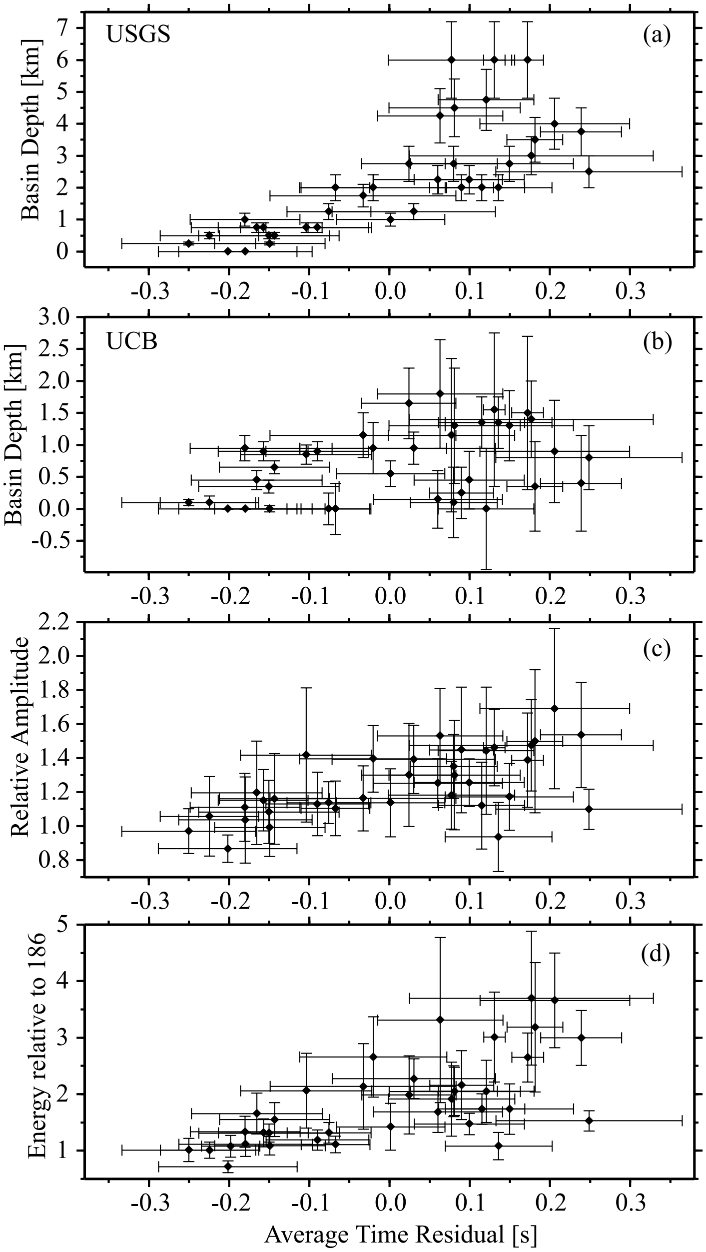

Figure 2.11: (a) Basin depth from the USGS model as a function of the average time residual measured for the seven teleseismic events. Each data point represents a SCVSE station. (b) Same as (a), except that the basin depth from the UCB model is used. (c) Relative amplitudes as a function of the average time residual for the seven teleseismic events. (d) Average P-wave energy for the seven teleseismic events relative to the station 186 as a function of average time residual. Each data point represents a SCVSE station.

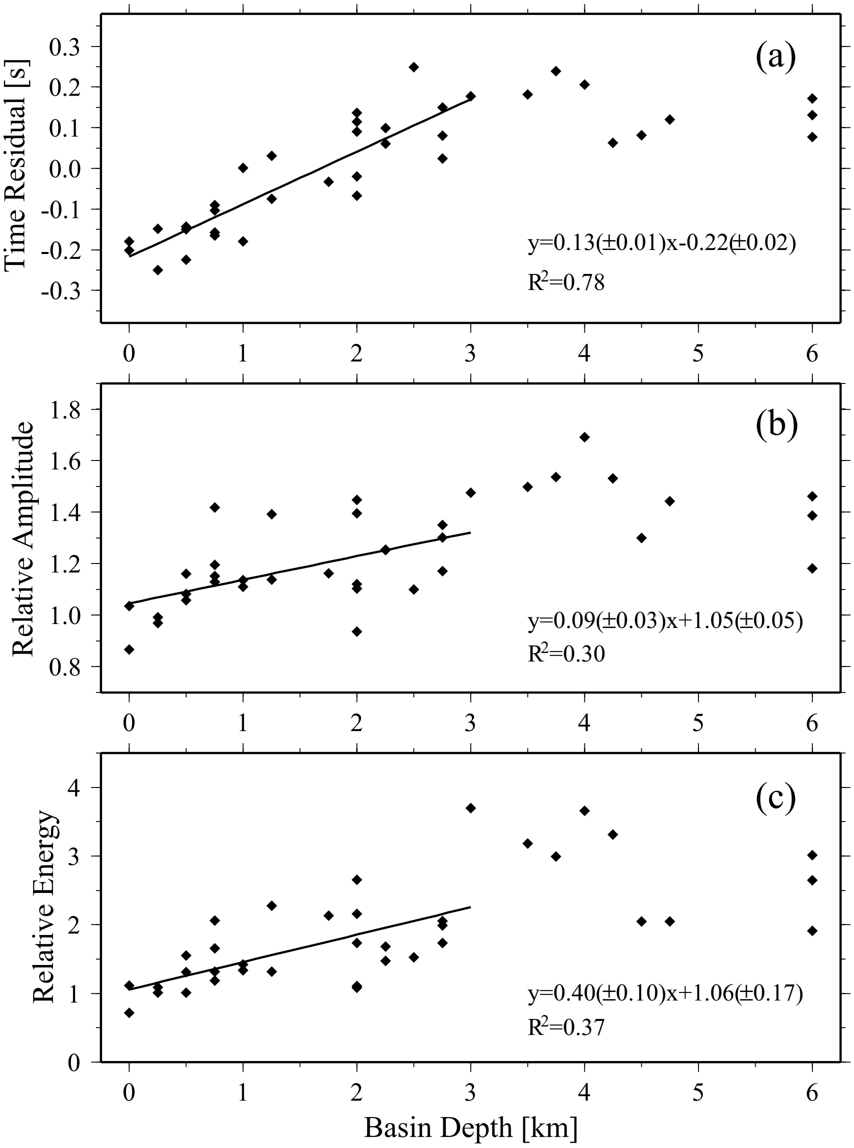

Figure 2.12: (a) Travel-time residuals averaged over the seven teleseismic events as a function of the USGS model basin depth. Stations located above the basin that was shallower than 3 km were used in the regression. Equation of the line fit and the R^2 value are listed. Standard errors are included in parenthesis. (b) Relative amplitudes for the seven teleseismic events as a function of the USGS basin depth. (c) Average P-wave energy for the seven teleseismic events as a function of the USGS basin depth.

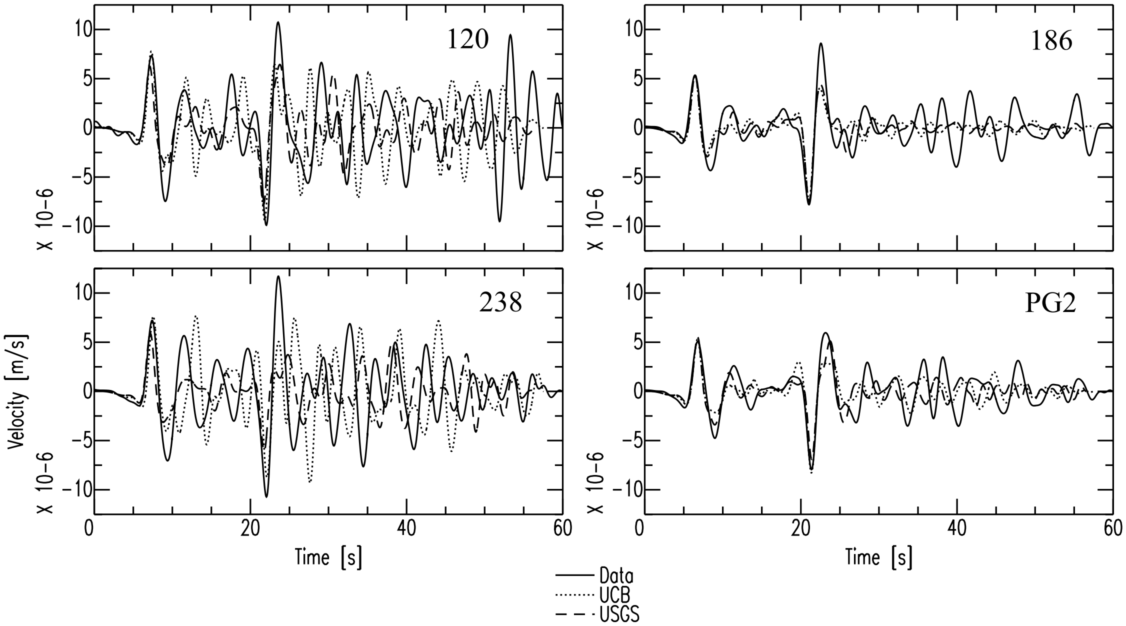

Figure 2.13: The observed (solid) and calculated waveforms for the UCB (dotted) and the USGS model (dashed) for event 4. Stations 120, 238, 186, and PG2 are shown. The first P wave is followed by the pP wave about 15 sec later. Strong converted arrivals can be seen between the P and pP waves.

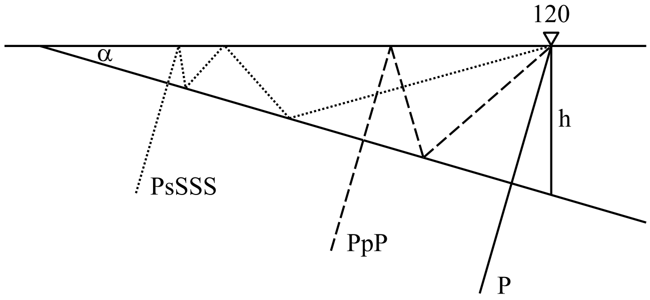

Figure 2.14: Part of the UCB model cross section across the SCV through station 120, used to estimate travel-time delays for some of the converted arrivals (see Table 2.2). In the UCB model, the depth of the basin under the station 120 is $h = 1.4km$, and the dip of the Cupertino basin in the west is $\alpha = 16.3^o$. The P wave and two converted phases are shown. The incident P wave perpendicular to the basin bottom was used in the calculation.

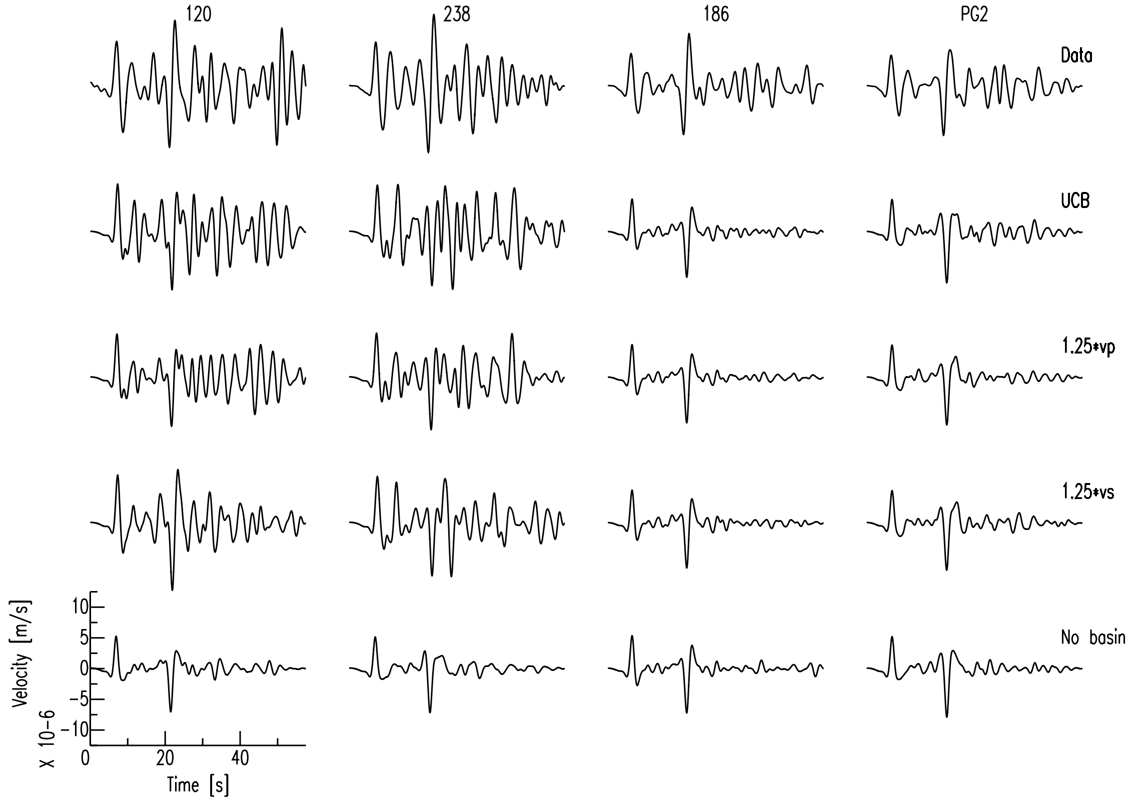

Figure 2.15: The observed waveforms (top) for event 4 recorded at stations 120, 238, 186, and PG2. Shown below are the calculated waveforms for the UCB model, the UCB model with the 25% increased P-wave velocity in the SCV basins, the UCB model with the 25% increased S-wave velocity in the SCV basins, and the UCB model with the SCV basins removed.

Chapter 3

Microseisms observations in the Santa Clara Valley, California

This chapter was published in *Bulletin of the Seismological Society of America* [*Dolenc & Dreger*, 2005] with the title 'Microseisms observations in the Santa Clara Valley, California'.

Summary

We have investigated ground-motion amplification in the Santa Clara Valley (SCV) using microseisms observed during the 1998 deployment of 41 short-period seismometers. The Santa Clara Valley Seismic Experiment (SCVSE) [*Lindh et al.*, 1999; *Fletcher et al.*, 2003]) recorded many local, regional, and teleseismic events. In our previous work we investigated the 3D velocity structure of the SCV by modeling the teleseismic P waves recorded during the SCVSE [*Dolenc et al.*, 2005a]. To comple-

ment these results, we now focus on the microseisms that were recorded during the same period and relate these observations to local earthquake wave amplification. It is found that the seismic noise is related to the ocean wave heights measured on the weather buoy west of Half Moon Bay, California. The spectral ratio of the horizontal to vertical (H/V) microseisms at each SCVSE site is stable with time, and the period of the dominant peak in the H/V ratio is related to the basin depth. The results of this study show that seismic noise can be used in the assessment of the effects of deep sediments on long-period earthquake ground motions.

3.1 Introduction

Santa Clara Valley (SCV) is located south of the San Francisco Bay and comprises two elongated alluvial basins, the Cupertino basin in the west and the Evergreen basin in the east. To learn more about the basin structure, the Santa Clara Valley Seismic Experiment (SCVSE), a joint project of the U.S. Geological Survey (USGS), University of California, Berkeley (UCB), and Incorporated Research Institutions for Seismology Program for Array Seismic Studies of Continental Lithosphere (IRIS PASSCAL), was deployed in the SCV from June through November 1998 (Fig. 3.1). In our previous work we investigated the 3D velocity structure of the SCV by modeling the teleseismic P waves recorded during the SCVSE [*Dolenc*, 2001; *Dolenc et al.*, 2005a]. The goal of this study was to demonstrate that the microseisms recorded during the SCVSE are also sensitive to the deep basin structure and can be used to predict the effects of deep sediments on long-period earthquake ground motions.

3.2 Microseisms

The microseisms are generated by the ocean waves and their signal can be observed in the noise spectra from any site. Microseisms show a large peak at 0.2 Hz which is called the double-frequency peak. It is a result of the pressure variations on the sea floor caused by the standing ocean waves which have frequency that is twice the frequency of the original traveling ocean waves [*Longuet-Higgins*, 1950]. A second microseisms peak can be observed between 0.05 and 0.1 Hz and is called the primary or single-frequency peak. It is much smaller and is generated by a different mechanism than the double-frequency peak [*Webb*, 1998].

We examined the relationship between the ocean waves recorded on the buoy west of Half Moon Bay, California, and the microseisms recorded by the SCVSE. The locations of the weather buoy and of the SCV seismic stations are shown in Figure 3.1. The buoy data were obtained from the National Data Buoy Center and consist of standard meteorological data as well as wind and wave information. In this study we used spectral wave density (SWD), a recorded energy within frequency bins covering the range from 0.03 to 0.4 Hz. Figure 3.2 shows the spectral wave density in the three frequency bins in July and October 1998. We selected one quiet (26-30 July) and one stormy interval (24-28 October) for further analysis. There were no significant local, regional, or teleseismic events in either of the two 5-day periods.

Figure 3.3 presents an example of the observed data. The SWD of the ocean waves recorded at the buoy (black) and the power spectral density (PSD) for the seismic data recorded on the vertical components at the stations 313 and 098 are shown. The two stations were selected as representatives of stations located close to the ocean (313) and those further inland (098). The PSDs of the seismic data are compared to the ocean-wave data recorded in the half-frequency bin. The moving average over five adjacent data points was applied to buoy and seismic data. The left column shows data for the quiet interval in July 1998 and the right column shows data for the stormy interval in October 1998.

In both cases the seismic noise closely tracks the ocean-wave data. This is true at all the seismic stations. These results confirm that the noise observed at the SCV seismic stations during stormy and quiet periods is related to ocean waves and not to urban noise.

3.3 Continuous excitations of the SCV basins

To determine whether the effect of the basins can be seen in the recordings of the microseisms, we calculated the average PSD at each station for several days. The vertical component ground-velocity records were processed by deconvolving the reported instrument response parameters [*Lindh et al.*, 1999]. For every day, the PSD was calculated for 5-min segments at the beginning of each hour for the vertical seismic data. The results were first averaged over the 0.1- to 1-Hz frequency range and then through the day to obtain a single value for each day.

The relationships between the PSDs at the various sites were remarkably consistent. As an example results from 28 October 1998 are presented in Figure 3.4. The font styles indicate different seismometer types, and the radii of the circles represent the average PSD values. The values are consistently larger over the two basins and smaller between them. As expected, the values observed in the Cupertino basin, which is closer to the ocean, are larger than in the Evergreen basin. No correlation exists with the seismometer type.

The general pattern of these results is similar to that observed for the average P-wave energy of the teleseismic events recorded by the same array (figure 8 in *Dolenc et al.*, 2005, and also figure 2.10 in chapter 2). Both data sets indicate that a correlation exists between the observed energy and the outline of the Cupertino and the Evergreen basin.

3.4 H/V spectral ratio of microseisms

The use of the spectral ratio between the horizontal and vertical components (H/V ratio) to estimate the site amplification from a single-station noise recording was first proposed by *Nakamura* [1989]. Since then, many studies have used the H/V technique to evaluate site response and identify fundamental resonance frequencies of the sedimentary layers. The H/V technique is most often used to study the response of the shallow structures, mainly the response of the soft soils. Some of the studies also applied the H/V technique to deep basins [*Yamanaka et al.*, 1994; *Dravinski et al.*, 1996; *von Seht & Wohlenberg*, 1999; *Bodin & Horton*, 1999; *Bodin et al.*, 2001]. Typical period ranges of data used in shallow-site studies and deep-basin studies are 0.5-2 sec and 2-5 sec, respectively.

We calculated H/V spectral ratios of microseism signals for a 5-day earthquake-free period for each SCV station. The geometric average of the two horizontal components was used to calculate the horizontal spectrum. The H/V spectral ratios for the 5-min segments at the beginning of each hour were calculated. The dominant period of the H/V spectral ratios in the 0.1- to 1-Hz frequency range is stable over time and depends on the location. We show, as examples, the H/V spectral ratios for station 006 located in the northern part of the Cupertino basin, for station 117 at the eastern edge of the Cupertino basin, and for station 208 located between the two basins (Fig. 3.5). Periods of increased noise for individual time segments are seen as vertical lines in the plots most noticeably in the 0.8- to 1-Hz frequency range. However, the dominant signal that is stable with time can be observed around 0.2 Hz for station 006, around 0.35 Hz for station 117, and between 0.35 and 0.6 Hz for station 208. Most of the stations exhibit a similar stable peak between 0.1 and 1 Hz.

To obtain an overall picture we again averaged the H/V spectral ratios calculated for 5-min segments at the beginning of each hour over the 5-day interval. Figure 3.6 shows results obtained for the quiet interval in July 1998 (dashed) and for the stormy interval in October 1998 (solid). Although the excitation levels for the two intervals were significantly different (Fig. 3.2), the H/V spectral ratios are very similar. This confirms that the H/V spectral ratios are stable not only over an interval of a few days, but also of a few months. Some of the stations do not show a peak in the 0.1- to 1-Hz frequency range and this is also observed during both time periods.

On some stations different absolute amplitude of the H/V spectral ratios can be observed for the two time periods (e.g., stations 098, 125, 309 in Fig. 3.6). Because some of the instruments were changed between the two periods we monitored individual instruments to see if amplitude changes could suggest instrumental problems. But we could not identify instruments that would consistently show low H/V spectral ratios. We therefore do not think that the differences are instrument related, but rather that they result from slightly different directionality of the microseisms for the two periods. If this is the case, and assuming that the amplification and interference patterns of the basin 3D structure are direction dependent, this could result in observed changes of absolute amplitudes. The fact that the period of the H/V peak is stable with time and that at the same time we can observe variations in the peak amplitude on some stations suggests that the observed period shifts are first order in nature and amplitude variations of the second order.

The periods of the dominant peak of the H/V spectral ratio in the 0.1- to 1-Hz frequency band appear to be correlated with the two SCV basins (Fig. 3.7). At the stations located above the two basins the dominant peak has longer periods than at the stations located between the basins.

The analysis of the teleseismic P waves of seven events recorded by the SCVSE described in a companion study [*Dolenc et al.*, 2005a] demonstrated the influence of the SCV basins on the timing of primary arrivals. Observed P-wave arrival-time delays were on the order of $\pm 0.25 sec$ and showed the spatial extent of the basins. These arrival-time delays were found to correlate strongly with other observations such as primary P-wave amplification and seismic wave energy. Here we show that arrival-time delays are also correlated to the dominant period of the microseisms H/V peak.

Figures 3.8a and 3.8c show the period of the dominant H/V peak in the 0.1- to 1-Hz frequency range as a function of travel-time residuals from the companion paper [*Dolenc et al.*, 2005a]. The uncertainty of the period of the H/V peak is presented as the width of the H/V peak at 85% of its maximum value. Although we chose this value is arbitrarily based on our review of all of the data, it is in our opinion a conservative estimate of the possible errors in picking such a peak in the H/V spectra.

In Figures 3.8a and 3.8c just the two very different types of observations are compared. Figures 3.8b and 3.8d, on the other hand, show the period of the dominant H/V peak in the 0.1- to 1-Hz frequency range in the two intervals as a function of the basin depth as given in the USGS model [*Brocher et al.*, 1997; *Jachens et al.*, 1997]. The USGS model and the steps used to determine the USGS model basin depths are described in *Dolenc et al.* [2005].

The correlation is clear between the period of the dominant H/V peak in the 0.1- to 1-Hz frequency range and the basin depth up to 3 km depth. This suggests that the H/V method can be used to determine and constrain the deep structure of the alluvial basins. The best-fit line in Figures 3.8b and 3.8d is shown for the stations located above basins shallower than 3 km. The 3-km depth for the best-fit line was selected to match the teleseismic observations (figure 2.12 in chapter 2.) and local earthquake observations (figures 3.9 and 3.10, right columns). The uncertainty in the basin depth is estimated to be 20% of the depth [*Jachens et al.*, 1997]. A similar trend of increased period of the dominant H/V peak can be observed when the results are plotted against the UCB model basin depth. Since previous work presented in Chapter 2 indicated that the USGS basin geometry better describes the observations, only the USGS model was used in the analysis.

Some studies have used H/V ratios to predict amplification of ground motion at the specific sites. *Lermo and Chávez-García* [1994] have shown that Nakamura's technique [*Nakamura*, 1989] can be used to obtain a rough estimate of the amplification of seismic waves but only when the local geology is simple. Theoretical investigations [*Lachet & Bard*, 1994; *Dravinski et al.*, 1996], on the other hand, have shown that the H/V method is efficient for estimating the fundamental frequency of a sedimentary site, but that the H/V ratio is not adequate for estimating ground-motion amplification in deep sedimentary basins.

The amplitudes of the H/V peaks for the two 5-day intervals as a function of the basin depth from the USGS velocity model are shown in Figure 3.10. The mean value and standard deviation are presented for each station. Standard deviation is obtained from averaging H/V ratios for every hour, at the period of the final H/V maximum. The results show that there is a very weak inverse correlation, if any, between the amplitudes of the H/V spectral ratios and the basin depth. Slightly larger H/V amplitudes can be observed at the stations over basins shallower than 2 km. However, considering the uncertainty in the observations and basin depth, there does not appear to be any correlation of H/V amplitude with basin depth. Similarly, when the amplitudes of H/V peaks are plotted as a function of the teleseismic delay times, no correlation is observed.

3.5 Ground motions from local earthquakes

One of our objectives is to find relationships between the seismic observables and basin thickness. It is also of primary interest to obtain such relations for local earthquake wave amplification.

The two strongest local earthquakes recorded during the SCV seismic experiment were the San Juan Bautista (SJB, 12 August 1998; M_L5.4; depth, 9 km) and the Gilroy (10 October 1998; M_L4.0; depth, 6.5 km) event. Their locations and focal mechanisms are shown in Figure 3.1.

To measure the incoming seismic wave energy, the vertical and horizontal waveforms were squared and integrated for the 125 sec after the P-wave arrival. Peak ground velocity (PGV) recorded on the vertical and horizontal components was also measured. The horizontal component that was used was always the vector sum of the two horizontal channels. Results for the Gilroy and SJB events are shown in Figures 3.9 and 3.10. Waveforms were bandpass filtered between 0.1 and 0.3 Hz. This band is used because more systematic results were obtained than in the full-bandwidth case (0.1 to 1 Hz). This is likely because at local distances peak ground motions at short periods are caused by body waves that interact with mid- and lower-crust structure. By examining the lower frequencies, surface waves in the local earthquake records are enhanced and a comparison between local earthquake surface waves and microseism waves is more justified. In both figures the panels on the left show the results as a function of the travel-time residuals from the analysis of the recorded teleseismic events [*Dolenc et al.*, 2005a]. Panels on the right show the results as a function of the basin depth from the USGS velocity model. Stations above basins shallower than 3 km were used in the regression. The equations of the best-fit lines and the R^2 values are listed in the figures and standard errors are included in parenthesis.

Results from the two local events show that the seismic wave energy and PGV for vertical and horizontal components increase with the measured travel-time delays determined from the teleseismic events and with the basin depth from the USGS model. The overall range in PGV amplification in the 0.1- to 0.3-Hz band is about a factor of 2 over the 4-km range. The correlation of local earthquake PGV saturates for basin depths greater than 4 km, similar to what was observed previously for the microseisms (3 km) and the teleseismic observations (3 km) [*Dolenc et al.*, 2005a].

3.6 1D modeling

We modeled the response of the sedimentary layers using the propagator matrix approach [*Kennett & Kerry*, 1979] and the 1D structures below each SCV seismic station taken from the 3D USGS model and from the 3D UCB model [*Stidham*, 1999; *Stidham et al.*, 1999]. In the USGS model, layers with $v_S < 0.5km/sec$ were not incorporated into the 1D models and the attenuation was taken from the original USGS model. There is almost no variability across the entire SCVSE array in the original USGS model in the shallowest three layers. Since the model is almost flat for $v_S < 0.5km/sec$, these shallow layers should not add to the site-by-site variability in the modeled results. Because attenuation is not included in the 3D UCB model, we used values from layers with similar properties from the USGS model. This resulted in a uniform quality factor $Q_S = 50$ within the basin in the 1D UCB models. A propagator matrix method was used to calculate the transfer function of the basin sedimentary layers for the vertical and horizontal component of ground motion.

In Figure 3.12, the calculated H/V spectral ratios for stations 006, 110, 117, and 208 are compared to the observed H/V ratios at these stations. These four stations are located in the northern part of the SCV (Fig. 3.1). In both models the basin depth decreases from station 006 located above Cupertino basin, to station 208, located in between the basins. The 1D profiles of the shear-wave seismic velocity below these four stations are shown in Figure 3.12.

The results show that for some stations the calculated H/V peak period matches the observed H/V peak period (station 006, USGS model). As the basin depth decreases, the H/V peak widens and moves towards higher frequencies. The same trend can be observed for calculated synthetics. For some stations neither of the two models matches the observed H/V peak. This is not surprising, as the basinŠs complex 3D structure should have a significant effect and should be included in the modeling. Also, the transfer functions of the sedimentary layers were calculated for a simple plane wave and not for a true microseism source.

It may be possible to use the SCV seismic array to locate the microseism sources and then using the 3D finite-difference code simulate the response of the basins. If possible this will allow for the inversion of microseismic data for 3D basin structure. These possibilities are presently being investigated.

3.7 Conclusions

The seismic noise recorded on the SCV seismic stations is related to the energy of the ocean waves observed on the buoy west of Half Moon Bay, California. The period of the microseisms H/V spectral peak in the 1- to 10-sec range is correlated with the depth of the SCV basin beneath the array. The H/V spectral peaks are stable with time and can be observed during both quiet and stormy intervals. Measured energy and PGV for the two local events recorded with the SCV seismic array also show correlation with the depth of the basin beneath the station.

We calculated empirical relationships between the seismic observations and the basin depth. The data in this article, the companion article [*Dolenc et al.*, 2005a], and the accompanying empirical relations may be used to further revise and validate basin structure in the SCV. A consistent observation in this study and the companion article [*Dolenc et al.*, 2005a] is that the seismic observables saturate for basin depths greater than 3-4 km. Although gravity data indicate a density contrast defining the basins extends to greater depth in some places [*Brocher et al.*, 1997; *Jachens et al.*, 1997], our results indicate that it is the shallow part of the basins that most significantly affect the seismic wave fields.

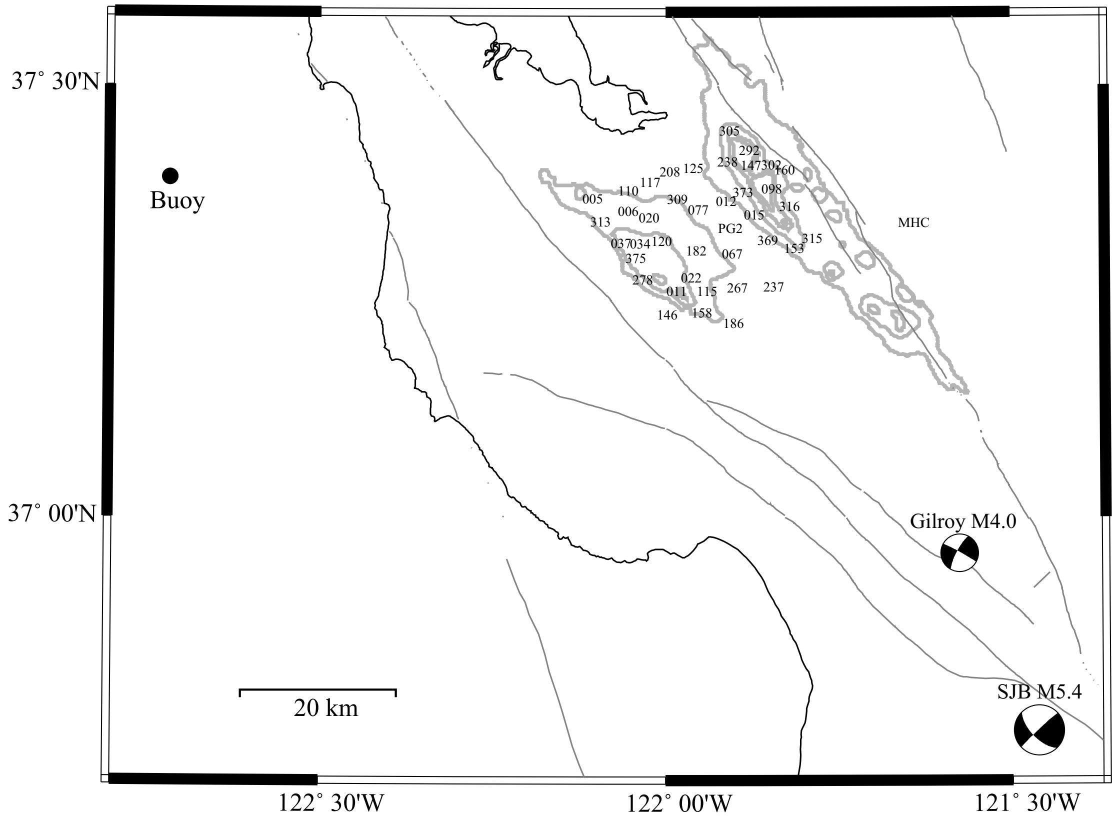

Figure 3.1: Location of the SCV seismic array south of the San Francisco Bay. Numbers indicate SCVSE seismic stations. Thin gray lines are the active faults in the region and MHC is a permanent station of the Berkeley Digital Seismic Network. Contours of the basins from the USGS model at 1 km, 3 km, 5 km, and 6 km depth are shown in gray. The circle indicates the location of the weather buoy west of Half Moon Bay, California. Focal mechanisms from the Berkeley Seismological Laboratory Moment Tensor Catalog are shown for the two local events used in this study.

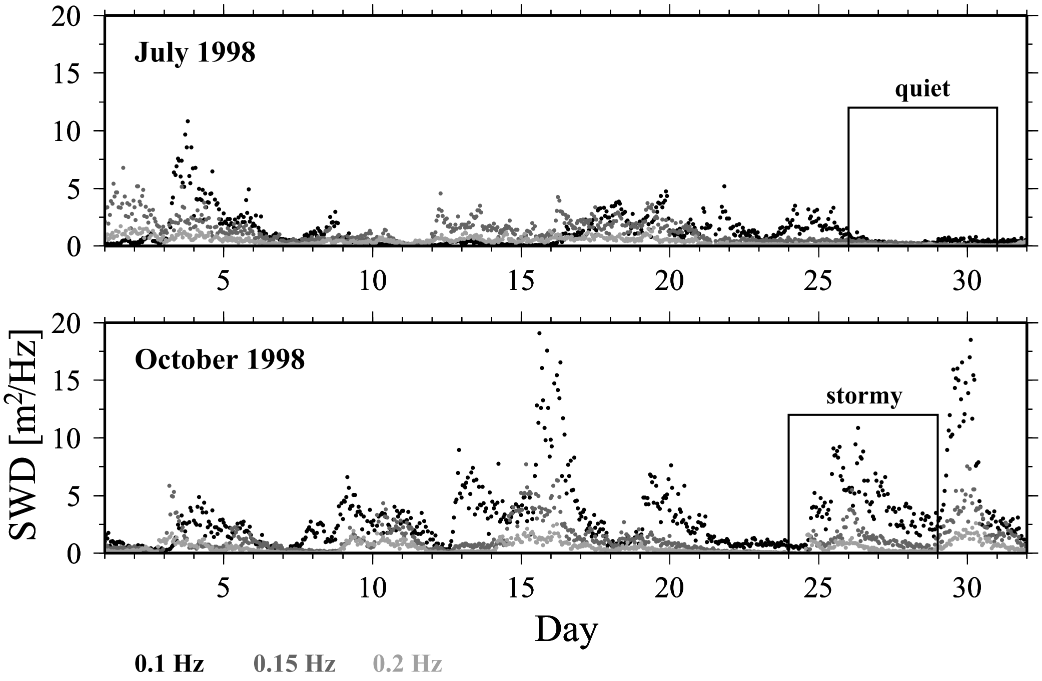

Figure 3.2: Spectral wave density (SWD) of the ocean waves recorded on the buoy west of Half Moon Bay, California, in July and October 1998. Colors denote 0.1 Hz (black), 0.15 Hz (dark gray), and 0.2 Hz (light gray) frequency bin. The width of each bin was 0.05 Hz.

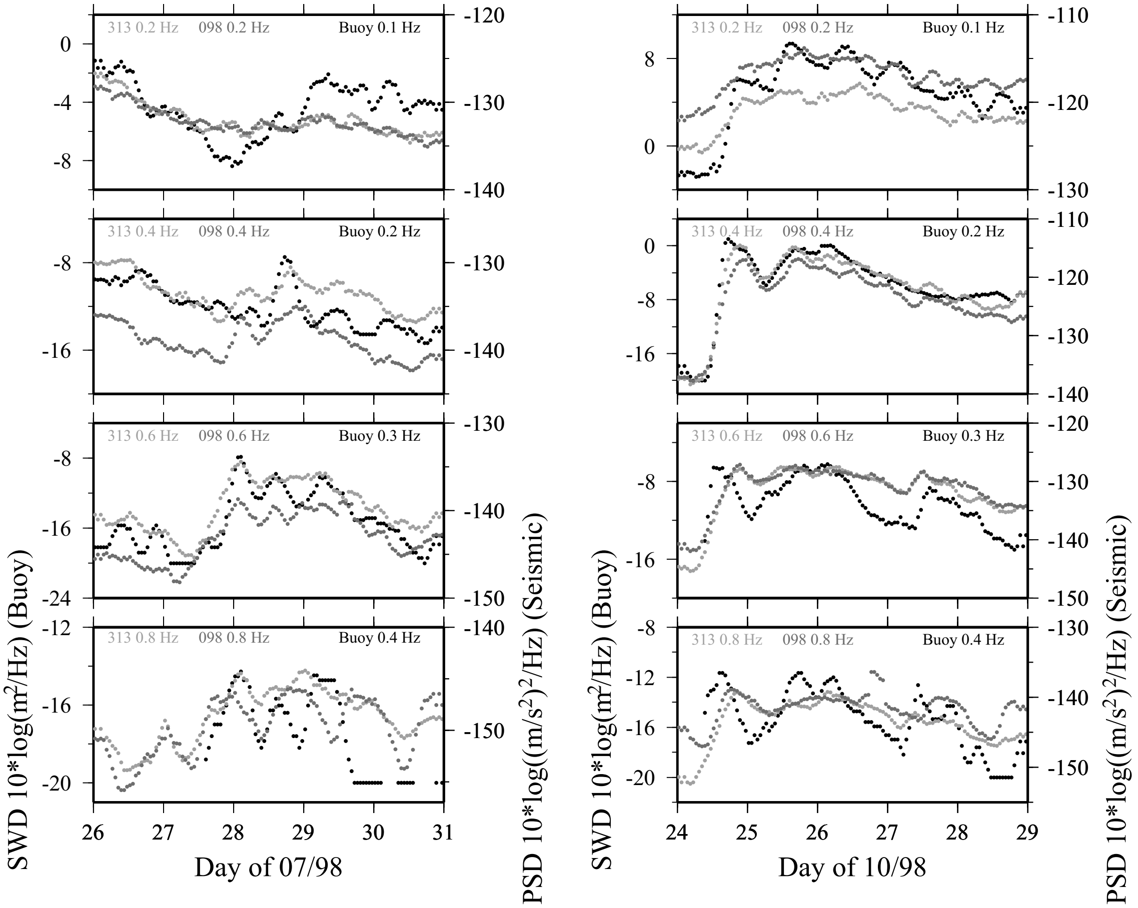

Figure 3.3: Spectral wave density of the ocean waves (black) and the average PSD for the seismic data in the corresponding double-frequency bin recorded on stations 313 (light gray) and 098 (dark gray). Shown are results for a 5-day period in July 1998 (left) and October 1998 (right).

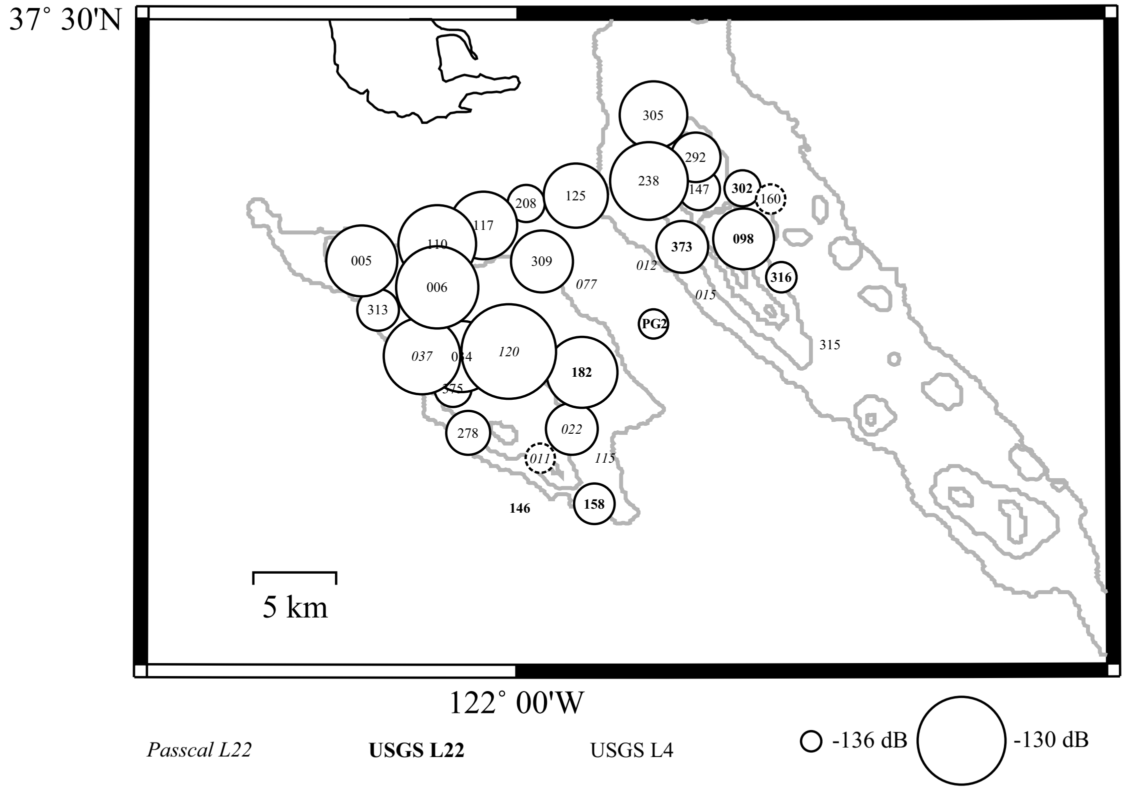

Figure 3.4: The PSD averaged over 0.1- to 1-Hz range and over the 5-min segments at the beginning of every hour on 28 October 1998. The font styles indicate the seismometer model. Only values for the stations with complete data on this day are shown. The average PSD at the stations 011 and 160 was -137.05 dB and -138.96 dB, which would result in the circle smaller than the station label. A larger circle (dotted) is shown instead.

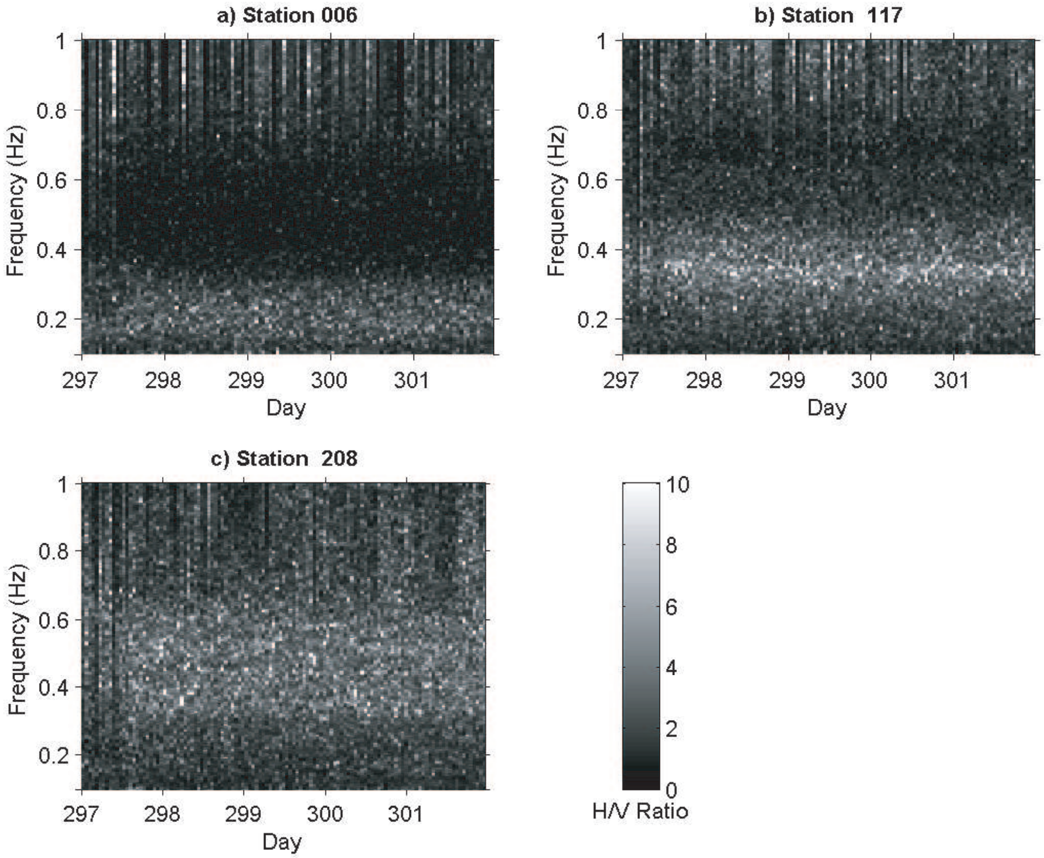

Figure 3.5: H/V spectral ratio for the stations 006, 117, and 208 as a function of frequency and time. Results for a 5-day interval (24-28 October 1998) are shown.

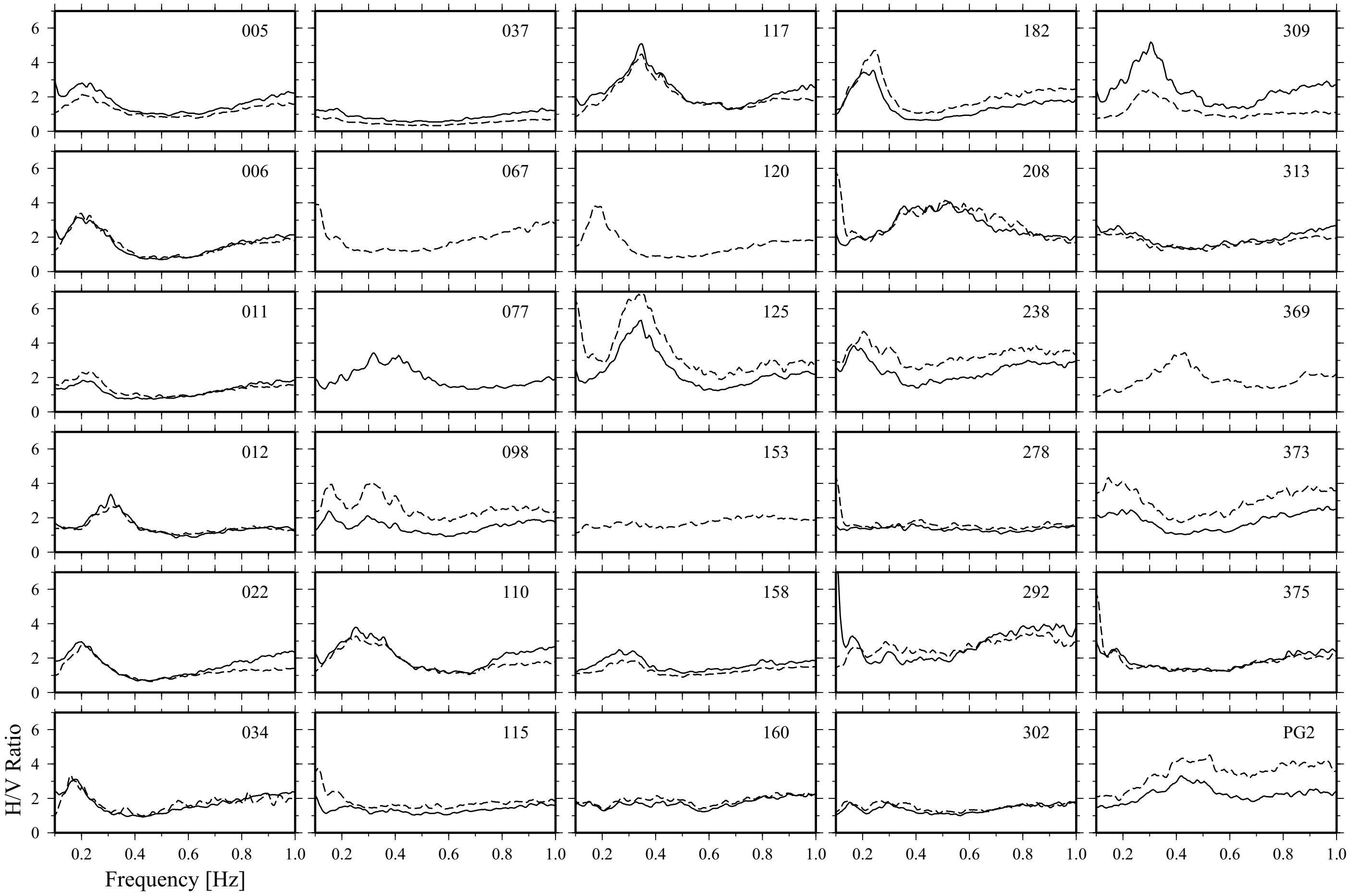

Figure 3.6: H/V spectral ratio for most of the SCV stations calculated for the 5-day interval in July 1998 (dashed) and October 1998 (solid). For a few stations data were only available for one of the periods.

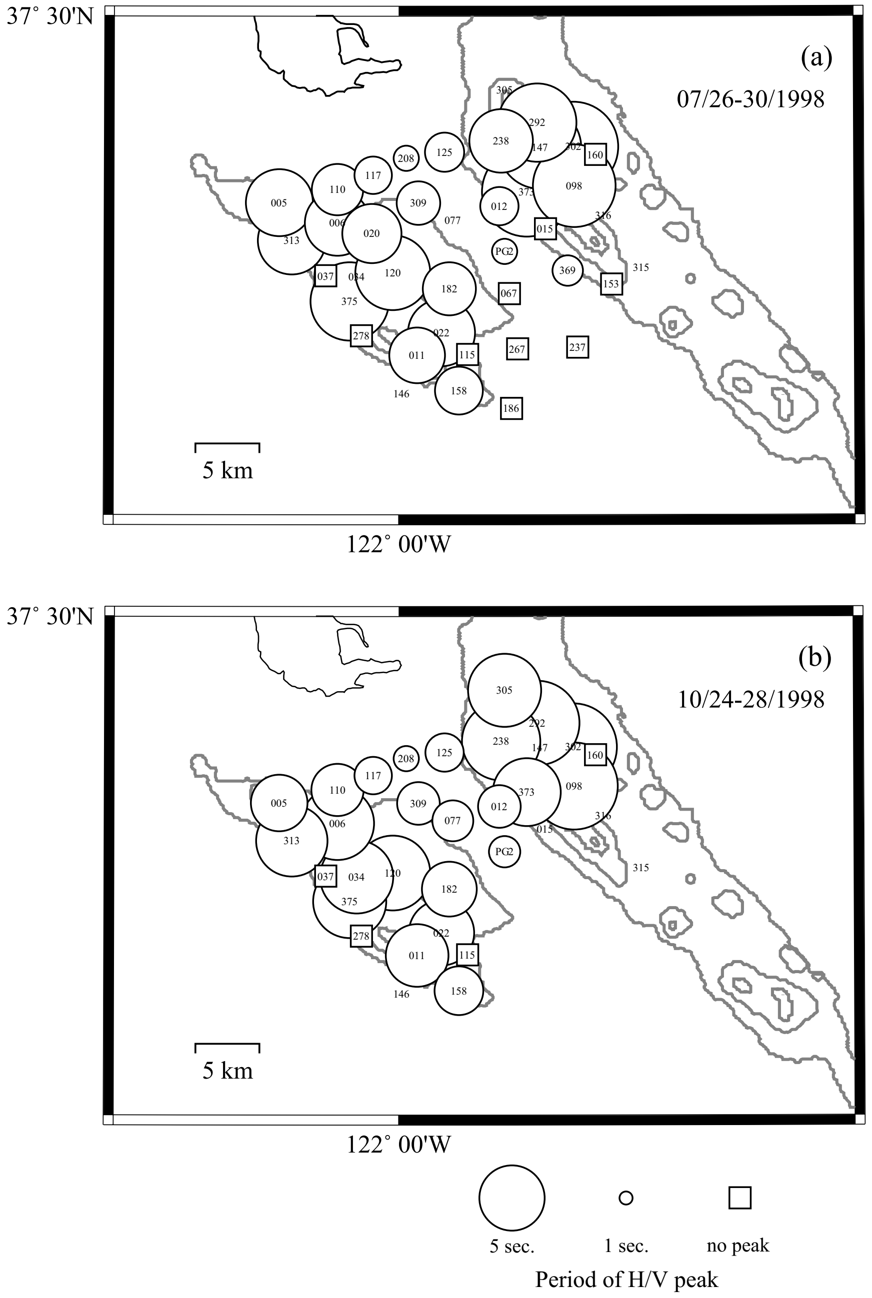

Figure 3.7: The periods of the H/V spectral peaks in the 0.1- to 1-Hz frequency range for the 5-day period in July 1998 (a) and October 1998 (b). The numbers indicate locations of the SCV seismic stations and the circles indicate the periods of the H/V spectral peaks. Stations that showed no peak in the 0.1- to 1-Hz frequency range are indicated by squares. Contours of the basins from the USGS model at 1 km, 3 km, 5 km, and 6 km are shown in gray.

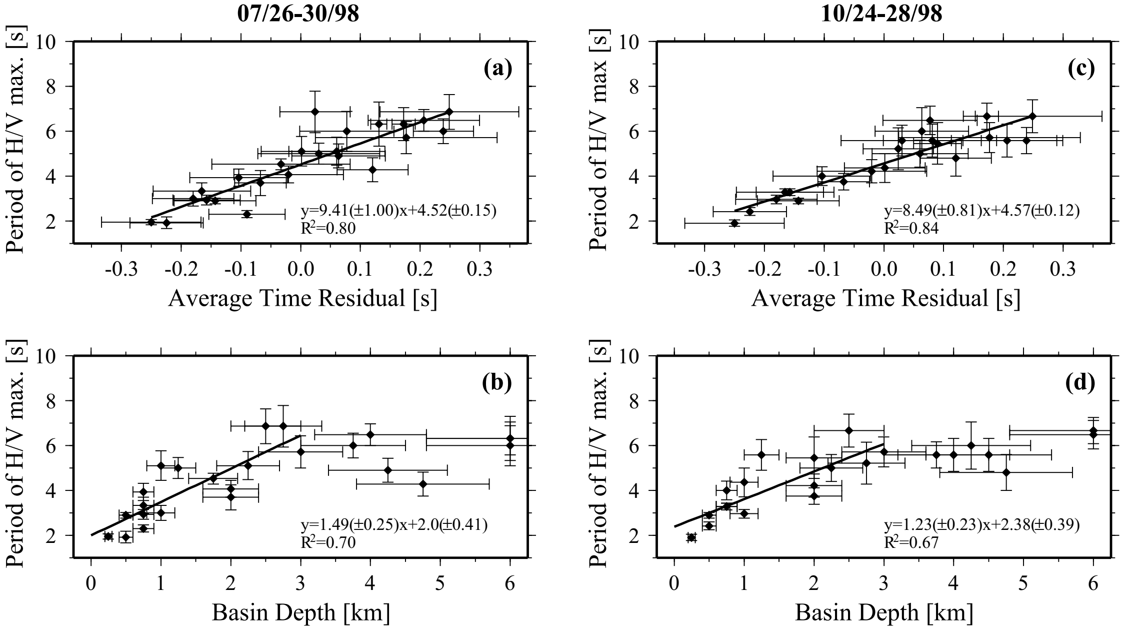

Figure 3.8: (a,c) The period of the dominant H/V peak in the 0.1- to 1-Hz frequency range as a function of travel-time residuals from the analysis of the recorded teleseismic events [*Dolenc et al.*, 2005a]. Results for the two 5-day periods are shown. (b,d) The period of the dominant H/V peak in the 0.1- to 1-Hz frequency range as a function of the basin depth from the USGS model for the two 5-day periods. Stations located above basins shallower than 3 km were used in regression. Equations of the line fit and the R^2 values are listed. Standard errors are included in parenthesis.

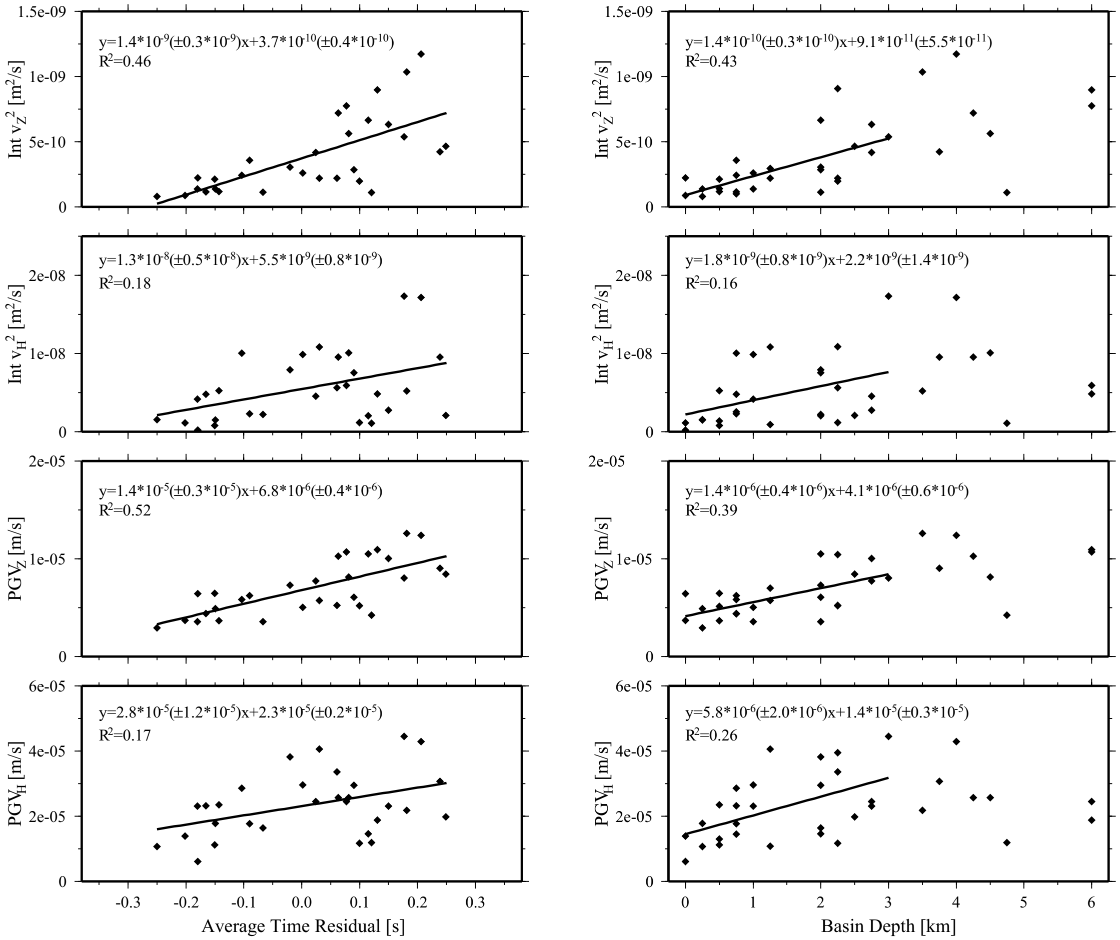

Figure 3.9: Integrated squared velocity for the 125 sec after the P-wave arrival and the PGV measured for the Gilroy $M_L4.0$ event. Results for the vertical and for the horizontal component are shown. The horizontal component that was used was always the vector sum of the two horizontal channels. Panels on the left show the results as a function of the travel-time residuals from the analysis of the recorded teleseismic events [*Dolenc et al.*, 2005a]. Panels on the right show the results as a function of the basin depth from the USGS velocity model. Waveforms were bandpass filtered between 0.1 and 0.3 Hz. The equations of the line fit and the R^2 values are listed. Standard errors are included in parenthesis.

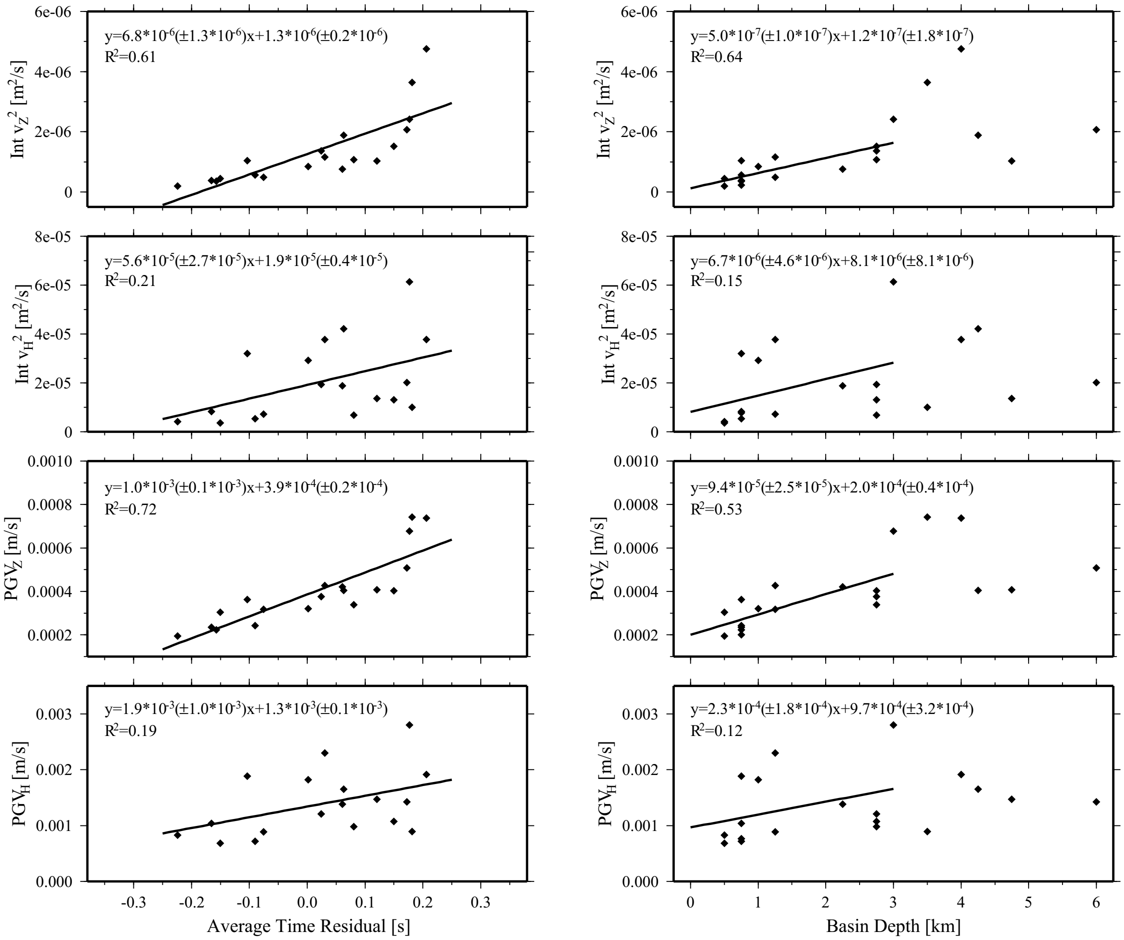

Figure 3.10: Integrated squared velocity for the 125 sec after the P-wave arrival and the PGV measured for the San Juan Bautista M_L5.4 event. Results for the vertical and for the horizontal component are shown. The horizontal component that was used was always the vector sum of the two horizontal channels. Panels on the left show the results as a function of the travel-time residuals from the analysis of the recorded teleseismic events [*Dolenc et al.*, 2005a]. Panels on the right show the results as a function of the basin depth from the USGS velocity model. Waveforms were bandpass filtered between 0.1 and 0.3 Hz. The equations of the line fit and the R^2 values are listed. Standard errors are included in parenthesis.

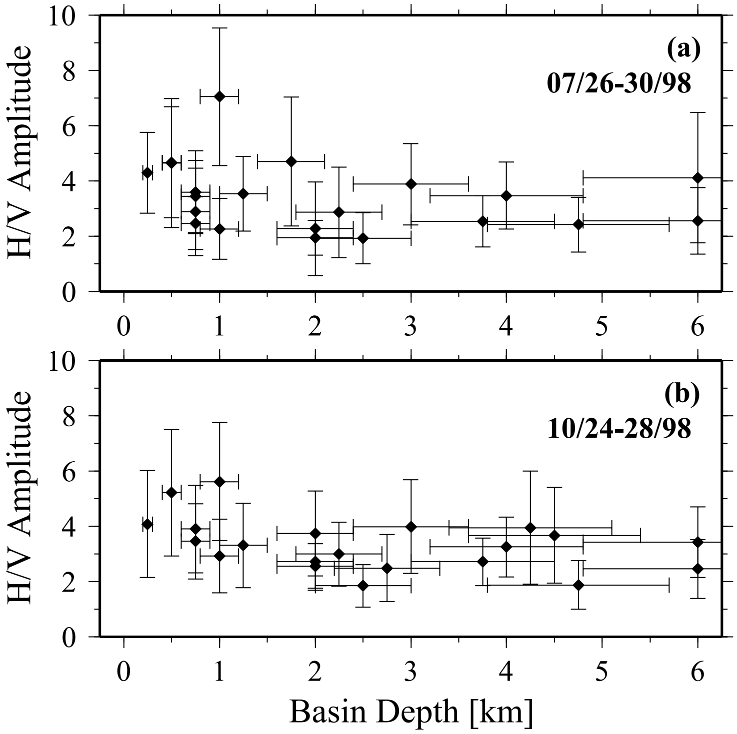

Figure 3.11: The amplitudes of the H/V peaks as a function of the basin depth from the USGS velocity model. Results for the two 5-day periods are shown.

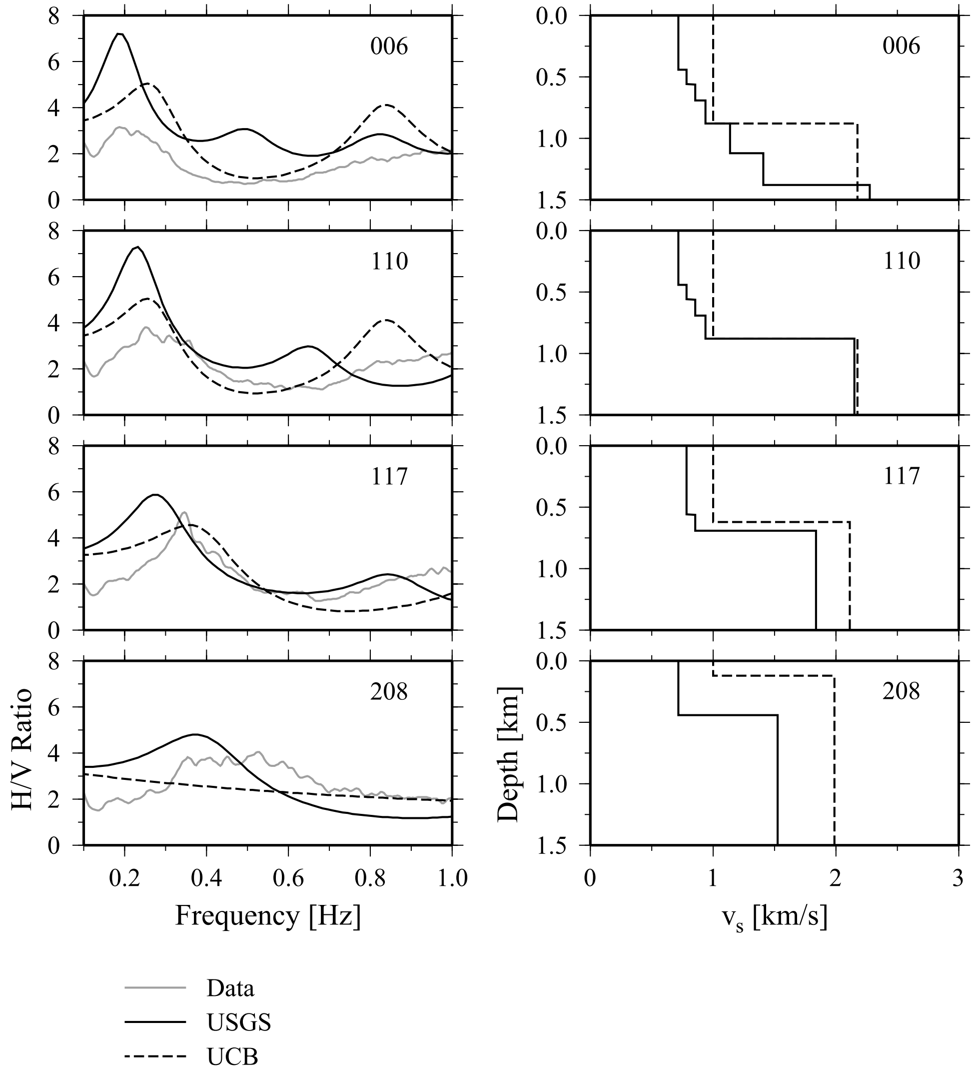

Figure 3.12: (Left) The calculated H/V spectral ratios for four SCVSE stations obtained with the USGS model (black, solid line) and the UCB model (black, dashed line), compared with the observed H/V spectral ratios (gray) measured during the 5-day interval in October 1998. (Right) Shear-wave seismic velocity (v_S) below selected SCV stations as obtained from the USGS model (solid) and UCB model (dashed). The USGS model layers with $v_S < 0.5 km/sec$ were not used in the 1D model.

Chapter 4

3D Simulation of teleseismic P-wave in the Santa Clara Valley, California, using the USGS SF06 velocity model

Summary

The USGS has recently released an updated 3D velocity and density model (USGS SF06) for the greater San Francisco Bay Area [*Brocher et al.*, 2006] that will be used to evaluate shaking hazard for possible future events in the region. In this study I used the 3D model and the 3D finite-difference code E3D [*Larsen & Schultz*, 1995], to simulate the propagation of the teleseismic P-wave through the Santa Clara Valley (SCV) basins. I compared the results to both observations and the simulations obtained with previous models (Chapters 2 and 3).

4.1 Introduction

The seismic velocity models are developed to evaluate shaking hazard for possible future events, to predict where liquefaction of the ground may occur, as well as to locate earthquakes and determine their mechanisms more accurately. The high level of details included in any velocity model and the fact that most of our knowledge about the region was included in its development, does not yet guarantee that the model will provide reliable ground motion estimates for possible future events. In order to accurately predict shaking levels, it is important to first extensively test the model using past event waveform data.

Following its release, the USGS SF06 velocity model was first validated by using it to model the 1989 $M_W 6.9$ Loma Prieta earthquake. As a member of the UC Berkeley group that participated in the SF06 Simulation Project (www.sf06simulation.org), I had a chance to test the model using the finite-difference code E3D and different finite-fault source models for the Loma Prieta event as well as smaller events using point-sources [*Dolenc et al.*, 2006]. Our results for the Loma Prieta event as well as those from other groups showed very good agreement with the observations. At the same time, results from smaller events suggested that modifications might be needed in some regions of the model [*Dolenc et al.*, 2006; *Rodgers et al.*, 2006].

Here I use the USGS SF06 model to simulate the propagation of the teleseismic P-wave through the SCV basin to see how well the model can reproduce the observations and how it compares to results from previous models.

4.2 USGS SF06 velocity and density model

The modeling of the great 1906 San Francisco earthquake for the event's 100th anniversary was one of the reasons for the USGS SF06 velocity model release and also provided the model's name (SF06; www.sf06simulation.org). The model version that I used in this study was USGS SF06 05.1.0. This model is based on a previous version (USGS Version 2; see Chapter 2). It extends to 45 km depth and consists of a detailed model with approximate dimensions of 290×140 km. This detailed model is nested inside an extended model which has approximate dimensions of 650×330 km. The extended model was provided mainly to accommodate the 1906 San Francisco earthquake simulations and as a buffer zone for the simulations with either sources or stations close to the edge of the detailed model. The model's main improvement is that more realistic material properties were assigned to individual geologic units [*Brocher*, 2005a, 2005b, 2005c]. Also, the model now includes topography and material properties of water for the Pacific Ocean and the San Francisco Bay. The other advantage of the new model is that it is stored in an Etree database [*Tu et al.*, 2003], and query routines were developed by the USGS to more easily access its values.

The USGS SF06 model cross sections across the SCV basins, along the lines A, B, and C shown in Figure 2.3, are presented in Figure 4.1 and can be compared to the other two models from Chapter 2. The most striking difference between the USGS SF06 and the other two models is not in the velocities within, but rather outside of the basins. Much faster basement values are now found at shallow depths. Within the basins the velocity gradients are now steeper and very slow values ($v_s < 1km/s$) are mainly limited to the shallowest 500 meters. The depth of the basins remains similar, but the shape of the western edge of the Cupertino basin has also changed significantly. Since the velocities within the basins have only changed slightly from the previous model version, the faster bedrock increased the basin/basement impedance, which is more consistent with the sharpness of the boundary in the UCB 3D model (Chapter 2).

To use the USGS SF06 model with the finite-difference code, I queried the model to extract values on a grid with a 125 m spacing. Because of computation limitations, the slowest velocities in the model were increased to a minimum S-wave velocity of 500 m/s. The slowest P-wave velocity was 865 m/s.

4.3 Modeling

The teleseismic P-wave data recorded in the SCV has been shown to be sensitive to the deep basin structure (Chapter 2). Here I simulate propagation of the teleseismic P-wave through the USGS SF06 model in the SCV region to see how it compares to the observations and previous simulations. The size of the model used in the finite-difference simulation was $220 \times 135 \times 50$ km with more than 760.3×10^6 grid points. As in previous simulations described in Chapter 2, stress-free surface and absorbing boundary conditions were used, and a "sponge" boundary layer was applied to minimize reflections from the model boundaries. Included in the simulation was water (S-wave velocity 0.0 m/s), but not the topography or attenuation. At five grid points per wavelength, frequencies up to 0.8 Hz were simulated with minimal grid-dispersion effects, and the results were compared in the 0.1 to 0.5 Hz passband. To model a teleseismic plane wave, I used a disc of point sources spaced 1.25 km apart in the deepest homogeneous layer of the model. Each compressional point source had a Gaussian pulse shape. Previous modeling of the teleseismic waves (Chapter 2) showed that orientation of the incoming plane wave has very little influence on the basin response, therefore I now used a horizontal plane wave. The simulation was performed on the Linux cluster at the Berkeley Seismological Laboratory.

4.4 Results

The results for the observed and the simulated travel-time residuals are presented in Figure 4.2. The observed travel-time residuals (red) were averaged over all events. Results from previous simulations (open symbols) are for event 4 (Figure 2.2), and results with the USGS SF06 model (black) are for the horizontal plane wave simulation. The measurements made on the synthetics were obtained in the same manner as previously described in Chapter 2. Relative amplitudes for the observed and simulated waveforms are shown in Figure 4.3. Presented values are relative to station 186, located south of the Cupertino basin (see Figure 2.3).

The results from the simulation with the USGS SF06 model show the sinusoidal signal across the basins and basement ridge, as observed in the data and previous synthetics. As previously described in Chapter 2, the UCB model better matches the overall variation and range in the amplitudes and travel-time residuals, but the shape of the observed time residuals and amplitudes is better modeled by the USGS ver. 2 model. The shape of the travel-time residuals obtained with the USGS SF06 model is similar to the USGS ver. 2 model. However, an important difference between the two USGS models is that the USGS SF06 model results show increased time residuals that are now closer to the observations. Although the change is small, it is in the right direction and can be seen across both basins on all three profiles. The mean and standard deviation of the absolute difference between the observed and synthetic travel-time residuals are listed in Table 4.1. Since the two USGS models had similar minimum P- and S-wave velocities, the values for the two models can be directly compared. Results show that the mean absolute difference between the observed and synthetic travel-time residuals for the USGS SF06 model has been reduced when compared to the USGS ver. 2 model. The results for the relative amplitudes show even larger improvement, particularly in the middle section across the Evergreen basin (see Figure 4.3). The shape of the observed relative amplitudes in the southwest and northeast part of the cross section B is much better captured by the USGS

SF06 model than it was by the USGS ver. 2 model. Changes seen on the other two profiles are smaller, but overall the results obtained with the USGS SF06 model moved towards the observations. The Table 4.2 lists the mean and standard deviation of the absolute difference between the observed and synthetic relative amplitudes for the three models. When compared to the values obtained with the USGS ver. 2 model, the USGS SF06 model results are closer to the observations. The largest improvement can be seen for the section B.

The results show that the USGS SF06 model, when compared to the USGS ver. 2 model, is a step in the right direction. The results also indicate that further model refinement is needed. In future work we will test models with the USGS SF06 model basin shape and basement velocity structure, but overall reduced velocities within the basins. Also, we expect that the inverse scheme approach described in Chapter 5 will show that basins with slower average velocities better describe the observations.

4.5 Conclusions

When compared to the previous USGS velocity model for the greater San Francisco Bay Area, the recently released USGS SF06 velocity model includes important changes in the SCV region. Although the structure within the basins as well as the basin depth have not changed much, the updated velocities outside of the basins increased the basin/basement impedance. The observed travel-time residuals and relative amplitudes of the teleseismic P-wave are better modeled with the USGS SF06 model than they were with a previous USGS model version. However remaining misfit between the simulations and the observations indicates that more model refinement with perhaps an inverse scheme as defined in Chapter 5 is needed.

Table 4.1: The mean and standard deviation of the absolute difference between the observed and synthetic travel-time residuals for the three models as shown in Figure 4.2. Results for all stations and for stations in individual sections (see Figure 2.3) are listed. Presented values are in seconds.

	UCB	USGS ver. 2	USGS SF06
All	0.11 ± 0.10	0.077 ± 0.044	0.060 ± 0.044
Section A	0.093 ± 0.064	0.071 ± 0.037	0.038 ± 0.025
Section B	0.15 ± 0.12	0.084 ± 0.052	0.078 ± 0.048
Section C	0.068 ± 0.071	0.070 ± 0.035	0.044 ± 0.033

Table 4.2: The mean and standard deviation of the absolute difference between the observed and synthetic relative amplitudes for the three models as shown in Figure 4.3. Results for all stations and for stations in individual sections (see Figure 2.3) are listed. Relative amplitudes were determined relative to station 186.

	UCB	USGS ver. 2	USGS SF06
All	0.16 ± 0.12	0.21 ± 0.14	0.14 ± 0.11
Section A	0.12 ± 0.10	0.22 ± 0.13	0.17 ± 0.10
Section B	0.15 ± 0.11	0.25 ± 0.17	0.17 ± 0.11
Section C	0.19 ± 0.14	0.15 ± 0.07	0.085 ± 0.086

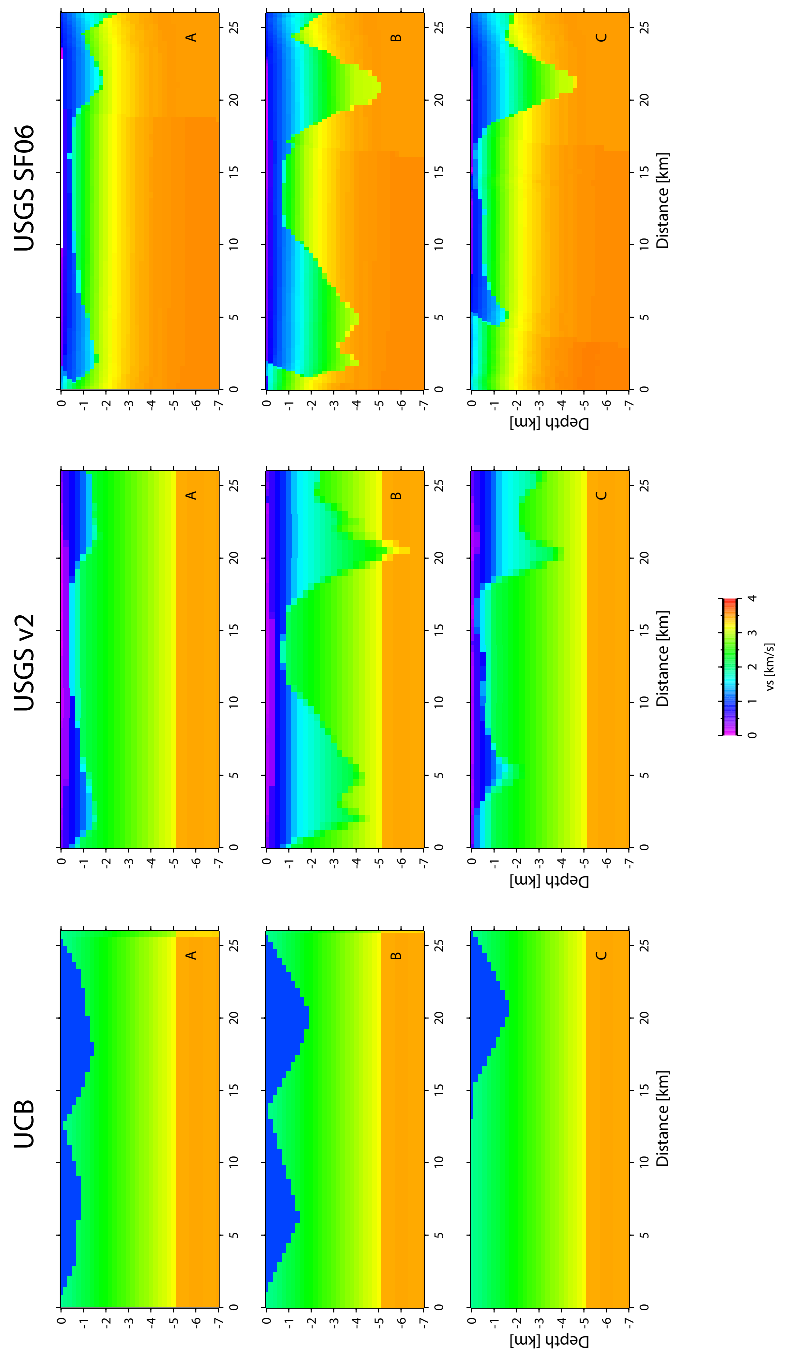

Figure 4.1: Cross sections of shear-wave velocities from the UCB, the USGS v2 (both used in Chapter 2), and the USGS SF06 models across the SCV basins, along the lines A, B, and C shown in Figure 2.3.

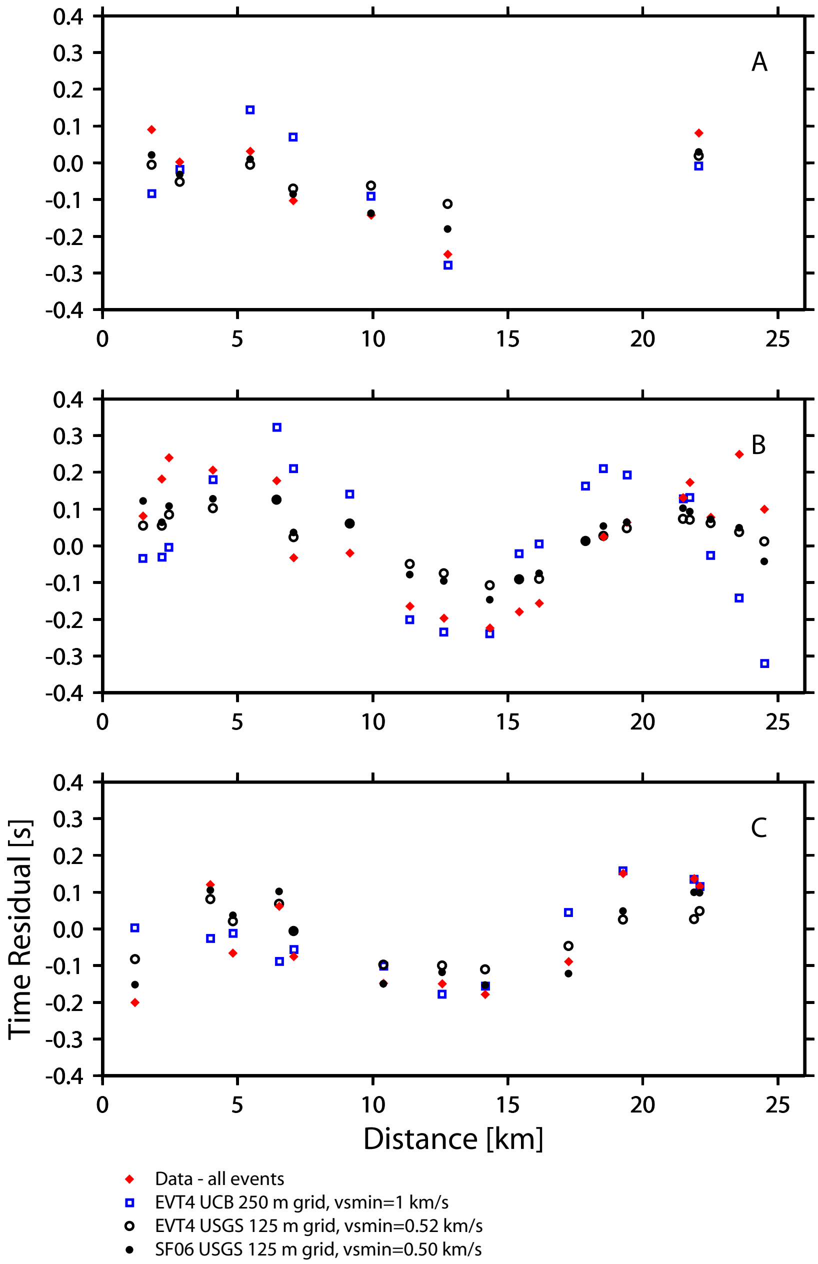

Figure 4.2: Travel-time residuals for the observed and simulated teleseismic waveforms across the profiles A, B, and C shown in Figure 2.3. Waveforms have been bandpass filtered between 0.1 and 0.5 Hz.

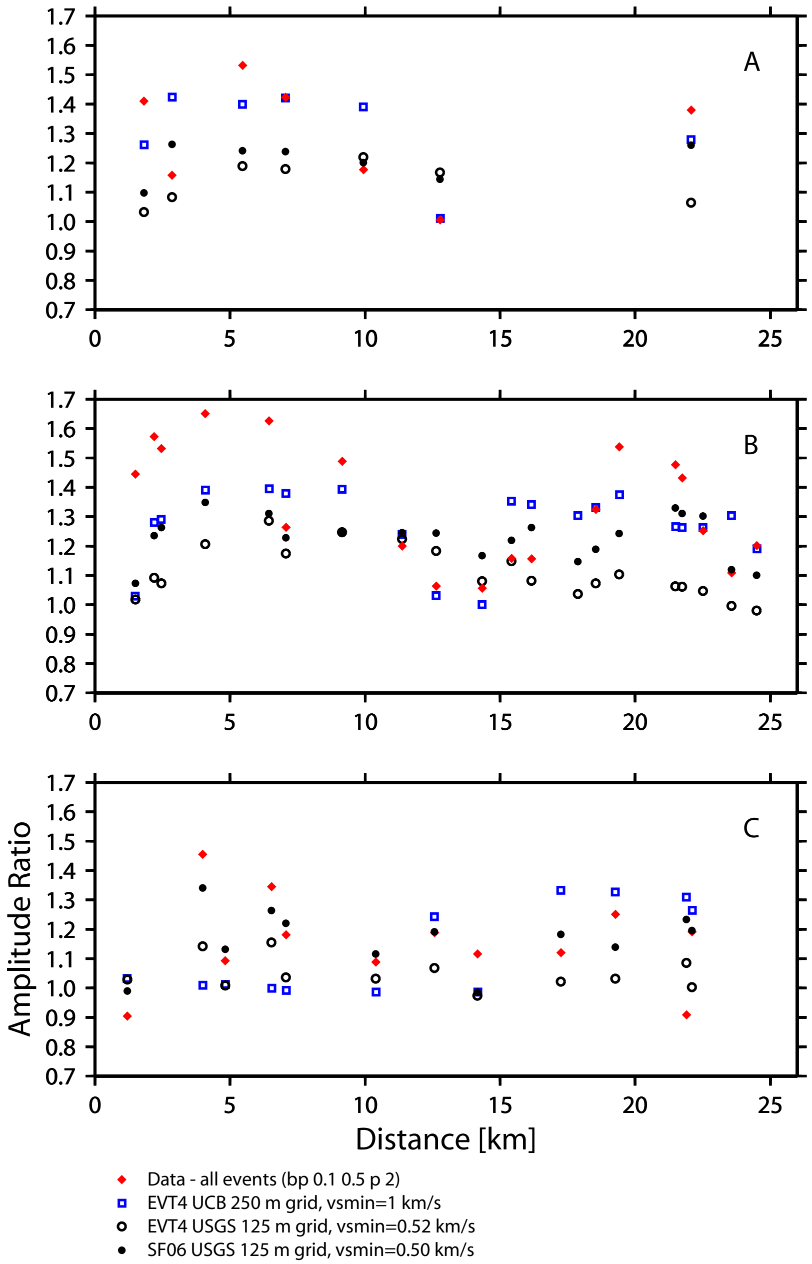

Figure 4.3: Relative amplitudes for the observed and simulated teleseismic waveforms. Presented values are relative to station 186, located south of the Cupertino basin (see Fig. 2.3). Waveforms have been bandpass filtered between 0.1 and 0.5 Hz.

Chapter 5

Inversion for the velocity structure of the Santa Clara Valley, California

Summary

I started to develop a simultaneous inversion of the teleseismic, local earthquake, and microseism data to refine the velocity structure within the SCV basins. The observation equation is first linearized and then solved iteratively by singular value decomposition. Synthetic waveforms as well as sensitivity functions are needed to obtain the solution. I use the elastic finite-difference code E3D to calculate the waveforms and obtain the sensitivity functions numerically, by taking the difference of waveforms from perturbed and unperturbed models. Preliminary synthetic tests using the teleseismic data show that the method is stable and can be used to improve the velocity structure within the basin.

5.1 Introduction

Results presented in Chapters 2 to 4 showed that teleseismic, local earthquake, and microseism data are all sensitive to the SCV basin structure. This suggests that they can be used together to further improve the 3D velocity model. I started to develop a simultaneous inversion of the observations from the three datasets to refine the USGS 3D model velocity structure within the SCV basins. To reduce the extremely large model space, I invert for the velocity structure within the basins while the basin geometry, as defined in the USGS ver. 2 velocity model, is held fixed. Basin geometry in the USGS model was mainly constrained by the inversion of the gravity data [*Jachens et al.*, 1997; *Chuchel & Jachens*, 1990] and is one of the better known parameters in the model (R. Jachens, personal communication, 2005). Results from more recent reflection and refraction studies [*Catchings et al.*, 2005; *Catchings et al.*, 2006] confirmed the general basins geometry along their profiles.

I use the 3D elastic finite-difference code E3D to simulate the teleseismic, local, and microseism wavefields for the models with increasing levels of complexity in the basins. I prepared scripts that identify the SCV basins in the USGS model following the velocity contrast at the bottom of the basins. Once I have the SCV basins singled out from the rest of the model, I can assign them different properties. I prepared four variations of the model within the basin:

1. Laterally uniform velocity with a single velocity gradient.
2. Three vertical regions, each with its own velocity gradient.
3. Six 1-km thick horizontal layers with constant velocity.
4. Multi-layered constant velocity layers draped over the basin geometry.

Because of the computational limitations, the slowest velocities in the model were increased to a minimum S-wave velocity of 1 km/s. The slowest P-wave velocity was 1.75 km/s. The modeling was performed using a 250-m grid spacing. The size of the model used for modeling the teleseismic events was 100.5 × 100.5 × 40 km. To model the plane wave from the teleseismic events, I used a disc of point sources in the deepest homogeneous layer of the model, representing the upper mantle. To simulate the microseisms I used a localized source of isotropic Rayleigh waves located offshore. The results of the f-k analysis of the observed and simulated microseisms are consistent with the findings of the study by *Schulte-Pelkum et al.* [2004] in which the microseisms display strong directionality in their propagation and source localization.

In the next step I use the simulated wavefields to do the inversion following the approach developed by *Aoi* [2002]. In his study, *Aoi* [2002] used the inversion scheme to estimate the 3D basin shape from the long-period strong ground motions. In this work I keep the basin geometry fixed and invert for the velocity structure within the basins.

5.2 Formulation of the inversion

To obtain the model that best describes the data, the observation equation

$$u_i(x_m, t_n; \mathbf{p}) \cong \tilde{u}_{imn} \tag{5.1}$$

needs to be solved. The $u_i(x_m, t_n; \mathbf{p})$ is the i-th component of the synthetic waveform for the model parameter vector $\mathbf{p}$ and $\tilde{u}_{imn}$ is the i-th component of the data observed at x_m at the n-th time step t_n. The equation is nonlinear with regard to the model parameter $\mathbf{p}$ and in order to solve it iteratively, the left side is first expanded in Taylor series about the parameter $\mathbf{p}^0$ (initial model). It is then linearized by omitting the higher-order terms. Resulting linearized observation equation for the l-th iteration can then be written as

$$u_i(x_m, t_n; \mathbf{p}^l) + \sum_{k=1}^{K} \left.\frac{\partial u_i}{\partial p_k}\right|_{\mathbf{p}=\mathbf{p}^l} \delta p_k \cong \tilde{u}_{imn} \tag{5.2}$$

where $\mathbf{p}^l$ is the model parameter estimated in the (l-1)-th iteration. To solve this nonsquare matrix equation, we need to obtain the sensitivity functions $\frac{\partial u_i}{\partial p_k}$. They can be calculated numerically by using the finite-difference approximation by first modeling the waveforms for the perturbed and unperturbed models and then calculating the difference of the waveforms

$$\left.\frac{\partial u_i}{\partial p_k}\right|_{\mathbf{p}=\mathbf{p}^l} \cong \frac{u_i(x_m, t_n; \mathbf{p}^l + \Delta\mathbf{p}_k^l) - u_i(x_m, t_n; \mathbf{p}^l)}{\Delta p_k} \tag{5.3}$$

where $\Delta\mathbf{p}_k^l = (0, 0, ..., \Delta p_k, ..., 0)$. The equation 5.2 now represents a set of simultaneous linear equations whose coefficient matrix is nonsquare and singular value decomposition method (SVD; [*Press*, 1999]) can be used to solve it. The model parameters are iteratively modified by linear iteration method until the residual

$$\sqrt{\sum_{i,m,n} (\tilde{u}_{imn} - u_i(x_m, t_n; \mathbf{p}^l))^2} \tag{5.4}$$

is sufficiently small and the model has converged [*Aoi*, 2002].

5.3 Preliminary results

In the test inversions I used synthetic waveforms obtained with a selected target model instead of true observations. This was to test the inversion method while the target 3D velocity structure was known and based on the USGS ver. 2 model. I also used teleseismic data from a set of 38 stations. The structure within the basins was laterally uniform with a single velocity gradient. One example of the test inversion is presented below. The velocities and density of the target and of the starting model are listed in Table 5.1. The velocity and density gradients in the SCV basins in the target model were the same as in the USGS model. The velocity and density gradients in the starting model were 50% smaller than the USGS gradients in the SCV basins. The perturbation steps used for all six model parameters (P- and S-wave velocity and density at the surface and their gradients with depth) were 15% of their starting values.

The computations were performed on the BSL Linux cluster. The size of the model was $100.5\times100.5\times40$ km and the grid spacing was 250 m. The computation time for a single forward simulation that produced 60 s long waveforms was ~70 minutes when 16 cluster nodes and 2 processors per node were used. Each forward computation required ~4.5 GB of memory. To obtain the sensitivity functions (see equation (5.3)), waveforms for the perturbed and unperturbed model had to be forward modeled at every iteration step. Since six parameters were used, waveforms for each of the six models were computed at every iteration step. In addition, waveforms for the model obtained in the previous iteration (or the starting model for the first iteration) were also computed. The combined time for every iteration step was therefore about 500 minutes.

Results for a subset of four stations are presented in Figures 5.1 and 5.2 and the properties of the final model are listed in Table 5.1. Stations 120 and 238 are located over the basins, station 186 is south of the Cupertino basin, and station PG2 is between the basins (see Figure 2.3). Waveforms for the starting model and for a model from every iteration step are shown (solid lines) as well as the waveforms obtained with a target model (dotted). Waveforms were bandpass filtered between 0.1 and 0.5 Hz as the waveforms from the recorded teleseisms had most of the energy in this frequency band. Figure 5.1 shows first 20 s of the waveforms, the time window that was also used in the inversion. This time period includes the P-wave arrival as well as the P- to S-wave converted arrivals discussed in Chapter 2. Longer waveforms are shown in Figure 5.2. They include the arrival of the pP-wave that was also modeled, but not included in the inversion as it arrives after the first 20 s. The pP-wave was modeled following the approach described in Chapter 2.

In addition to the above presented result, other test inversions were performed. They included an example with the same target model as above, but with a faster starting model that included 25% faster velocities at the surface and 50% larger gradients than the target model. Also tested were the reverse combinations in which the above target and the starting model had reversed roles. In all of the tests so far the perturbation steps were 15% of the starting values.

Results from the test inversions performed so far showed that the method is stable and that four or less iteration steps were needed to reach the target model. Preliminary results also suggest that P- and S-wave velocity structure can be best resolved and that the density gradient is not resolved well (see Table 5.1). This indicates that it might be best not to include density as a free parameter in the inversion but rather link it to the S-wave velocity, or consider it a fixed parameter since it is reasonably well constrained by the gravity model used to construct the USGS SF06 model.

5.4 Conclusions

Velocity structure in the basins can be improved by the inversion of the teleseismic data. Previous results showed that local earthquake and microseism data are also sensitive to the basin structure and it should be possible to include them in the inversion and use all three datasets to improve the 3D velocity model in the basin.

Since the finite-difference code is used to calculate the sensitivity functions at each iteration step, this method can become computationally expensive, particularly if the model includes many free parameters and the number of iterations needed to reach the final model is not small. It is therefore important to use a simple model parameterization as well as to consider a hierarchical scheme that starts the inversion with a smaller number of parameters and later adds additional ones [*Aoi*, 2002]. Additional tests should also show if it is best to use all three datasets simultaneously or rather use the most robust data first. A hierarchical scheme for model parameters and data might work best to ensure stability and resolution at the minimum computational time.

5.5 Future plans

We will further test the presented inversion method. We will test how the inversion sensitivity and convergence are affected by the size of the perturbation step. We will also test what is the best perturbation step for each individual parameter. So far we used all 38 stations. In future work we will test how the station coverage affects the results.

The presented inversion example used only teleseismic waveforms. Future inversions will use additional parameters obtained from the local earthquake and microseisms data. For the local earthquakes, these parameters will include energy estimates and peak ground velocity values. For the microseisms data, the parameter that will be included in the inversion will be the value of the horizontal to vertical spectral ratio peak. Additional parameters that would characterize the teleseismic waves coda could also be added.

The same routines could easily be applied to a different basin geometry. In fact, increased computational capabilities in the future could enable us to add the parameters defining the basin topography into the inversion and obtain basin shape and its properties at the same time. Particularly sensitive to the basin shape are the P- to S-wave converted phases that are discussed in Chapter 2 and can be seen in

Figure 2.13. They should provide an important constraint for the basin shape.

Table 5.1: Velocities and density values in SCV basins for the target, starting, and final model obtained after four iterations. Listed are properties at the surface and their gradients with depth.

Parameter	Target model	Starting model	Final model (Iter. 4)
v_p $[km/s]$	2.187	1.75	2.107
v_s $[km/s]$	1.25	1.0	1.29
ρ $[g/cm^3]$	2.5	2.0	2.575
$\partial v_p/\partial z$ $[km/s \ / \ km]$	0.614	0.307	0.677
$\partial v_s/\partial z$ $[km/s \ / \ km]$	0.286	0.143	0.265
$\partial \rho/\partial z$ $[g/cm^3 \ / \ km]$	0.107	0.053	0.043

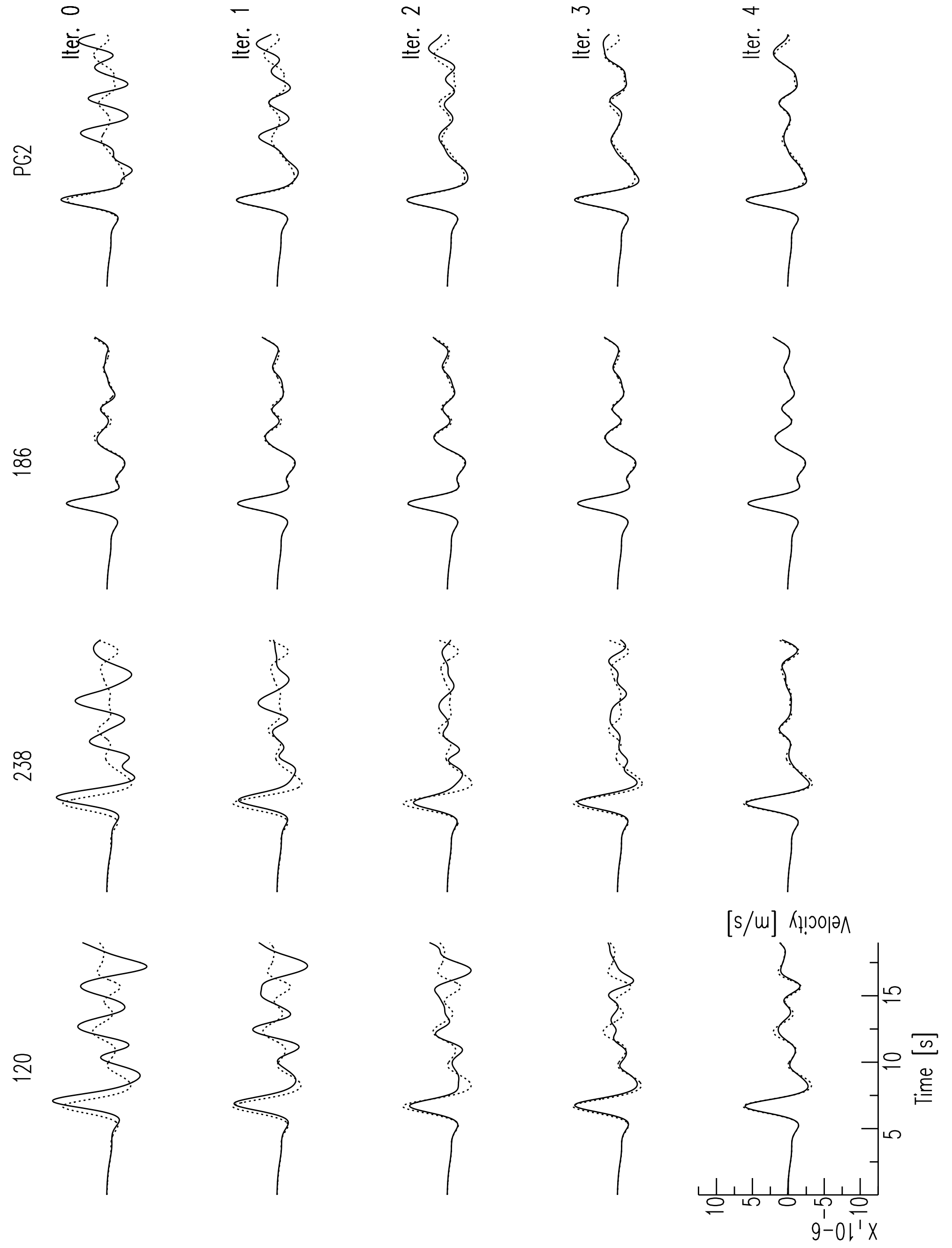

Figure 5.1: Results from a test inversion. Waveforms for the four SCV station are shown for the starting model (solid, top row) and for a model as it was modified after each iteration (solid, bottom rows). Waveforms obtained with the target model are shown for comparison (dotted). Shown are first 20 s of the waveforms as only this time window was used in the inversion.

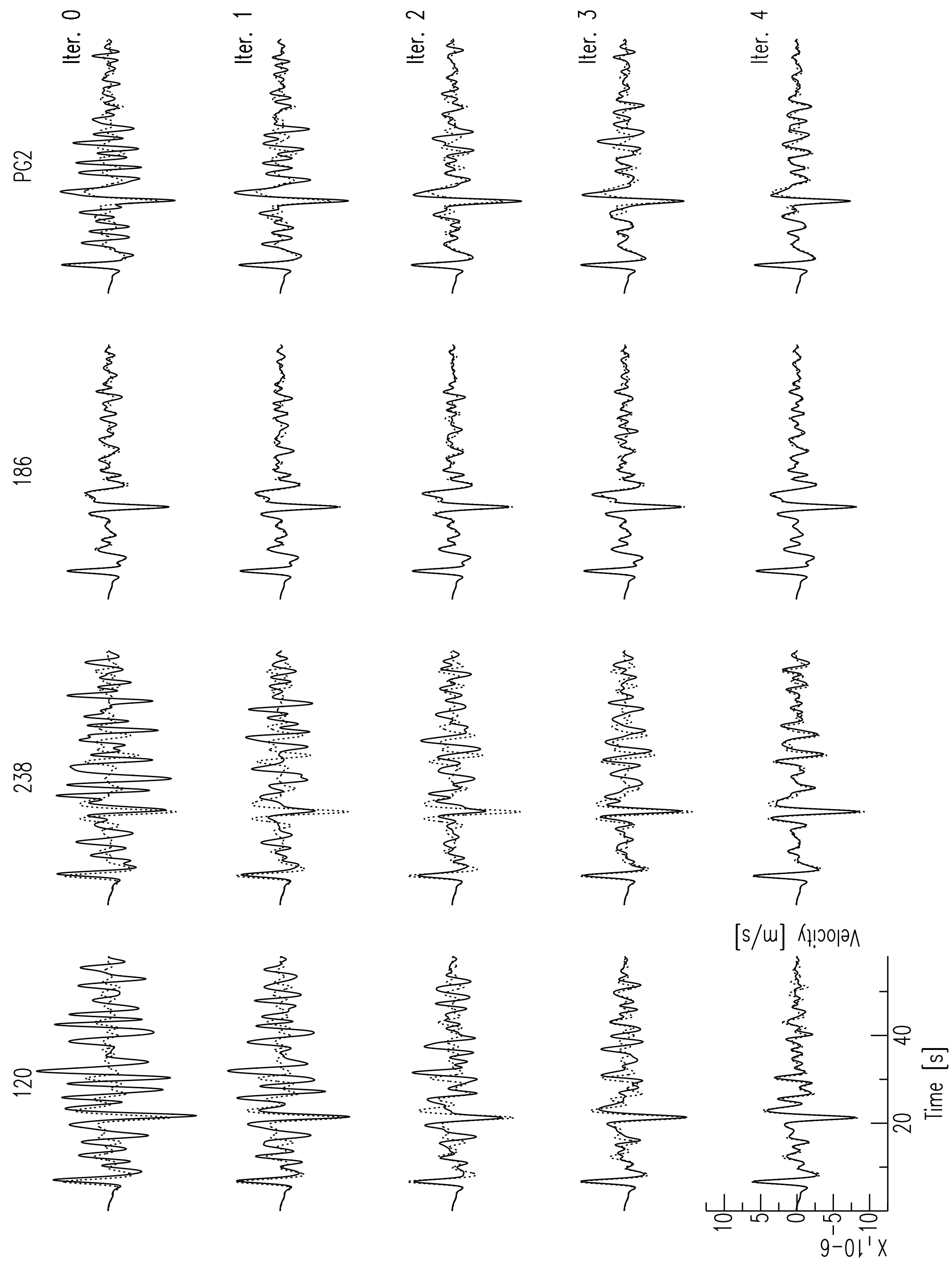

Figure 5.2: Same as Figure 5.1, only that 60 s time window is now shown. In addition to P-wave, pP-wave can also be seen arriving just after the first 20 s. Waveforms for the first 20 s were used in the inversion.

Chapter 6

The Monterey Bay broadband ocean bottom seismic observatory

This chapter was published in *Annales Geophysicae* [*Romanowicz et al.*, 2006] with the title 'The Monterey Bay broadband ocean bottom seismic observatory'.

Summary

We report on the installation of a long-term buried ocean-floor broadband seismic station (MOBB) in Monterey Bay, California (USA), 40km off-shore, at a water depth of 1000 m. The station was installed in April 2002 using a ship and ROV, in a collaborative effort between the Monterey Bay Aquarium Research Institute (MBARI) and the Berkeley Seismological Laboratory (BSL). The station is located on the western side of the San Gregorio Fault, a major fault in the San Andreas plate boundary fault system. In addition to a 3-component CMG-1T seismometer package, the station comprises a current meter and Differential Pressure Gauge, both sampled at high-enough frequency (1 Hz) to allow the study of relations between background noise on the seismometers and ocean waves and currents. The proximity of several land-based broadband seismic stations of the Berkeley Digital Seismic Network allows insightful comparisons of land/ocean background seismic noise at periods relevant to regional and teleseismic studies. The station is currently autonomous. Recording and battery packages are exchanged every 3 months during scheduled one day dives. Ultimately, this station will be linked to shore using continuous telemetry (cable and/or buoy) and will contribute to the earthquake notification system in Northern California. We present examples of earthquake and noise data recorded during the first 6 months of operation of MOBB. Lessons learned from these and continued recordings will help understand the nature and character of background noise in regional off-shore environments and provide a reference for the installation of future off-shore temporary and permanent broadband seismic stations.

6.1 Introduction

Two-thirds of the earth's surface is covered by oceans, and this represents a significant challenge for the investigation of global scale dynamic processes in the earth's interior, as well as tectonic processes at ocean-continent boundaries. In particular, the need for long term ocean floor seismic observatories has now been widely recognized, and several national and international efforts are underway to resolve the technological and logistical issues associated with such deployments [e.g., *COSOD II*, 1987; *Purdy and Dziewonski*, 1988; *Purdy*, 1995; *Forsyth et al.*, 1995; *Montagner and Lancelot*, 1995].

Following pioneering efforts in the 1960's [*Sutton et al.*, 1965], a number of pilot projects have been conducted in the last ten years, coordinated internationally by ION

[International Ocean Network, *Suyehiro et al.*, 1995], to test technological solutions and demonstrate the feasibility of seafloor seismic observatories either in boreholes or on the ocean floor [e.g., *Suyehiro et al.*, 1992; *Beranzoli et al.*, 1998]. In particular, in 1992, a French experiment involving the manned underwater vessel *Nautile* installed two sets of 3-component broadband seismometers in the north-equatorial mid-Atlantic, one directly on the sea-floor, and the other, using the Ifremer re-entry vessel *NADIA*, at 300 m depth inside ODP hole 396B [*Montagner et al.*, 1994a,b]. The data comparison between the two systems seemed to indicate that the ocean-floor installation was quieter at long periods [*Beauduin et al.*, 1996], however, this remained controversial, as only 10 days of data were acquired in this experiment, and water circulation may have increased the noise in the borehole. Since then, several other buried seafloor installations have been deployed in the deep oceans, some of them making use of abandoned submarine telecommunications cable [e.g., *Butler et al.*, 2000; *Kasahara et al.*, 1998].

During the OSN1 experiment in 1998 [e.g., *Collins et al.*, 2001] 3 broadband systems were installed 225 km southwest of Oahu (Hawaii), at a water depth of 4407 m, one on the seafloor, one buried, and the third one at 248 m below the seafloor, in a borehole drilled by the ODP in 1992 for this purpose [*Dziewonski et al.*, 1992]. Data were collected for 4 months and demonstrated the importance of burying the seismometer package below the seafloor to obtain good coupling with the ground and ensure good quality of data at long periods. The OSN1 experiment also demonstrated that a borehole installation can be quieter at teleseismic body wave periods than a buried or sea-floor deployment, because it avoids signal-generated noise due to reverberations in the near surface sediment layers. This was confirmed by the long-term Japanese NEREID observatory deployment, which also documented that a properly cemented ocean-floor borehole in basement rock can be very quiet at long periods as well [*Araki et al.*, 2004].

Long-term ocean floor observations are also necessary to better constrain regional tectonics, such as on the western margin of North America, where tectonics and seismic activity do not stop at the continental edge. For example, in California, the zone with most abundant seismicity is associated with the Mendocino Triple Junction, and is mostly off-shore. Much effort has been expended to deploy networks of seismic stations in the western U.S., most recently broadband stations, with multiple goals of monitoring the background seismicity, understanding modes of strain release, documenting seismic hazards and providing constraints on crustal and upper-mantle structure. However, because there are very few off-shore islands in Central and Northern California, practically all stations are located on the continent. As a consequence, the study of plate-boundary processes, as afforded by regional seismological investigations, is heavily squewed on the continental side of the San Andreas Fault (SAF) system. Offshore seismicity is poorly constrained, both in location and in mechanisms, as is crustal structure at the continental edge.

While consensus seems to have been reached that permanent, borehole installations are best for seafloor deployments of broadband seismometers, they are very expensive: the spatial resolution required for regional studies, either off-shore or in the middle of the oceanic plates, may not be achieved for many years to come. It is therefore important to conduct pilot studies to determine how to optimally deploy ocean floor broadband systems, and in particular how to minimize the strong perturbing environmental effects, both through improved installation procedures, and through a posteriori deconvolution of ocean current, tide, pressure, temperature, and other such signals that can be recorded simultaneously.

In the summer of 1997, the international MOISE experiment (Monterey Ocean bottom International Seismic Experiment) allowed us to collect 3 months of broadband seismic data from a sea-floor system installed 40 km off-shore in Monterey Bay, in a cooperative experiment between MBARI, IPG (Paris, France) and UC Berkeley [e.g., *Stakes et al.*, 1998; *Romanowicz et al.*, 1998]. During this experiment, the feasibility of performing under-water electrical and data cable connections between instruments, using an ROV operated from a ship, were successfully illustrated for the first time. The MOISE experiment also demonstrated the sensitivity of ocean floor systems to sea currents at long periods and the importance of simultaneous recording of current velocity and direction, at a sampling rate sufficient for quantitative comparisons with seismic data: the conventional current meter sampling rate used by oceanographers (4 sample points once every 4 minutes), was too low to correct the MOISE seismic data for noise generated by currents, although this is theoretically possible [e.g., *Stutzmann et al.*, 2001].

The Monterey bay Ocean Broad Band Observatory [MOBB, *McGill et al.*, 2002; *Uhrhammer et al.*, 2002; *Romanowicz et al.*, 2003] was installed in April 2002. It is a direct follow-up of MOISE, and capitalizes on the lessons learned during that pilot experiment. The ultimate goal of this collaborative project between MBARI and the Berkeley Seismological Laboratory (BSL) is to link the MOBB station by continuous telemetry to the shore, so that MOBB becomes part of the Berkeley Digital Seismic Network [BDSN, *Romanowicz et al.*, 1994]. The data can then be contributed to the real-time earthquake monitoring system in Northern California [*Gee et al.*, 2003]. The opportunity to do so awaits the installation of the MARS cable (Monterey Accelerated Research System; http://www.mbari.org/mars). In the meantime, data are recorded on-site and retrieved every 3 months using MBARI's ship and ROV, and data analysis is focused on understanding sources of background noise at long periods in this relatively near-shore environment. We view MOBB as the first step towards extending the on-shore broadband seismic network in Northern California to the seaside of the North-America/Pacific plate boundary, providing better azimuthal coverage for regional earthquake and structure studies. In what follows we describe this observatory and discuss some of the data recorded during the last 18 months.

6.2 Location, instrument packages and deployment

The MOBB station is located at a water depth of 1000 m, 40 km off-shore in Monterey Bay, in an area called “Smooth Ridge” on the western side of the San Gregorio fault, and closer to it than was MOISE (Figure 6.1). The planned MARS cable route is down the center of Smooth Ridge and with a termination near the MOBB site.

The San Gregorio fault (SGF) splays from the SAF at the Golden Gate and extends south past the San Francisco peninsula and Santa Cruz mountains, mostly off-shore. It is the principal active fault west of the SAF in central coastal California, yet it remains the largest known fault whose seismogenic potential is not well characterized in this region. However, *Begnaud and Stakes* (2000) and *Begnaud et al.* (2000) used a temporary offshore seismic network to demonstrate the unusually high seismicity levels of the northern SGF, dominated by compressional mechanisms as well as an east-dipping focal plane [*Simila et al.*, 1998]. The SGF is thought to be capable of $M > 6$ earthquakes, making the MOBB site particularly interesting from the tectonic and seismic hazards point of view. Using refined crustal velocities based on the results of *Begnaud et al.* (2000), *Simila et al.* (1998) relocated the 1926 $M > 6$ doublet to show that the first event occurred on the northern SGF followed by the second on the adjacent Monterey Bay Fault Zone.

The coseismic geodetic slip on the SAF during the 1906 earthquake and the late Holocene geologic slip rate on the San Francisco peninsula and southward are about 50-70% of their values north of San Francisco [*Thatcher et al.*, 1997; *Schwartz et al.*, 1998]. Review by the Working Group on Northern California Earthquake Potential (1996) suggests that the slip rate on the SAF in the Santa Cruz mountains is about 14 mm/yr, which is 58% of the slip rate north of San Francisco, so the rest of the slip must be accommodated by other faults, both on-land and off-shore. This slip gradient reflects partitioning of the plate boundary slip onto the San Gregorio, Sargent and other faults south of the Golden Gate. Because of the limited onshore extent, few detailed geologic studies have been conducted to evaluate the style and rate of late

Quaternary deformation along this complex fault zone.

The ocean-bottom MOBB station currently comprises a three-component seismometer package, a current meter, a differential pressure gauge (DPG) and a recording and battery package. The data logger, battery, and DPG are contained in a modular frame which is removed and replaced when the ROV services the system. This configuration permits hardware and software upgrades to take place as required. For instance, the DPG [*Cox et al.*, 1984] was not present in the initial deployments, but was added later during a data retrieval dive in September, 2002.

The seismic package contains a low-power (2.2 W), three-component CMG-1T broadband seismometer system, built by Guralp, Inc., with a 24-bit digitizer, a leveling system, and a precision clock (Figure 6.2a). The seismometer package is mounted in a cylindrical titanium pressure vessel 54 cm in height and 41 cm in diameter (Figure 6.2b), custom built by the MBARI team and outfitted for underwater connection. The component design of the instruments permit the sensor, datalogger, and current meter to be carried to the seafloor separately, then tested and connected in situ. This component design permits us to update software, change batteries and replace instruments without disturbing the sensor package. The system has been designed to permit a GPS time mark, applied during an ROV visit, to establish the offset and drift rate of the Guralp clock. These errors are recorded and the timing of the seismic data is corrected in post-processing. The clock is not adjusted in situ to prevent abrupt jumps in the time marking of the data. Establishing these corrections on the seafloor and after the system has reached thermal equilibrium is a critically important feature for long-term autonomous deployments.

Because of the extreme sensitivity of the seismometer, air movement within the pressure vessel must be minimized. In order to achieve this, after extensive testing at BSL, the top of the pressure vessel was thermally isolated with two inches of insulating foam and reflective Mylar. The sides were then insulated with multiple layers of reflective Mylar space blanket, and the vessel was filled with argon gas (Figure 6.2b).

The low thermal conductivity of argon allows better thermal insulation. This resulted in significant noise reduction on the 3 components, in the 10-100 sec period range (Figure 6.3).

Near-bottom water currents are measured by a Falmouth Scientific 2D-ACM acoustic current meter. It is held by a small standalone fixture and measures the current speed and direction about one meter above the seafloor. The recording system is a GEOSense LP1 data logger with custom software designed to acquire and record digital data from the Guralp sensor and from the current meter over RS-232 serial interfaces, as well as analog data from the DPG. The seismic data are sampled at 20 Hz and the current meter and DPG are sampled at 1 Hz. Data are stored on a 6 GB, 2.5-inch disk drive. All the electronics, including the seismometer, current meter, and DPG, are powered by a single 10 kWh lithium battery.

All installations were done using the MBARI ship *Point Lobos* and the ROV *Ventana.* Prior to the instrumentation deployment, the MBARI team manufactured and deployed a 1181 kg galvanized steel trawl-resistant bottom mount to house the recording and power systems, and installed a 53 cm diameter by 61 cm deep cylindrical PVC caisson to house the seismometer pressure vessel. The bottom mount for the recording system was placed about 11 m away from the caisson to allow the future exchange of the recording and battery package without disturbing the seismometer. The seismometer package was tested extensively at BSL, then brought to MBARI where its internal clock drift was calibrated against GPS time in an environmental test chamber at seafloor temperature.

The actual deployment occurred over 3 days (04/09-11/2002). On the first dive, the seismometer package was lowered into the PVC caisson (Figure 6.4a), and its connection cable brought to the site of the recording unit. On the second dive, the recording package was emplaced in its trawl-resistant mount (Figure 6.4b), and connected to the seismometer package (Figure 6.4c). Tiny (0.8 mm diameter) glass beads were poured into the caisson until the seismometer was completely covered, to further isolate it from water circulation, as dictated by lessons learned from previous experiments [e.g., *Sutton et al.*, 1981; *Duennebier and Sutton*, 1995]. The seismometer package is now buried at least 10 cm beneath the seafloor. On the third dive, the ROV immobilized the cable between the seismometer and recording package with steel "wickets" inserted into the sediment. It then connected the seismometer to the recording system, leveled and recentered the seismometer, and verified that everything was operational. Finally, the current meter was installed and connected to the recording system.

On April 22nd, 2002, the ROV returned to the MOBB site to check the functioning of the seismometer and recording system. Some slight settling of the seismometer pressure vessel had occurred, and so the seismometer was recentered electronically. Over 3 MB of data were then downloaded from the recording system over a period of about two and a half hours, using a 9600 bps serial data connection through the ROV. These data included the recordings of two regional earthquakes in California and two teleseismic events that occurred in Guerrero, Mexico, and in Northern Chile.

The site was revisited two months later, on June 27th, to check the functioning of the system and replace the data recording and battery module, in the first of a series of such dives planned for the next 3 years. The following functions were performed:

1. Disconnected the current meter and seismometer from old datalogger.
2. Removed old datalogger frame with datalogger and batteries from the trawl-resistant mount.
3. Installed new datalogger frame in the trawl-resistant mount.
4. Connected the current meter to the new datalogger.
5. Connected the ROV to the new datalogger and verified that the datalogger was operational.
6. Connected the seismometer to the new datalogger and monitored its reboot.

7. Centered the seismometer.
8. Re-centered the seismometer.
9. Verified that the Guralp was receiving the GPS clock signals from the ROV (NMEA time messages and pulse per second), and recorded the clock offset. During this dive, the Guralp clock was not resynchronized to GPS time.
10. Brought the old datalogger frame with datalogger and batteries back to the ship.

Figure 6.5 shows the evolution of the tilt signal obtained from the seismometer mass position channels (MMZ, MME, MMN), for the first 7 months of deployment. These data indicate that the seismometer package has been experiencing an exponentially decaying tilt in a south-southwesterly direction, which is also the down slope direction (e.g., Figure 6.1). The large step on day 112 (04/22/2002) was caused by re-centering, when the instrument was checked 12 days after installation. The small step on day 134 (05/14/2002) is coincident with the occurrence of a $M_w 4.96$ earthquake which occurred 55 km N59W of MOBB on the San Andreas fault near the town of Gilroy. The instrument was recentered again on day 178 (06/27/2002). The slow drift rate of the horizontal component mass positions in the latter half of the plot (day 263 onward) indicates that the OBS pressure vessel stabilized in the ocean floor sediments after about two and a half months after deployment. On the MMZ component, the semidiurnal gravitational tide is visible, riding on the tilt signal. As with the horizontal components, the largest signals are associated with rapid changes in the second derivative of the tilt, caused by recentering or by significant ground shaking (day 134).

During the first two months of recording, many regional and teleseismic events were recorded, as described later. The site has been revisited regularly every three months since. During each visit, the datalogger and battery packages are changed, the seismometers are recentered, and the clock re-synchronized to GPS time. Due to multiple datalogger problems (hardware and software) encountered in the first half of 2003, the best data available so far span the time period April-December 2002, as illustrated below.

6.3 Examples of data and preliminary analysis

Figure 6.6 shows the location of MOBB with respect to the nearby BDSN stations. Notably, we will be discussing comparisons between recordings on the ocean floor (MOBB), in the noisy Farallon Island environment (FARB) and on the continent (SAO, JRSC).

Figure 6.7 shows power density spectra for two different time periods, comparing background noise at MOBB and three land stations of the BDSN network. Day 143 (05/23/2002) is a "quiet" day, as assessed from the ocean wave data recorded on the NOAA buoy in Monterey Bay, whereas day 350 (12/16/2002) is a "stormy" day (spectral ocean wave density is an order of magnitude higher at around 30 sec). Increased noise level for periods between 20 and 500 sec, due to ocean currents and infragravity waves, is observed at MOBB on all 3 components on the stormy day, but only on the vertical component on the quiet day. The spectral width of the noisy long-period band is larger on the stormy day, and, interestingly, it also corresponds to a band of increased noise at the Island site FARB, where it is largest on the East component. This most likely indicates loading of shallow water around the small Farallon Island by gravity waves, similarly to what is observed in Hawaii [*Stephen et al.*, 2003]. We are currently investigating the source of this noise in more detail. In particular, it should be correlated with the DPG data, if it is indeed due to gravity waves generated by breaking waves at the coastline [*Webb et al.*, 1991]. The bell shape of this noise peak is in agreement with theoretical calculations by *Araki et al.* (2003). On the other hand, the noise level at MOBB between 30 and 100 sec on a quiet day is comparable to the noise level at the island station FARB on a stormy day. The "low noise notch" [*Webb*, 1998] is very narrow at MOBB (10-30 sec), and contains the single-frequency micro-seismic peak (12 sec), but the level of noise is comparable to the land station YBH, one of the quietest BDSN stations. The corresponding "double-frequency" micro-seismic peak around 6 sec is visible at all stations most of the time, but on day 350, it is hidden by higher amplitudes between 2 and 4 sec at MOBB. On day 143, two additional narrow-band micro-seismic peaks are clearly resolved at MOBB (around 2.5 and 4 sec). These could be related to a combination of local sea-state and distant storms [e.g., *Bromirski and Duennebier*, 2002]. They are clearly distinct in frequency from those observed in the open sea [e.g., *Stephen et al.*, 2003].

Noise levels at frequencies higher than 2 Hz and lower than 200 sec are comparable to those observed at some of the land stations. FARB (island site) is sometimes noisier at long periods, but the seismometer there is a Guralp CMG-3 with a shorter period high-pass corner (100 sec) than MOBB (360 sec) (Figure 6.8). Some of the longer period background noise is clearly correlated with currents that are associated with tidal flows, as was documented from MOISE [*Romanowicz et al.*, 1998; *Stutzmann et al.*, 2001]. Figure 6.9 shows a spectrum of the ocean current speed at MOBB computed using a 78-day time series, illustrating the dominant effects of tides on the bottom currents. This is also illustrated in Figure 6.10, which shows the corresponding distribution of current direction and velocity as a function of azimuth. With the current meter and DPG data sampled at 1 sec, it will now be possible to deconvolve the tide and current related noise from the MOBB data. Unfortunately, the DPG dataset is still too small (recording system problems since 01/01/03) to assess the effectiveness of such a deconvolution.

Figures 6.11- 6.14 illustrate observations that have been recorded at MOBB during the two months period 04/10/2002-06/28/2002, and which were retrieved during the first datalogger exchange, on 06/29/2002.

Figure 6.11 shows a component-by-component comparison of the recording of the 04/26/2002 M_w7.1 teleseism in the Mariana Islands at MOBB and 3 nearby BDSN stations (see location on Figure 6.6). The comparison shows consistency between the recordings of MOBB and nearby stations. On the horizontal components, there appears to be some signal-generated noise following the S waves and the Love wave, which is associated with ringing in the shallow mud layers as we will show below. In Figure 6.12, such ringing is clearly demonstrated for a deep earthquake (11/17/2002, depth 459 km, M_w7.3). Only the vertical component P-wave portion of the seismograms is displayed, filtered in two pass-bands. Signal-generated noise is very apparent in the P waves in the 0.03-0.3 Hz pass-band, where the P wave at MOBB displays a 3 min long coda. The ringing is narrow-band and disappears at frequencies lower than 0.1 Hz. Such observations should be helpful in understanding the triggering of submarine landslides in strong motion events, and may be relevant for ocean floor structures such as oil platforms and pipelines. On the other hand, this type of noise may be unavoidable in a shallow buried installation. We are currently evaluating ways to eliminate this signal-generated noise by post-processing. One possibility is to design an "observational" transfer-function, using data from near-by land stations that do not show the ringing. This is illustrated in Figure 6.13, where we show a comparison of original P-wave train at MOBB (blue) and JRSC (green) and "cleaned" MOBB data (red) after removal of the corresponding transfer function. We are working on combining this type of processing with direct modeling of the ringing effect, by computing theoretical transfer functions based on simple sediment layer models [*Uhrhammer et al.*, 2003; D. Dolenc et al., manuscript in preparation, 2006] that can be obtained from local studies [e.g., *Begnaud et al.*, 2000b].

Figure 6.14 shows the records, deconvolved to ground velocity, for a M_w3.63 regional event which occurred on 04/23/2002 on the SAF at a distance of 53.4 km from MOBB. The very large S-wave pulse on the horizontal components as well as the subsequent ringing are likely due to site response, as observed for the teleseismic events and could be similarly removed. On the vertical component, the water reflection of the P wave is clearly seen 1.3 sec after the P wave. In spite of these strong site effects, these data can be used in moment tensor studies, as illustrated in Figure 6.15a, which shows the results of a moment tensor inversion using a time domain whole waveform methodology [*Dreger & Romanowicz*, 1994]. A robust solution is obtained using data from 5 stations, including data from MOBB. The waveform fit at MOBB is outstanding with a 92.8% variance reduction. The addition of MOBB to the existing BDSN stations in this particular case provides an additional SH lobe but, since 3 SH lobes are already sampled by other BDSN stations, this particular strike-slip mechanism is well constrained in any case. However, this example serves to show that the MOBB data are well calibrated and have potential for providing valuable constraints in moment tensor studies of events of other types, such as reverse fault events in the Coast Ranges or strike slip events on faults closer to the shore or offshore.

To further demonstrate the consistency of the MOBB data, we also show the results of a single station moment tensor inversion using only MOBB, and the comparison of the corresponding synthetic predictions with the actual data at the four other BDSN stations (Figure 6.15b). The single station solution results in a nearly identical focal mechanism, but a slightly larger CLVD component and scalar moment, which is not unlike other single station inversions.

6.4 Discussion and future work

Data collected at the MOBB site can be used for several purposes. They provide complementary constraints for regional crustal and upper mantle structure to land-based broad band stations, as well as for the study of earthquakes along the San Andreas fault system. Currently, they are noisier than records from land-based stations, so that only relatively large events can be successfully analyzed. As we have seen, there are two sources of increased noise: signal-generated noise due to reverberation in the sediment pile, and background noise generated by currents as well as local and distant waves in the ocean. The first type of noise can be dealt with by designing appropriate deconvolution filters. In particular, the vicinity of high quality broadband land stations of the BDSN provides a helpful reference. The second type of noise is complex and time variable, however, the combination of MOBB and BDSN seismic data, current meter and DPG data, sampled at sufficiently high rates, as well as local and regional buoy data, provides a promising dataset to try to reduce the MOBB background noise - at least in the infragravity wave band. Ultimately, the level of success that we may reach in this endeavor will provide a reference for what can be expected of data from shallow-buried broadband ocean bottom systems.

Finally, the collection of these different types of data and their geographical distribution also provides an opportunity to further study the generation of such infragravity waves, at least in the particular setting of a relatively shallow ocean bay, as was pioneered by *Bromirski and Duennebier* (2002).

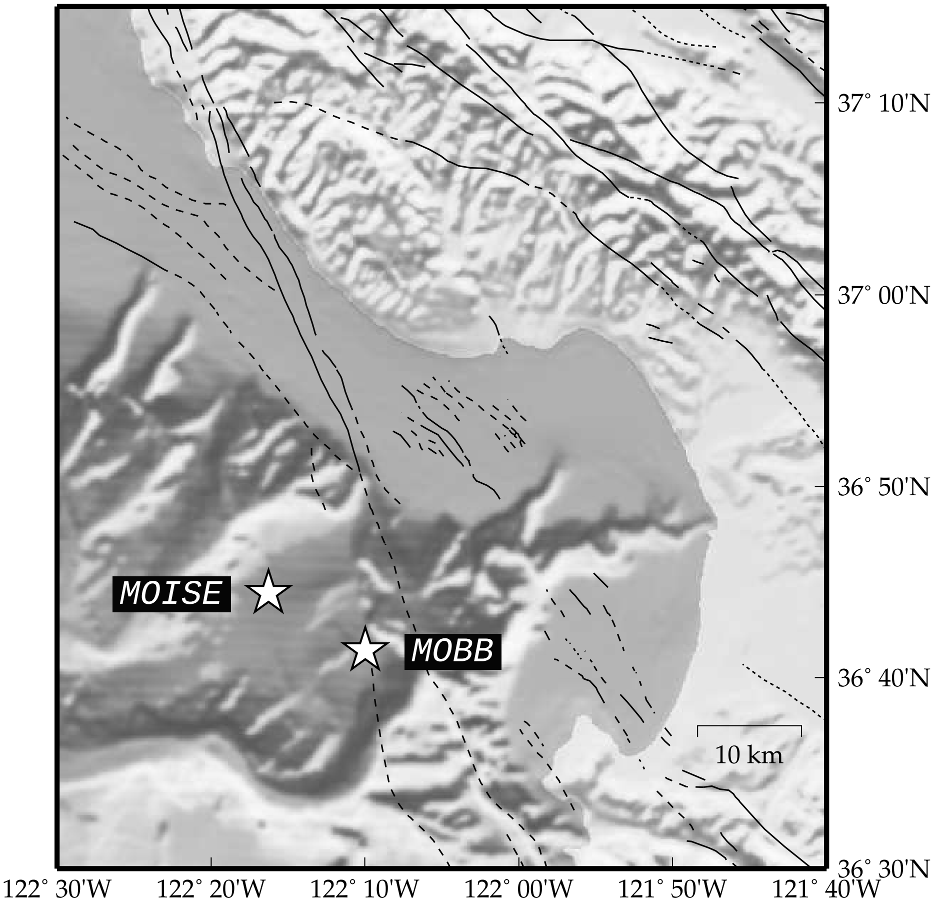

Figure 6.1: Location of the MOBB and MOISE stations in Monterey Bay, California, against seafloor and land topography. Fault lines are from the California Division of Mines and Geology database. MOBB is located at a water depth of 1000 m.

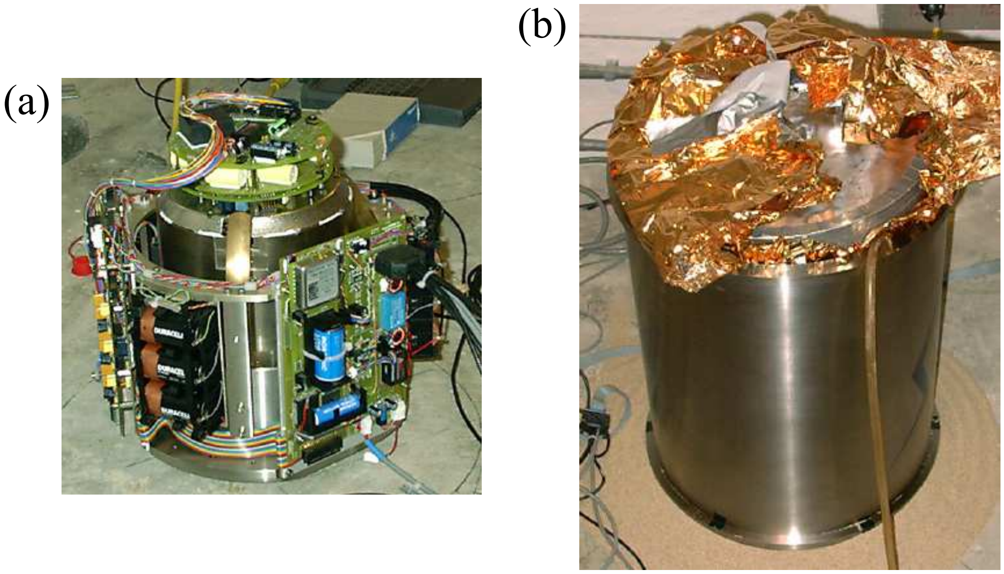

Figure 6.2: (a) Photo of a Guralp CMG-1TD seismometer in the Byerly Vault (BKS). Shown are the various circuit boards on the sides and the top of the sensor package. Three of the nine batteries used by the leveling system are on the left front and the system clock is on the circuit board on the right. The seismometers are in the μ metal shielded container mounted on leveling gimbals in the center. (b) Photo of the titanium pressure vessel containing the CMG-1TD and resting on a ~1 cm thick bed of kiln dried fine sand on the concrete pier at BKS, for the purpose of noise comparisons (B. Uhrhammer et al., manuscript in preparation, 2006).

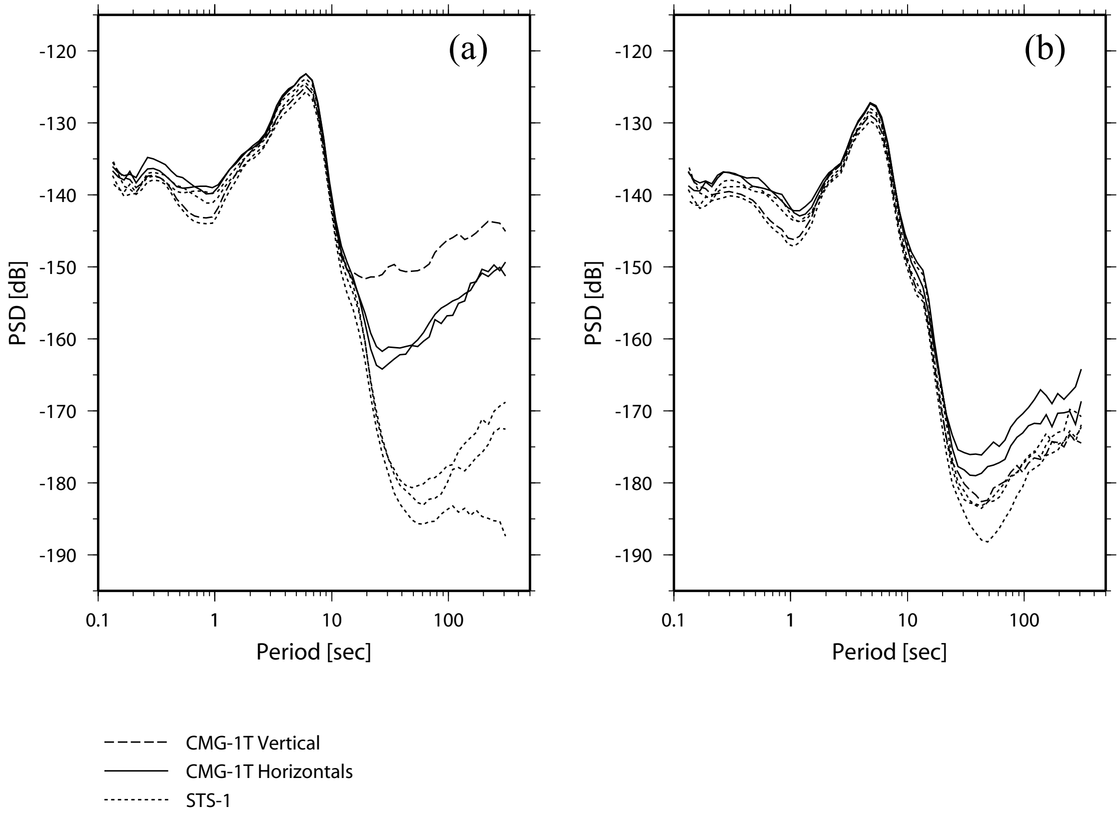

Figure 6.3: Comparison of typical background noise PSD levels observed by the CMG-1TD and the co-sited STS-1's in the BKS vault, (a) before and (b) after it had been installed in the titanium pressure vessel, appropriately insulated and purged with argon gas. The large dashed line and the solid lines are the Z component and horizontal component PSD's, respectively, and the small dashed lines are the STS-1 PSD's. Note that the CMG-1TD PSD levels are within ~5 dB of the STS-1 PSD levels at long periods after insulation (B. Uhrhammer et al., manuscript in preparation, 2006).

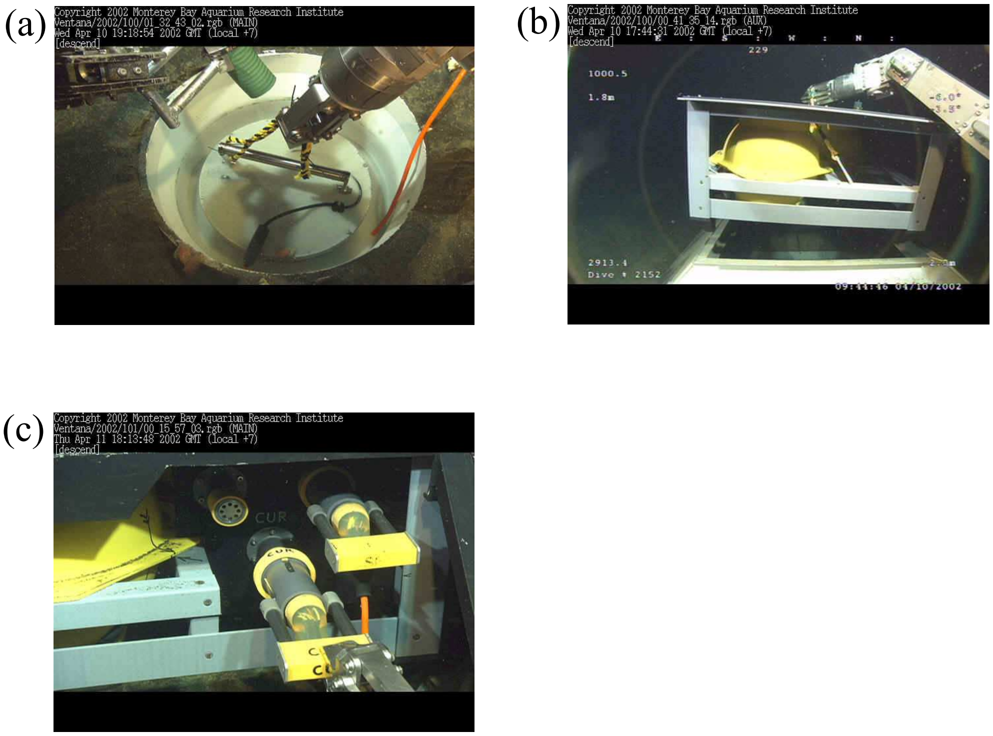

Figure 6.4: MOBB installation snapshots. (a) The seismometer package is being lowered into the hole bounded by the PVC pipe, held by the arm of the ROV *Ventana*. (b) The recording and battery package is being installed inside the trawl-resistant mount. (c) The ROV arm (at front) is connecting the current meter cable to the recording system. The connector of the seismometer package on the right is already in place.

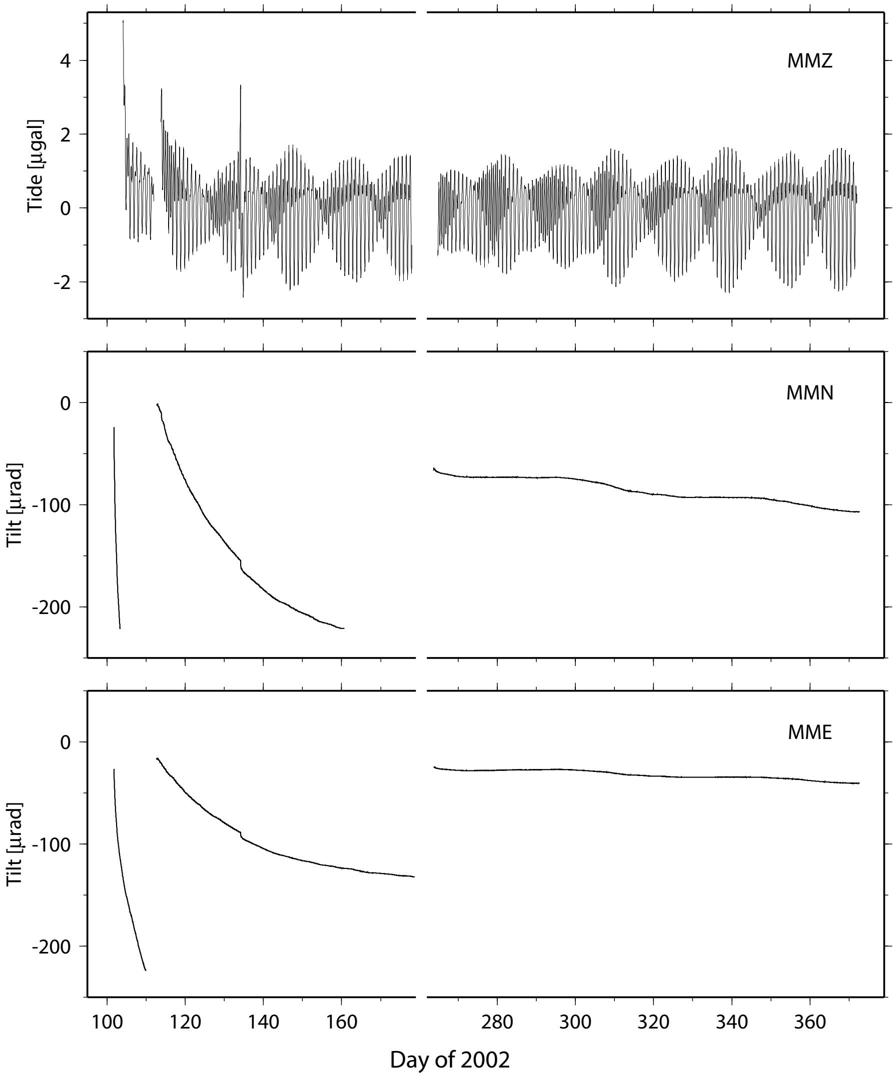

Figure 6.5: Mass position data, for portions of the time period 04/11/2002-01/07/2003, showing the progressive settling of the seismometers. At periods longer than the free period of the seismic sensor, the mass position is proportional to tilt on the horizontal components, and to perturbations in gravity on the vertical component. The mass position has therefore been converted to acceleration (vertical component, MMZ) and tilt (horizontal components, MMN, MME). The large steps on the horizontal components are associated with: 1) installation (day 100), and 2) re-centering (day 112, day 263). There is a smaller step on day 134, associated with a local $M_w4.95$ earthquake. The vertical component data have been detrended by subtracting a running 36 hour average (+/-18 hours) from each 1/2 hour duration smoothed data sample, to bring out the clearly visible tide signal.

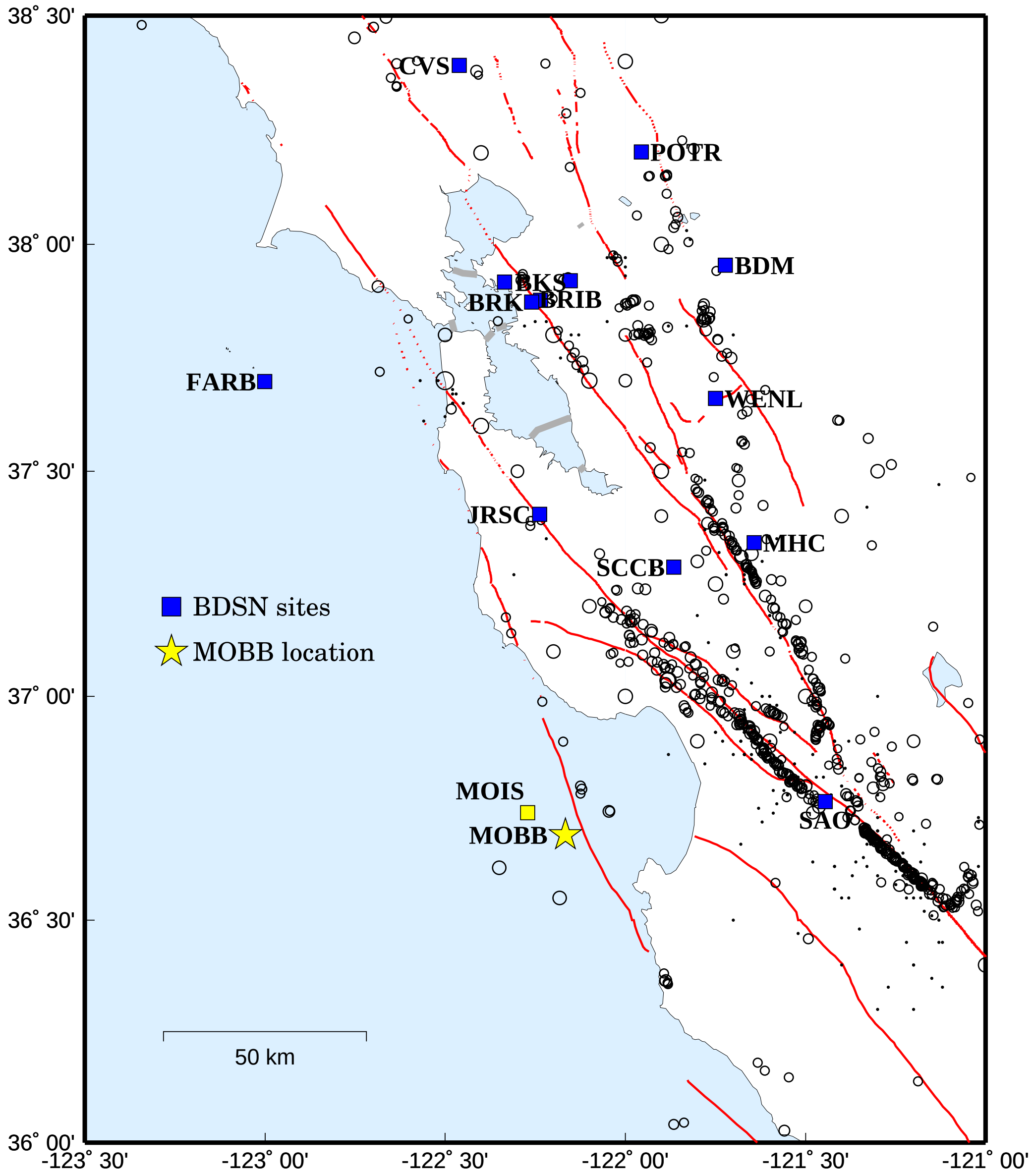

Figure 6.6: Location of MOBB (and MOIS) with respect to nearby broadband stations of the Berkeley Digital Seismic Network (BDSN). FARB is located on the Farallon Islands. MOBB is located just west of the San Gregorio fault.

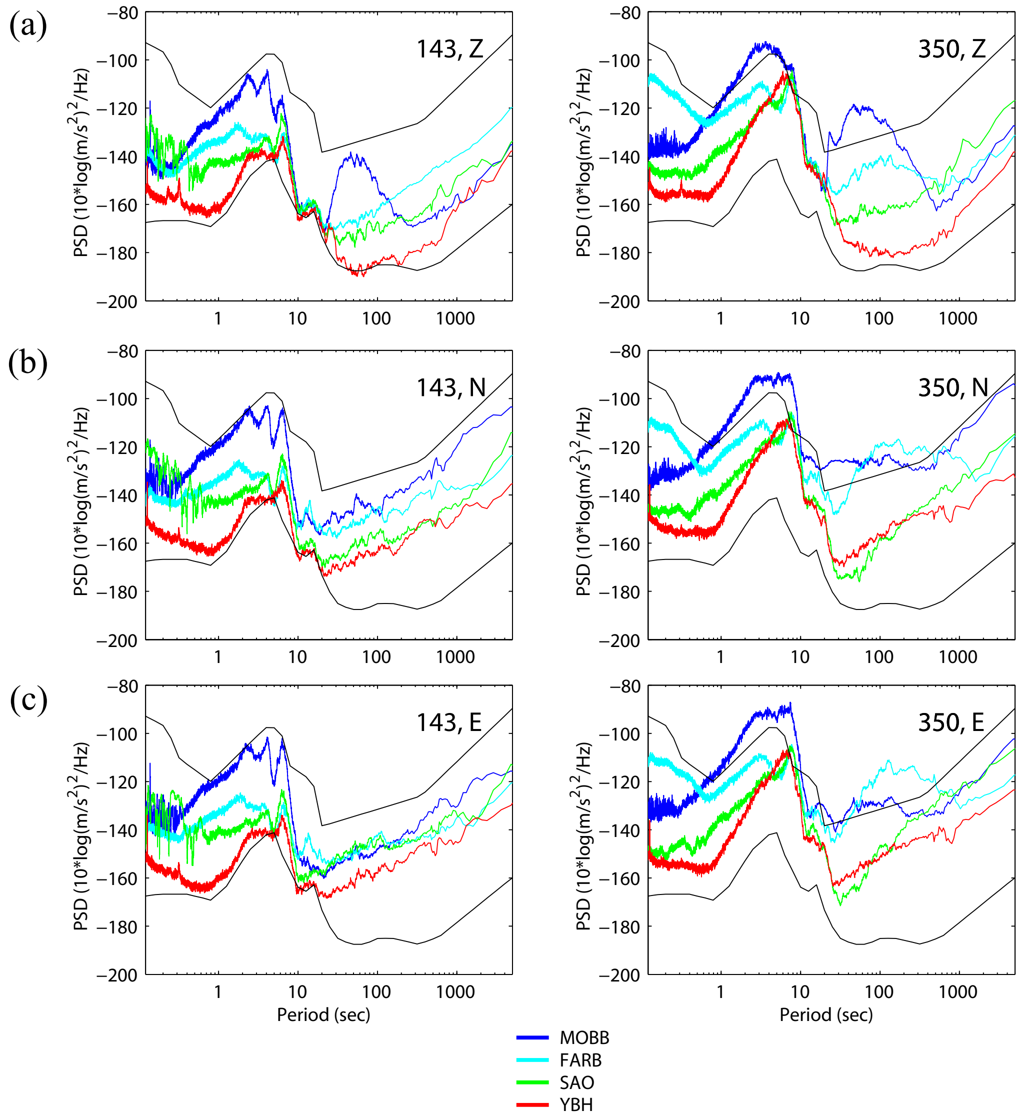

Figure 6.7: Comparison of noise recorded at MOBB and 3 other stations of the BDSN network, on two days in 2002 when no significant earthquake signals were recorded: a "quiet" day (143), and a "stormy" day (350), as assessed by the mean wave height recordings at a nearby NOAA buoy, located in Monterey Bay. The USGS high- and low-noise models for land stations are shown in black. Increased noise level for periods between 20 and 500 sec, due to ocean currents and infragravity waves, is observed at MOBB, as well as at the island station FARB. The noise level at MOBB between 10 and 20 sec is comparable to the land station YBH, one of the quietest stations of the BDSN. See Figure 6.6 for FARB and SAO locations. Station YBH is 560 km north of MOBB. (a) Vertical component; (b) North component; (c) East component.

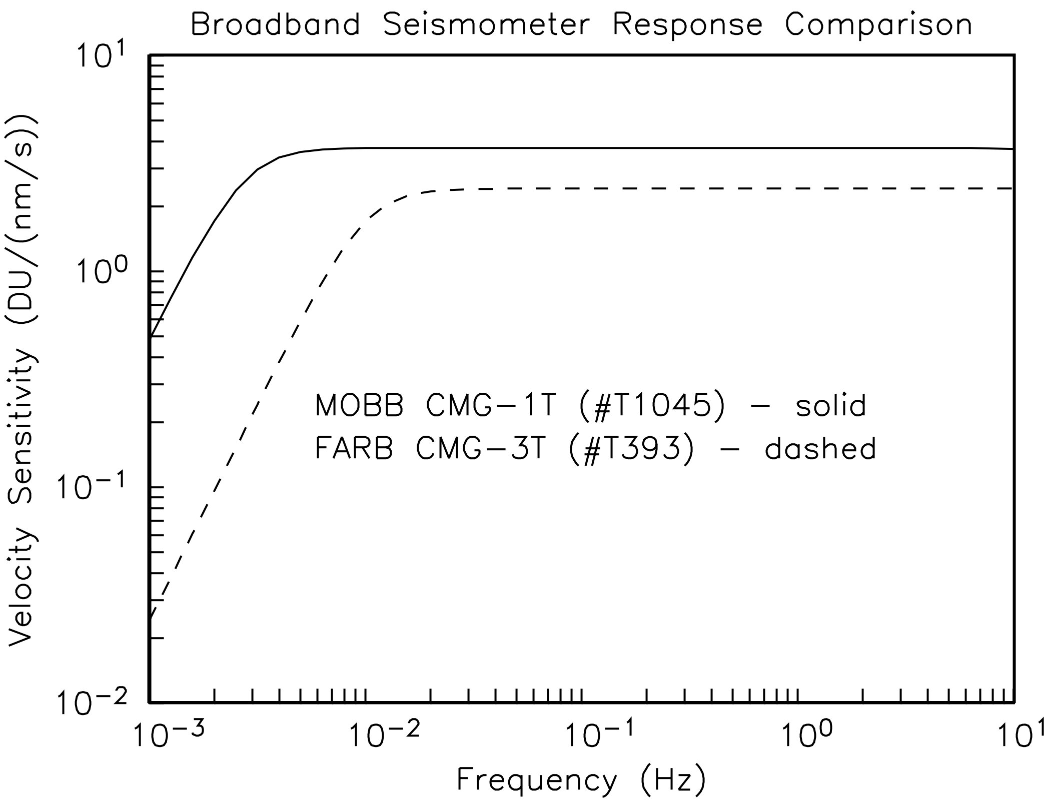

Figure 6.8: Comparison of instrument responses of the CMG-1T at MOBB and the CMG-3T at FARB.

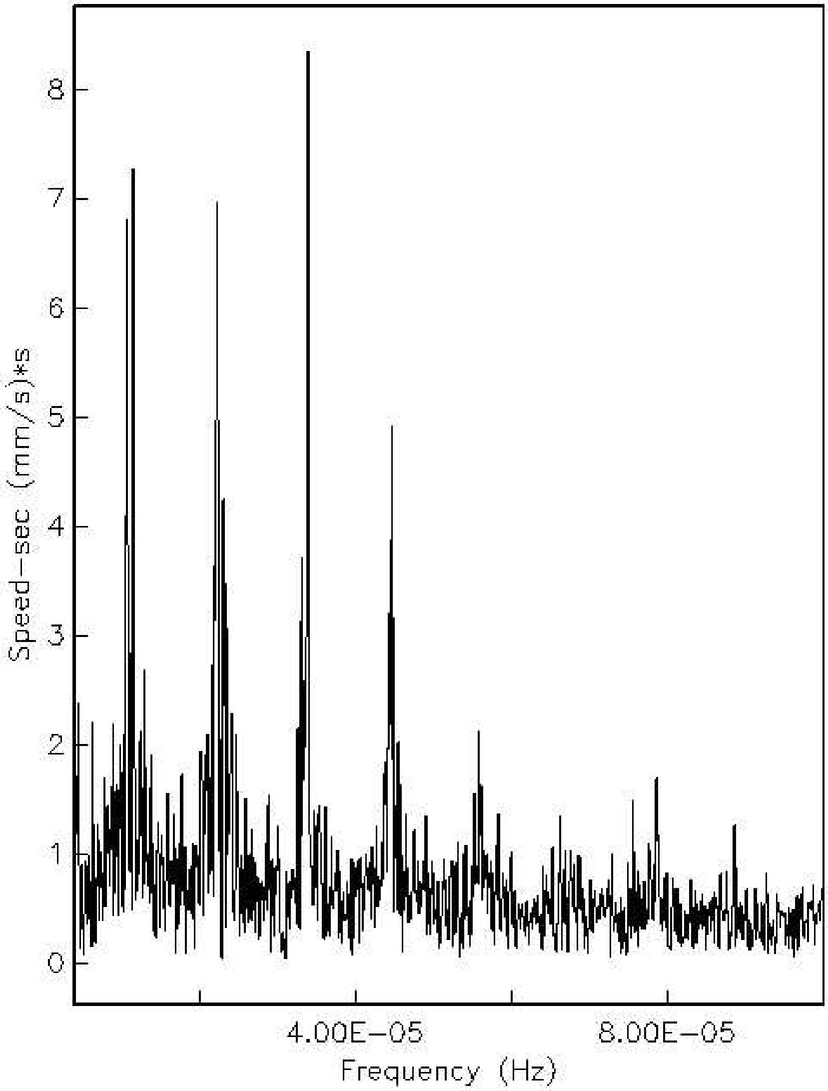

Figure 6.9: Spectrum of current speed (units are (mm/s)/Hz) based on a 78-day period of current meter data. The four dominant group of peaks coincide precisely with the frequencies of the diurnal, semi-diurnal, 8-hour and 6-hour components of the gravitational tides.

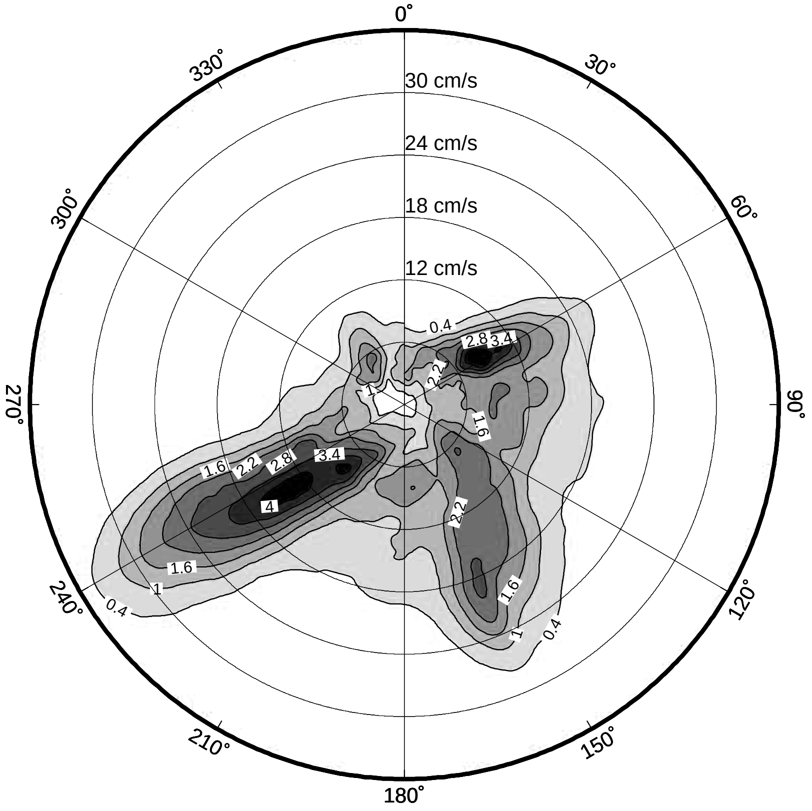

Figure 6.10: Distribution of current velocity data as a function of azimuth for the 78-day period shown in Figure 6.9. The contour label units are fractions of the average density distribution of the current velocity. The two dominant maxima (centered at 60^o and 240^o, i.e. orthogonal to the continental shelf) are associated with the semi-diurnal tidal currents. The third directional peak is roughly parallel to the coastline and appears to be related to the dominant ocean circulation.

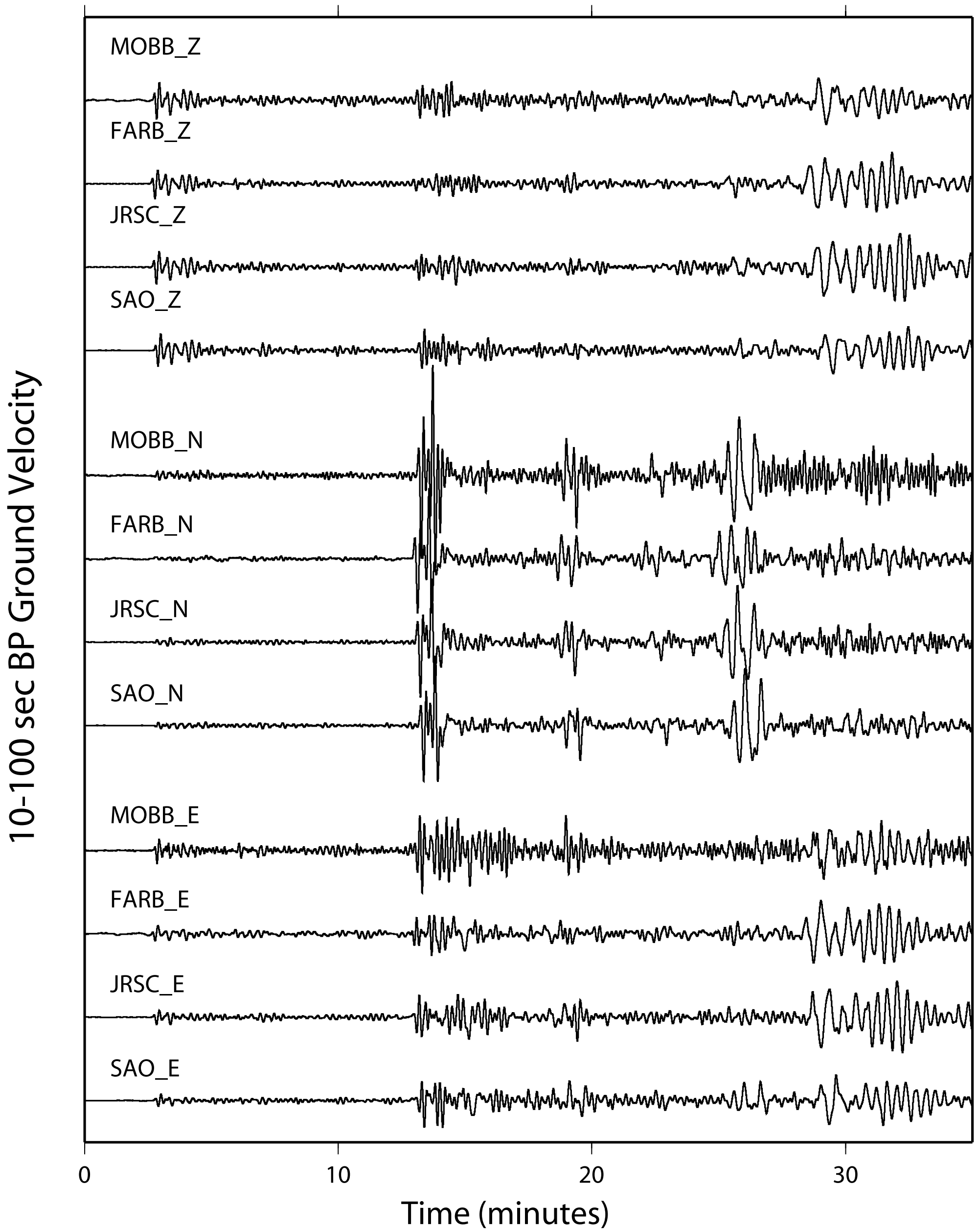

Figure 6.11: Comparison of vertical, N and E component records of the 04/26/2002 M_w7.1 Mariana earthquake (depth 86 km, distance 85.2^o, azimuth 283^o from MOBB), at MOBB and 3 stations of the BDSN. The records have been band-pass filtered between 10-100 sec.

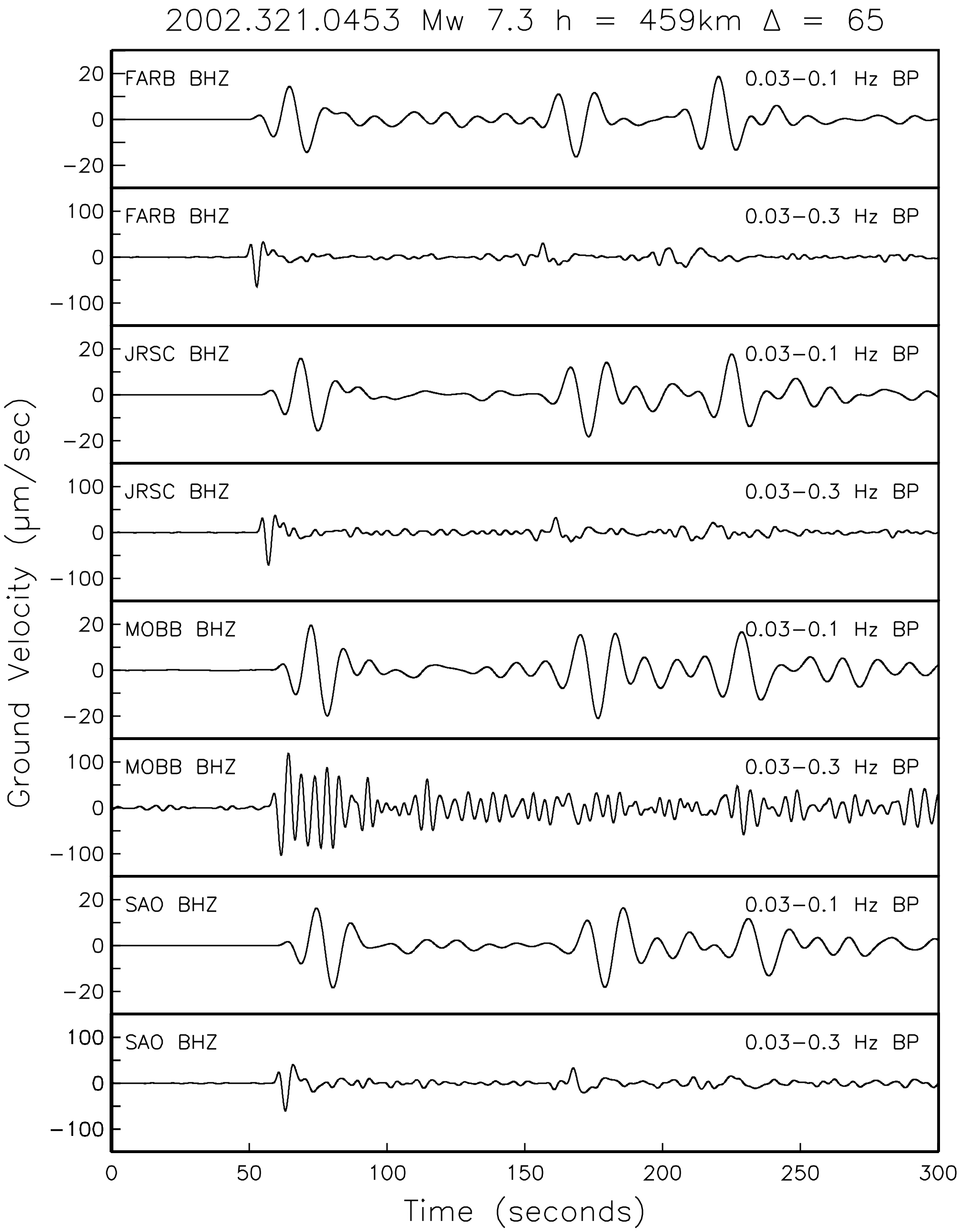

Figure 6.12: Comparison of vertical component records at stations FARB, JRSC, MOBB and SAO for the deep Kurile Island earthquake of 11/17/2002 (M_w7.3; depth 459 km; distance to MOBB 65^o). The data are shown in two pass-bands: 0.03-0.1 Hz and 0.03-0.3 Hz to emphasize the narrow-band character of the ringing in the MOBB P-wave data. Clearly visible in the lower frequency band are the P, pP and sP arrivals.

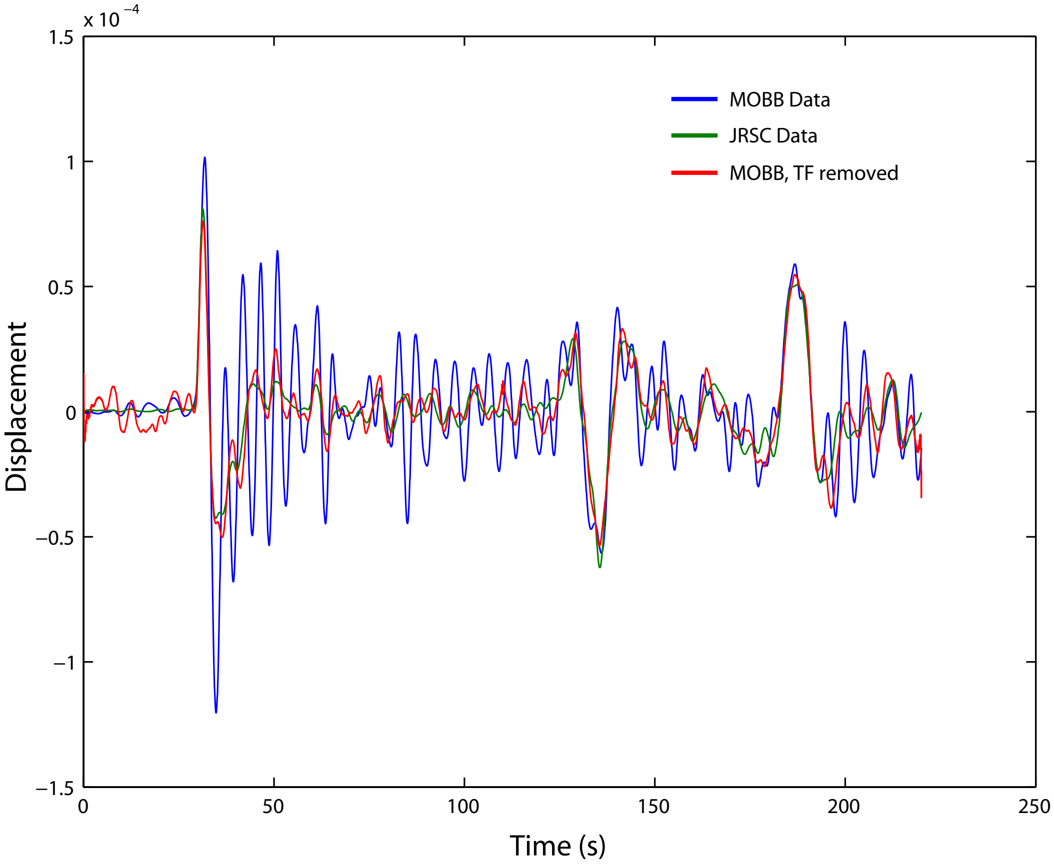

Figure 6.13: Raw vertical component data (P wave and depth phases) observed on the vertical component at stations MOBB (blue) and JRSC (green) for the 11/17/2002 deep Kurile Island earthquake. Clearly seen is the ringing due to the soft sediment layer in Monterey Bay. The red trace shows the MOBB data after removal of the transfer function constructed using JRSC data.

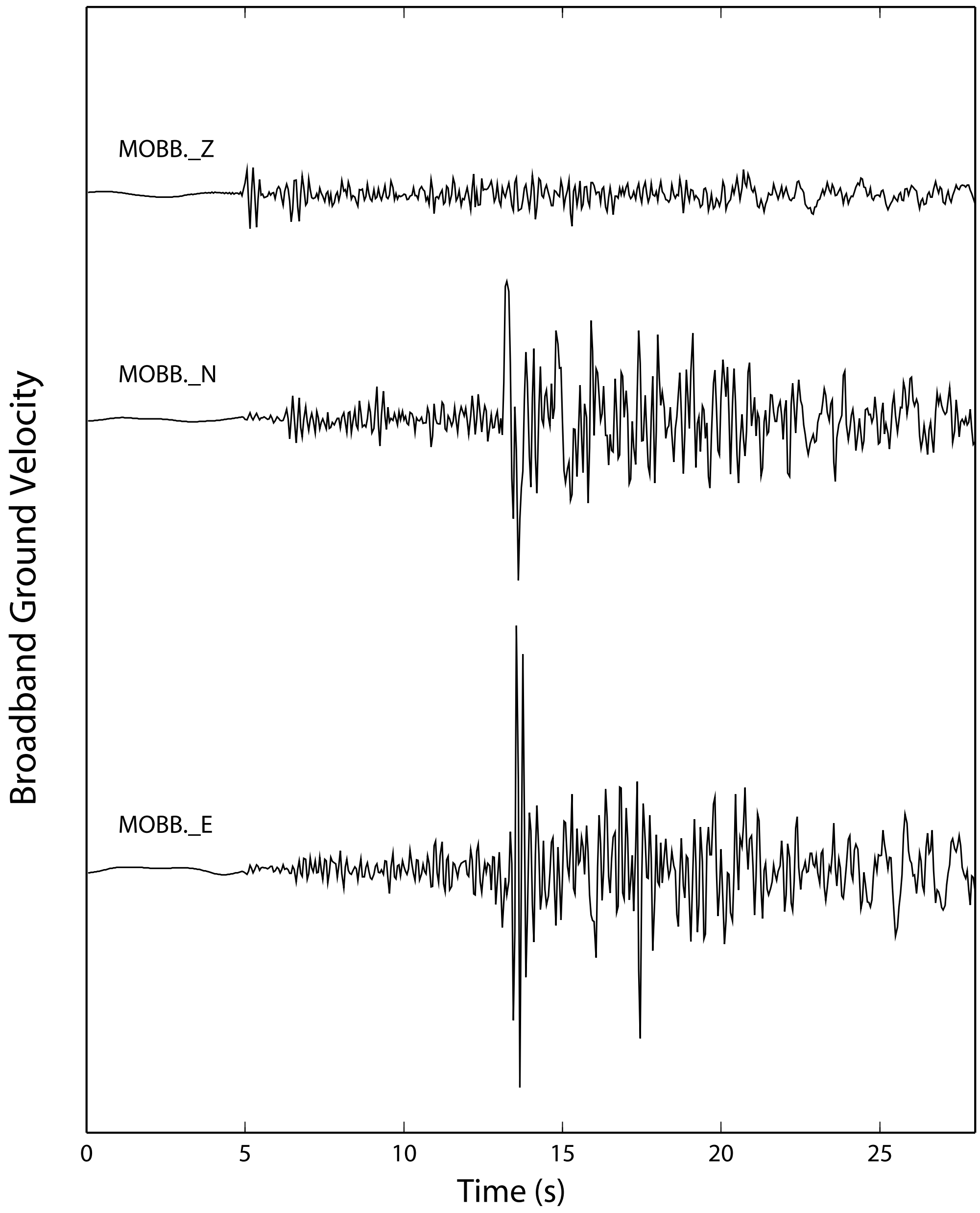

Figure 6.14: Deconvolved ground velocity records at MOBB of the 04/23/2002 M_w3.63 San Andreas fault event (lat. 36.866, lon. -121.61, depth 9 km).

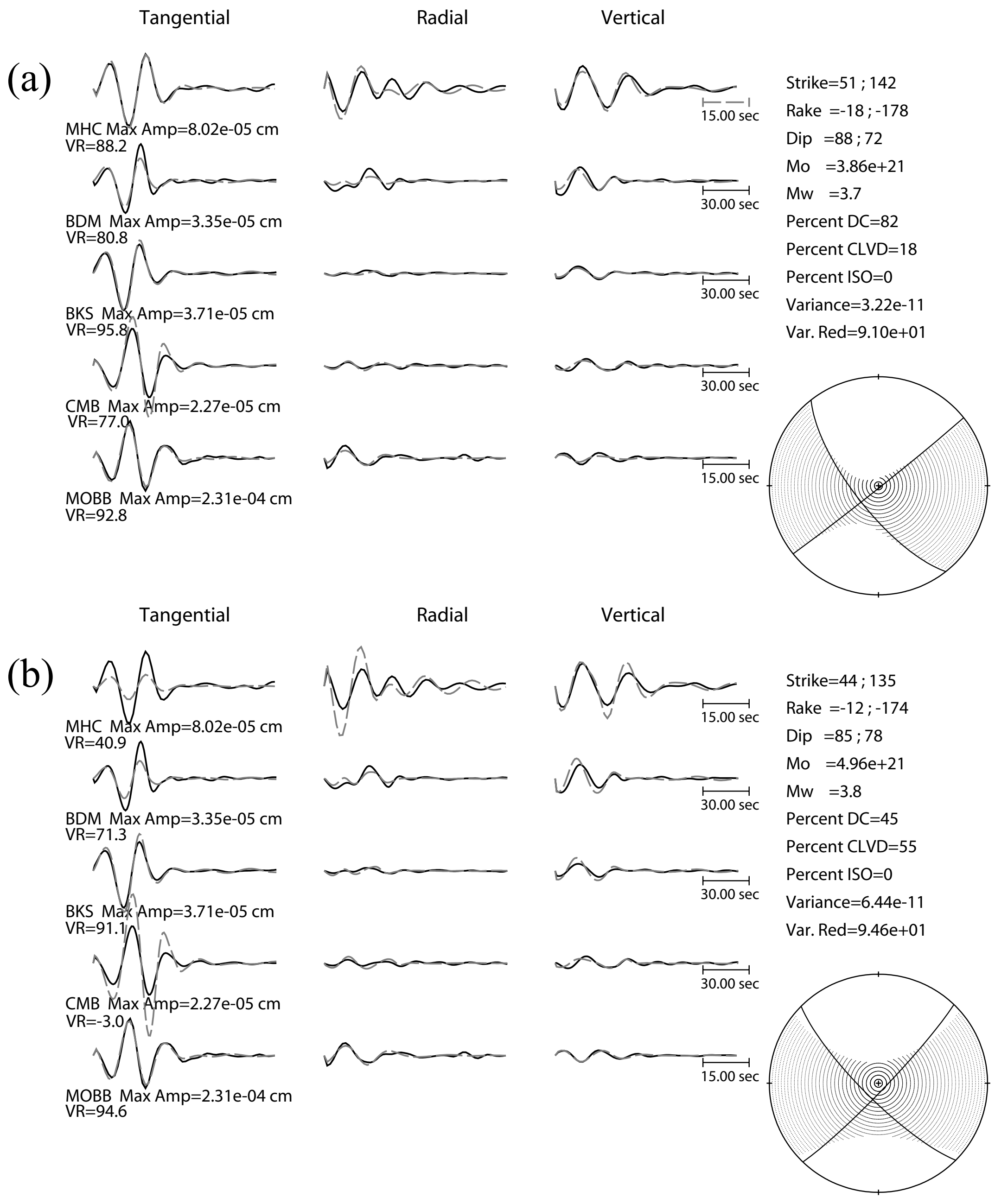

Figure 6.15: Results of moment tensor inversions for the $M_w 3.63$ regional event shown in Figure 6.14. (a) Inversion using 4 stations of the BDSN and MOBB (BDM, BKS, and CMB are bandpass filtered between 0.02 and 0.05 Hz; MHC and MOBB between 0.05 and 0.10 Hz). (b) Results of inversion using only MOBB, showing the good fits of the single station solution to the other BDSN waveform data.

Chapter 7

Observations of infragravity waves at the Monterey ocean bottom broadband station (MOBB)

This chapter was published in *Geochemistry Geophysics Geosystems* [*Dolenc et al.*, 2005b] with the title 'Observations of infragravity waves at the Monterey ocean bottom broadband station (MOBB)'.

Summary

Infragravity waves can be observed at the 1000 m deep ocean bottom broadband seismic station MOBB on stormy as well as quiet days. When compared to the energy of the short-period ocean waves recorded at the local buoys, infragravity waves in the longer than 20 s period band are found to be mainly locally generated from shorter-

period waves. Two types of modulation of the infragravity signal are observed. First, the entire infragravity band signal is modulated in-phase with tides, possibly as a result of the nonlinear exchange of energy between the short-period waves and tidal currents. Second, a longer-period modulation of the infragravity signal is observed and is best correlated with the energy of the 14 s period ocean waves. This correlation indicates that the mechanism of generation of double frequency microseisms and infragravity waves are likely strongly related. Previously recorded data during the Oregon ULF/VLF experiment at 600 m water depth also indicate that infragravity waves are primarily locally generated.

7.1 Introduction

The Monterey ocean bottom broadband station (MOBB) is a collaborative effort between the Monterey Bay Aquarium Research Institute (MBARI) and the Berkeley Seismological Laboratory (BSL). The MOBB was installed in April 2002, 40 km offshore in the Monterey Bay, at a water depth of 1000 m [*McGill et al.*, 2002; *Uhrhammer et al.*, 2002; *Romanowicz et al.*, 2003, 2006]. It is located west of the San Gregorio Fault, one of the major, yet not well documented faults of the San Andreas Fault System (Figure 7.1). The region is characterized by a very diverse topography; a wide, gently sloping continental shelf is found to the north, 1500 m deep Monterey Canyon is just south of MOBB, and a narrow shelf is present in Monterey Bay and further to the south. The MOBB is a continuously operated broadband seismic station and is considered the first step toward extending the Berkeley Digital Seismic Network (BDSN) westward of the Pacific-North America plate boundary. It follows from the experience gained previously during the 3-monthlong MOISE deployment in 1997, which was located about 10 km to the west [*Romanowicz et al.*, 1998; *Stutzmann et al.*, 2001].

The MOBB comprises a 3-component Guralp CMG-1T broadband seismometer buried in the ocean floor, a recording and battery package, as well as a collocated differential pressure gauge (DPG) [*Cox et al.*, 1984] and current meter, which measures ocean bottom current speed and direction [*Romanowicz et al.*, 2006]. At present, the station is autonomous and the data are on average retrieved every three months using the MBARI's remotely operated vehicle *Ventana*. With a planned connection to the MARS (Monterey Accelerated Research System; http://www.mbari.org/mars) fiber-optic cable, the data will be retrieved continuously and in real-time and will be publicly available from the Northern California Earthquake Data Center (NCEDC; http://quake.geo.berkeley.edu/ncedc).

The MOBB as well as future BDSN ocean bottom stations will enable us to better determine locations and mechanisms of offshore earthquakes, to learn more about the crustal structure at the continental edge, as well as to better understand the plate-boundary processes and therefore better constrain the seismic hazard along the west coast of northern California. At the same time such permanent ocean bottom stations equipped with broadband seismometers will provide us new information on the coupling between the ocean and the solid earth.

The broadband seismometer installed at MOBB is sensitive over a wide frequency range, from 50 Hz to 2.8 mHz (360 s). This enabled us to also observe the long-period signal which is largely due to the ocean surface infragravity waves.

7.2 Infragravity waves

Infragravity waves are ocean surface waves with periods longer than the wind-driven waves and the swell. Their wave amplitudes in the deep water are small (< 1 cm) and they can be observed in the frequency band from 0.002 to 0.05 Hz. They were first observed near the shore by *Munk* [1949] and *Tucker* [1950]. The pressure fluctuations from infragravity waves at the deep seafloor were first measured by *Sutton et al.* [1965], and they were first observed at the sea surface in the open ocean by *Snodgrass et al.* [1966]. Although high correlations have been observed between infragravity and shorter-period ocean waves (wind waves and swell) energy [e.g., *Munk*, 1949; *Tucker*, 1950; *Elgar et al.*, 1992; *Herbers et al.*, 1995a], the precise generation mechanism for infragravity waves is still not completely understood.

In oceanography, infragravity waves are considered important for harbor oscillations and nearshore processes, such as sediment transport. In seismology, pressure fluctuations due to infragravity waves have been identified as an important source of long-period noise at the ocean bottom [*Webb et al.*, 1991; *Webb*, 1998]. Infragravity waves have recently also been proposed as a source of the Earth's continuous free oscillations [*Rhie & Romanowicz*, 2004; *Tanimoto*, 2005].

7.3 Power spectral density

We first compared the power spectral density (PSD) at MOBB and three other stations of the BDSN network (Figure 7.2). Station SAO is the closest land station (see Figure 7.1), and station YBH is one of the quietest BDSN stations, located 560 km north of MOBB. Results obtained for a quiet day (2002, day 143) and for a stormy day (2002, day 350) are shown for the vertical (top) and for one horizontal component (E-W, bottom). Four hours of data (00-04 UTC) were used in the calculation. The quiet and the stormy day were selected based on the spectral wave density (SWD) measured at the nearby NOAA buoy 46042. There were no significant earthquakes recorded during the two time periods.

The MOBB vertical component data on a quiet day show a noise "hump" for periods between 20 and 200 s that is not present in the land station data. The observed peak at MOBB is even stronger and wider (periods 20-500 s) on a stormy day, when it can also be observed at the Farallon Islands station FARB. On the other hand, the noise at MOBB between 10 and 20 s is comparable to the quietest BDSN land stations. The results also show that the noise observed at MOBB on a quiet day for periods longer than 20 s is comparable to the noise observed at the island station on a stormy day. The sharp short-period cutoff observed at 20 s in the spectrum for the vertical MOBB component on a stormy day is determined by the water depth, since only linear waves with wave numbers comparable or smaller than the inverse of the water depth can generate a detectable pressure signal at the seafloor [*Webb*, 1998]. In the infragravity wave band, the difference between quiet and stormy period is larger at the lower frequencies than at the high-frequency end, with more low-frequency energy during storms.

In the microseism band, the three peaks are evident between 1 and 10 s. They are often observed in the spectra from the sites in the Pacific and are associated with the large storms in the Southern Ocean for the low-frequency peak, with the local storms in the North Pacific for the main peak, and with the local wind wave field for the high frequency peak [*Webb*, 1992; *Webb*, 1998]. On a stormy day, a well pronounced peak is present in the infragravity wave band between 20 and 30 s. A few more subtle peaks seem to be also present at longer periods within the infragravity wave band.

The results for the two horizontal components were similar and therefore only one component (E-W) is shown in Figure 7.2. In this case there is no peak observed at MOBB for periods longer than 20 s on a quiet day. On the stormy day, the increased noise at MOBB is present again. The signal at the island station FARB is even stronger than at MOBB and it extends all the way to 1000 s.

The shape of the noise spectra in the infragravity wave band measured at MOBB is in agreement with observations from previous deployments in which seismometers were buried under the ocean floor [*Stephen et al.*, 2003; *Araki et al.*, 2004], as well as with theoretical predictions [*Araki et al.*, 2004].

7.4 Generation of infragravity waves

We computed PSD for 1-hour long segments for all the available MOBB data until July 2004 and compared the results to the SWD measured at the nearby NOAA buoys. The SWD is computed at the buoys once every hour and it measures energy of the ocean waves in m^2/Hz in the 0.01 Hz wide frequency bins that cover the 0.03 to 0.4 Hz range. The location of the buoys considered is shown in Figure 7.3. Comparison spectrograms for a 7-day period (12/9-16/2003) are presented in Figure 7.4. The infragravity peak can be observed in the PSD plot for the vertical MOBB channel throughout the 7-day period (Figure 7.4, top panel). A rather sudden change of the infragravity peak width is indicated with a black line. The second panel from top in Figure 7.4 shows the SWD measured at the western most buoy 46059, and the panels below the SWD at three other nearshore buoys ordered by longitude. The storm observed on day 344 was approaching from the WNW direction, as the mean wave direction corresponding to energy of the dominant period measured at buoy 46042 in the second half of day 344 ranged from 280° to 295° from North. Increased energy of the 10-20 s ocean waves on day 344 can therefore first be seen on buoy 46059, and last on buoy 46011. The arrival of these waves at buoy 46042 coincides with the increase of the infragravity signal on MOBB. Buoy 46042 is the closest one to MOBB, located only 23 km to the W (see Figure 7.1). The fact that the arrival of the ocean waves coincides with increase of the infragravity signal clearly tells us that the infragravity waves observed at MOBB during this time period are primarily locally generated. The same can generally be observed throughout the deployment and for storms arriving from different azimuths.

The narrow peaks observed between 10 and 40 s in the second half of day 343 and early on day 344 correspond to an M_w6.2 Andreanof Islands (Aleutian Islands) earthquake and to an M_w6.8 earthquake in Taiwan. We also see a dispersed swell arrival with 18-26 s periods between days 345 and 347. We followed the approach described in *Bromirski and Duennebier* [2002] and inverted the dispersion trend to obtain the origin time and distance to the swell source. We assumed a mean water depth of 4500 m along the swell propagation path and obtained a distance of 4800 km and for the origin time, 01 UTC on day 343. By comparing the SWD from the buoys in the Pacific Ocean around the calculated origin time, we matched the swell source to a strong storm observed at the buoy 46072, located in the central Aleutians, 4233 km from MOBB. Similar dispersed swell arrivals can often be observed at MOBB and most of the time their origin can be traced to the northern or northeastern Pacific Ocean.

7.5 Modulation of infragravity signal

The PSD for the vertical MOBB component for a 10-day period (01/17-27/2004) is shown in Figure 7.5b. As before, the strongest infragravity signal (days 18-20) coincides with the increased energy of 10-20 s ocean waves as recorded at the local buoy 46042 (Figure 7.5f), although the arrival of the storm is not as sharp as in the previous example. In addition, two types of modulation of the infragravity peak can be observed.

The modulation with a period equal to the diurnal tide and to a lesser extent the semidiurnal tide is best seen at the short-period end of the infragravity peak (30-40 s periods) as well as throughout the entire infragravity band. It can be observed for the entire 10-day period. In fact, modulation as described below is observed throughout the deployment. This modulation clearly correlates with the amplitude of the tides at MOBB, shown in Figure 7.5a. Comparison of the PSD and the tides shows that the infragravity waves have less energy at low tides. This can best be seen for the strongest minima in tides that occur close to the beginning of each day for this time period. Additional small modulation can also be seen, particularly at the short-period end of the infragravity peak. It coincides with the second strongest tides minima which occur close to the middle of the day for this time period.

Also observed is a low-frequency modulation which is best seen as the variation of the period on the long-period side of the infragravity peak at which the infragravity peak rises above the noise from other sources (Figures 7.5b and 7.5c). The envelope of the observed infragravity peak on the long-period side was taken at the PSD value of -136 dB. The infragravity peak extends to longest periods during days 18 and 19, and then again slightly increases between days 22 and 26. First we compare this to the significant wave height measured at the local buoy 46042 (Figure 7.5d). Significant wave height is the average of the highest 1/3 of all of the wave heights during the 20-minute sampling period, calculated once every hour. The two agree well in the first half of the 10-day period, but then significant wave height has a peak in the second half of the day 25. Comparison with the SWD plot (Figure 7.5f) reveals that at that time most of the wave energy was in the waves with periods shorter than 10 s. We therefore looked at the correlation between the period of the infragravity peak envelope and the wave energy in individual frequency bins as observed at the local buoy. The best correlation was observed with the ocean waves with 14.3 s period for which the SWD is shown in Figure 7.5e and Figure 7.6b. Correlations between the period of the infragravity peak envelope and SWD of the ocean waves at two other periods (12.5 s and 16.6 s) as well as the significant wave height are also shown in Figure 7.6. The correlation coefficient between the period of the infragravity peak envelope and the SWD observed in the individual bins at buoy 46042, as a function of the SWD bin period, is presented in Figure 7.6d, and confirms that the infragravity peak long-period modulation correlates the strongest with the ocean wave energy at ~14 s.

7.6 Observation of infragravity signal during the Oregon ULF/VLF experiment

We have performed a similar analysis with the seismic and buoy data recorded during the Oregon ULF/VLF temporary deployment in 1991 [*Bromirski & Duennebier*, 1995; *Bromirski & Duennebier*, 2002]. In this experiment the seismic data were recorded at the 3-component Guralp CMG-3 broadband seismometer, sensitive from 50 Hz to 0.01 Hz (100 s), that was buried in the ocean floor, about 48 km off the Oregon coast (Figure 7.7). The water depth at this location was about 600 m. The locations of the two closest NOAA buoys that had spectral wave density data available for the time period of the experiment are shown in Figure 7.7. The closer buoy 46040 was located 68 km SSE of the seismometer location, at the water depth of 112 m, and about 20 km from the coast. The deepwater buoy 46005 was located 493 km W of the seismometer location.

In Figure 7.8, the PSD at the Oregon ULF station for a 4-hour period on a quiet day (1999, day 200, 07-11 UTC) is compared to the PSD on a stormy day (1999, day 205, 06-10 UTC). There were no significant earthquakes recorded during the two time periods. The results obtained for the vertical component show that the infragravity peak can be observed in the PSD during both quiet and stormy periods. The vertical component data on a quiet day show a noise "hump" for periods between 16 and 115 seconds. The observed peak is stronger on a stormy day. Since the noise level around the infragravity peak is also much higher on a stormy day, the short- and long-period ends of the infragravity peak are hidden and can not be directly compared to the ones observed on a quiet day. At Oregon ULF, the infragravity "hump" cannot be observed on either of the two horizontal components, although results for only one are shown in Figure 7.8. This indicates that for the horizontal components, noise sources other than infragravity waves are dominant at periods longer than 10 s. Part of this noise is probably generated by slight movements of the buried seismic package [*Bromirski & Duennebier*, 1995].

When compared to the result obtained with the MOBB data, the short-period end of the infragravity peak observed for the vertical component data extends to shorter periods. This is expected as the Oregon ULF station was located at only 600 m water depth. The pressure signal at the seafloor of depth H is related to the surface wave height ζ by

$$P_{bottom} = \rho g \zeta / \cosh(kH) \approx P_{surface} e^{-kH}, \tag{7.1}$$

where k is the wave number and ρ is water density. Assuming that the pressure fluctuations are caused by freely traveling surface gravity waves the dispersion relation can be used to determine the wave number

$$\omega^2 = gk \ \tanh(kH), \tag{7.2}$$

where ω is angular frequency of the ocean gravity wave. For water depth at MOBB H=1000 m and $\omega = 2\pi/20s$, which corresponds to the observed short-period cutoff period at MOBB, we obtain the value for the product of the wave number and water depth kH=10.1. Using equation (7.2) for water depth H=600 m and kH=10.1 from the above MOBB example, we obtain the expected short-period cutoff period for the Oregon experiment to be 15.5 s. This agrees well with the observed short-period cutoff value of 16 s.

The seismic data from the Oregon experiment are noisier than the MOBB data presented above, but the infragravity signal can still easily be observed during the 7-day deployment period (7/19-26/1991; Figure 7.9a). The SWD recorded at the two buoys is shown in Figures 7.9d and 7.9e. The signal recorded at the local buoy 46040 is again better correlated with the seismic PSD. The increased infragravity signal observed between days 204 and 206 matches the arrival of the 10-20 s ocean waves as recorded on the local buoy 46040.

The low-frequency modulation of the infragravity peak can again be seen as the variation of the period on the long-period side of the infragravity peak at which the infragravity peak rises above the noise from other sources (Figures 7.9a and 7.9b). The envelope of the observed infragravity peak on the long-period side was taken at the PSD value of -136 dB. The hours that had increased noise throughout the 10-200 s period band were not used in the calculation. The correlation between the period of the infragravity peak envelope and the wave energy in individual frequency bins as observed at the local buoy 46040 is presented in Figure 7.10. The best correlation was observed with the ocean waves with 12.5 s period for which the SWD is shown in Figure 7.9c and Figure 7.10b. Correlations between the period of the infragravity peak envelope and SWD of the ocean waves at two other periods (11.1 s and 14.3 s) are shown in Figures 7.10a and 7.10c. The correlation coefficient between the period of the infragravity peak envelope and the SWD observed in the individual bins at buoy 46040, as a function of the SWD bin period, is presented in Figure 7.10d, and confirms that the infragravity peak long-period modulation correlates the strongest with the ocean wave energy at ~12.5 s.

7.7 Discussion

7.7.1 Tidal modulation of the infragravity signal

The fact that the observed modulated infragravity signal is weakest at low tides is just the opposite from what one would expect from hydrodynamic filtering. The term "hydrodynamic filtering" is often used to describe that the pressure signal from the ocean waves decays exponentially with water depth, depending on the wave number of the waves [*Kinsman*, 1984]. Since only linear waves with wave numbers comparable or smaller than the inverse of the water depth can generate detectable pressure fluctuations at the seafloor, one would expect that the higher water column above MOBB at high tides would shield it against pressure signal from the higher frequency infragravity waves, which would result in weaker signal. What we observe is just the opposite which indicates that the tides must play an important role in the generation of the infragravity waves rather than just weakening the pressure signal at the ocean bottom. Also, the effect of the hydrodynamic filtering due to only a few meters high tides in a 1000 m water depth is very small. Using the equation (7.1), the relative change in the pressure variation at the bottom due to 3 m water depth variation can be estimated to be only about 6% for k=0.01/m (λ=324 m). In addition, such changes in hydrodynamic filtering should have stronger effect on the shorter-period infragravity waves. Our observations, on the other hand, show that strong modulation can be observed throughout the entire infragravity band.

Previous studies of the nonlinear interaction between short-period waves and currents [*Longuet-Higgins & Stewart*, 1960, 1961, 1964] found that the energy variations of the short-period waves correspond to work done by the currents against the radiation stress of the short-period waves. The magnitude of the energy exchange between the short-period waves and tidal current depends on the pattern of the tidal currents, but in simple situations, the energy of the short-period waves is in phase with the tidal elevations [*Longuet-Higgins & Stewart*, 1964]. This agrees with our observations. At the moment, currents are not measured at the nearby NOAA buoys, but the currents observed at the ocean bottom at MOBB clearly show the tidal pattern [*Romanowicz et al.*, 2006, Figure 9; *Uhrhammer et al.*, 2003]. Since the current direction and speed at shallow water depths as well as direction and amplitude of the incoming short-period waves all influence the efficiency of the energy exchange during nonlinear interaction between short-period waves and currents, future modeling of the observations at MOBB will help us better understand the underlying processes. For this purpose a better knowledge of the surface currents is needed.

Another effect that the tides have on the generation of the infragravity waves is through different topography that is brought into play at the same water depth during different tide heights. A study by *Herbers et al.* [1995b] observed that the energy levels of the free infragravity waves on the shelf depend on the surrounding topography. They suggested that the shelf topography is important to the propagation and trapping of free infragravity motions and that generation and reflection of free infragravity waves is sensitive to the shoreline morphology. In our case the topography around MOBB is very complex (see Figure 7.1) and it is possible that already a small water depth change can significantly perturb the conditions for generation and reflection of infragravity waves. Our observations seem to agree with observations by *Herbers et al.* [1995b], as we record stronger infragravity signal at high tides, when the shelf is slightly wider. Since MOBB is located close to the edge of the shelf our results suggest that at high tides infragravity waves are more efficiently generated on the shelf and/or can more efficiently leak from the shelf into the deeper water. Previous studies that observed tidal modulation of the infragravity energy close to shore [e.g., *Guza & Thornton*, 1982; *Okihiro and Guza*, 1995] suggested that tidal modulation could result either from the changes of the beach face slope with the tides or the changes of the surf zone width.

7.7.2 Short-period (12-14 s) ocean wave energy modulation of the infragravity signal

The low-frequency modulation of the observed infragravity signal during a 10-day stormy period at MOBB is best correlated with the energy of the 14.3 s period ocean waves. A similar result can be obtained for other stormy periods at MOBB. Analysis of the data recorded during the Oregon ULF/VLF experiment shows best correlation with the energy of the slightly shorter, 12.5 s period ocean waves. The data from the Oregon experiment only span over a 7-day period in which the energy of the ocean waves was significantly lower than during the time period used for MOBB. Also, the sensor used in the Oregon experiment had a shorter long-period corner frequency. We believe that for a better understanding of the influence of the water depth and regional topography on the observed correlation between the period of the ocean waves and the low-frequency modulation of the infragravity peak, data from stations deployed simultaneously and in a relative proximity of each other, as well as equipped with seismometers sensitive to longer than 100 s periods, should be used. Nevertheless, the results from both deployments are telling us that the modulation of the short-period (12-14 s) ocean wave energy can be observed in the infragravity signal as well. This suggests that the short-period ocean waves are essential for the generation of the infragravity waves. It is interesting to note that the same period ocean waves are also the source of the microseisms noise, observed at the double frequency, at 6-7 s. This suggests that the generation mechanisms of infragravity waves and double frequency microseisms are closely related, and originate from the non-linear interaction of ~14 s ocean waves, as already well documented for the microseisms [e.g., *Longuet-Higgins*, 1950].

7.7.3 Future work

In addition to the results presented in this paper we have done a preliminary investigation of the data recorded at the station KEBB, located offshore Washington, at a water depth of 2376 m. Station KEBB is part of the NEPTUNE project whose goal is to establish a regional ocean observatory in the northeast Pacific Ocean. Preliminary results showed that infragravity waves observed at station KEBB were mainly generated close to the nearby coast. A number of buoys as well as additional ocean bottom broadband seismometers that are already installed in the region, but for which the data are not available yet, will be used to learn more about the directional properties of the observed infragravity waves. This will be the subject of our future study.

7.8 Conclusions

The primary reason for installing ocean bottom broadband seismic stations is to record earthquakes. Any other signal is often regarded as noise and additional processing is required to remove it (D. Dolenc et al., manuscript in preparation, 2006). At the same time observations of non-seismic signals, like infragravity waves, can help us learn more about their generation and propagation. Such observations can also enable us to better understand the coupling between the ocean and the solid earth and learn more about the earth structure using non-seismic sources.

Infragravity waves can be observed at the permanent ocean bottom broadband seismic station MOBB on stormy as well as quiet days. When compared to the energy of the short-period ocean waves recorded at the local buoys, infragravity waves in the longer than 20 s period band are found to be mainly locally generated from shorter period waves. Two types of modulation of the infragravity signal are observed. First, the entire infragravity band is modulated in-phase with tides. It is possible that this is a result of the nonlinear exchange of energy between the short-period waves and tidal currents. Second, the low-frequency modulation of the observed infragravity peak is best correlated with the energy of the 14.3 s period ocean waves, suggesting a close relation of infragravity wave generation to that of double frequency microseisms, which have maximum energy at 6-7 s. Analysis of the data recorded during the Oregon ULF/VLF experiment also indicates that infragravity waves are primarily locally generated. In this case, the low-frequency modulation of the observed infragravity peak is best correlated with the energy of the 12.5 s period ocean waves. To better understand the influence of the water depth and regional topography on the observed correlation between the low-frequency modulation of the infragravity peak and period of the ocean waves it would be important to use data from stations deployed simultaneously in a relative proximity of each other.

To better understand the coupling between the ocean and the solid earth it will be important to compare observations from different broadband ocean bottom stations and nearby buoys. Future experiments that will include a large array of ocean bottom broadband seismometers as well as data from a dense network of ocean buoys will help us learn more about the directional distribution of infragravity waves and their generation.

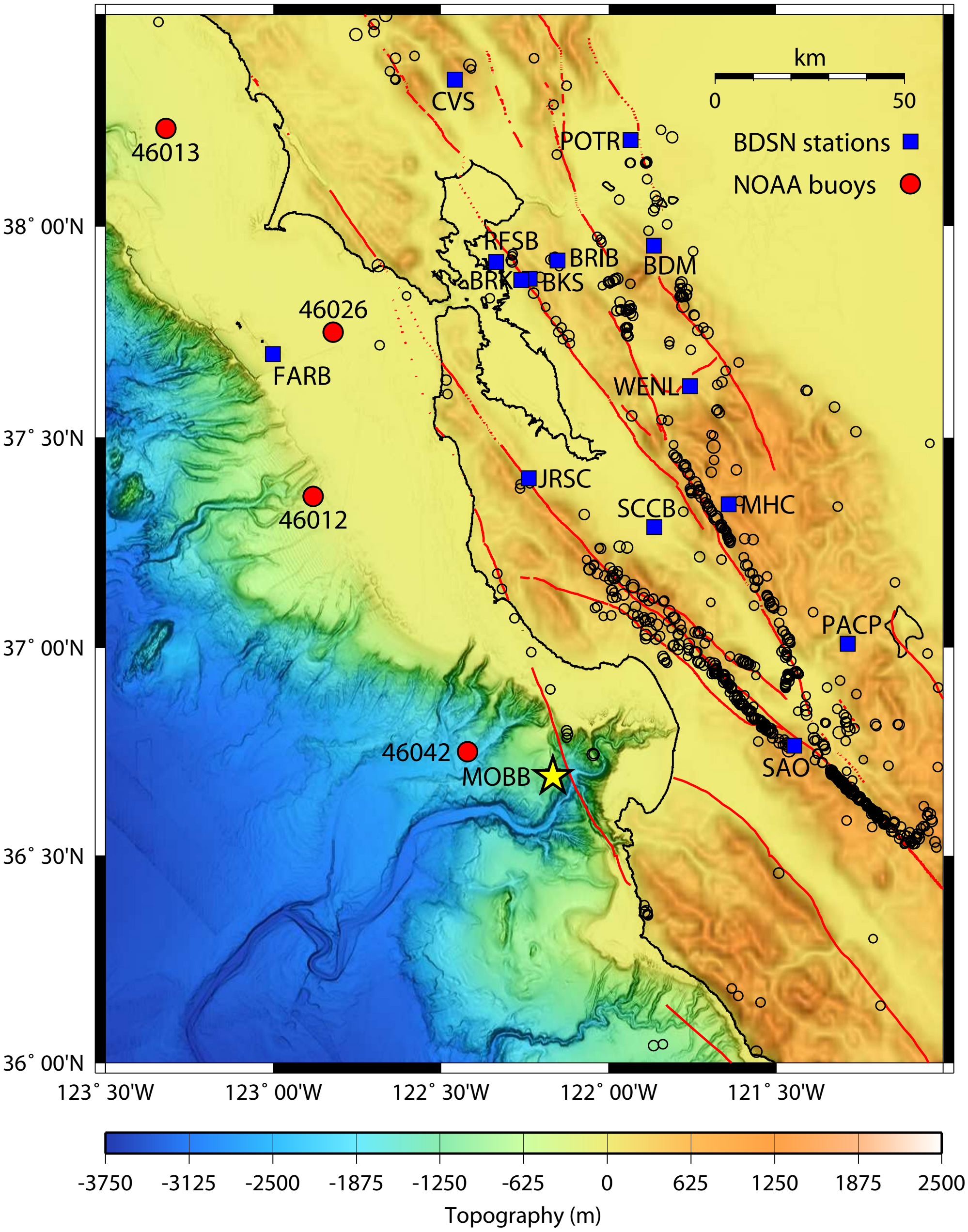

Figure 7.1: Locations of the MOBB (yellow) and the BDSN seismic stations (blue) shown against the seafloor and land topography. Background seismicity (ANSS catalog, 1968-2004, M3.5+) is shown in black. Locations of the NOAA buoys closest to the MOBB are shown in red. Fault lines from the California Division of Mines and Geology database are shown in red as well.

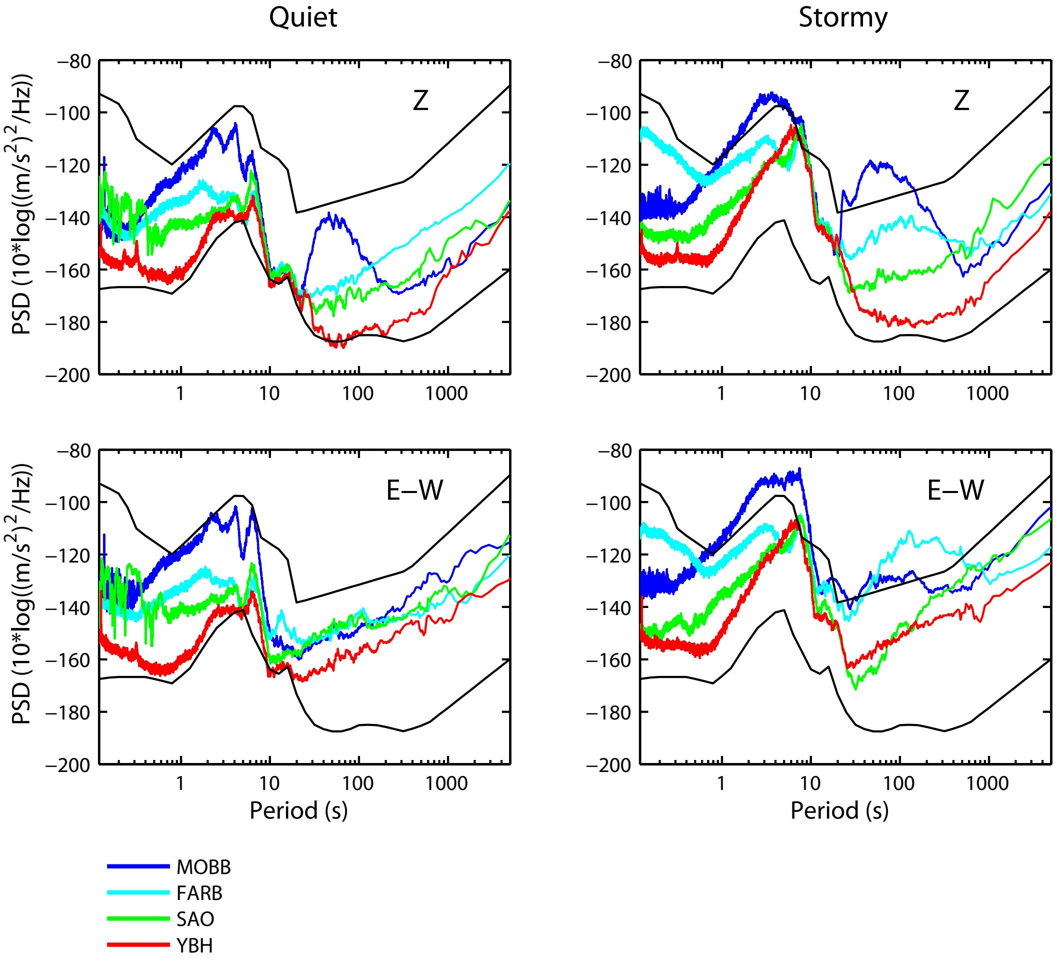

Figure 7.2: Comparison of the power spectral density (PSD) at the stations MOBB, FARB, SAO, and YBH calculated for a quiet day (2002, day 143) and for a stormy day (2002, day 350). Results obtained for the vertical (top) and for the horizontal components (E-W, bottom) are shown. The USGS high- and low-noise models for land stations are shown in black [*Peterson*, 1993].

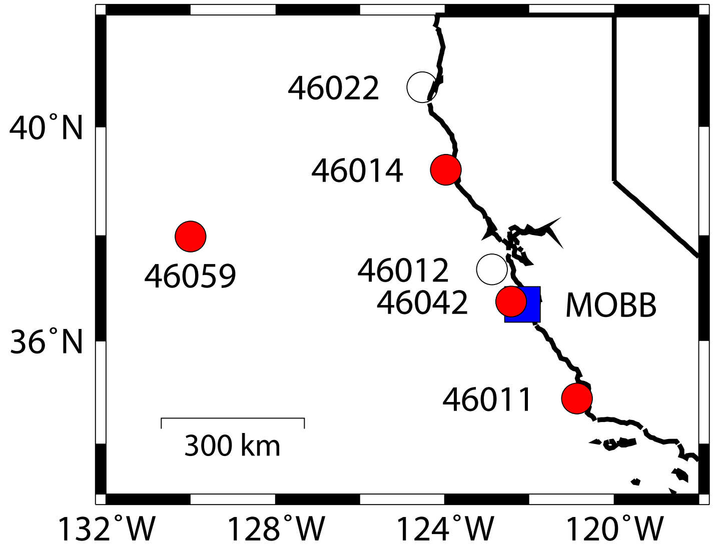

Figure 7.3: The location of some of the NOAA buoys closest to the MOBB. Red color indicates buoys with data available for the time period presented in Figure 7.4.

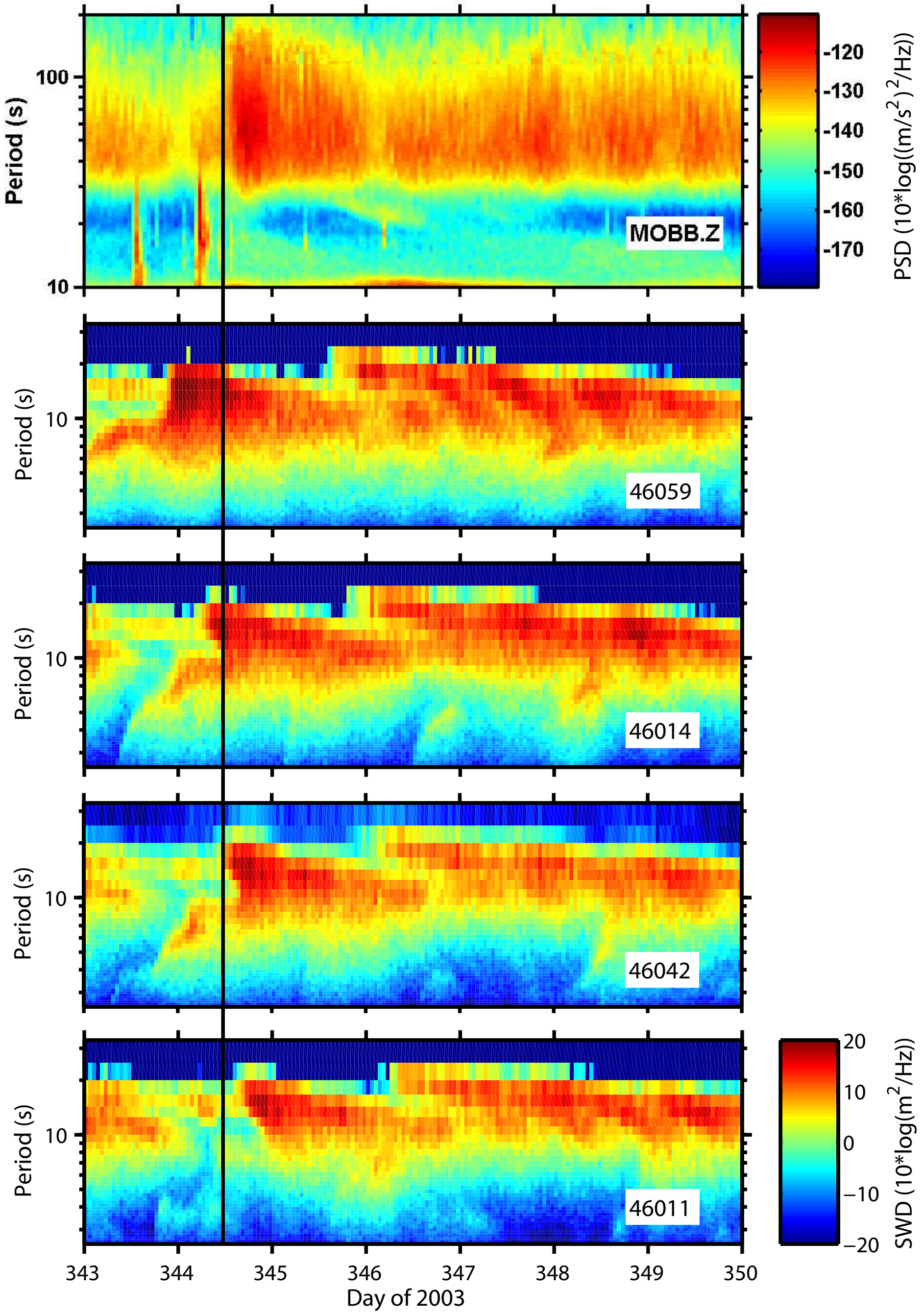

Figure 7.4: Top panel shows the power spectral density (PSD) for the vertical MOBB channel as a function of period and time. Bottom panels show the spectral wave density (SWD) calculated at 4 buoys. The vertical line indicates a sudden change of the infragravity peak width.

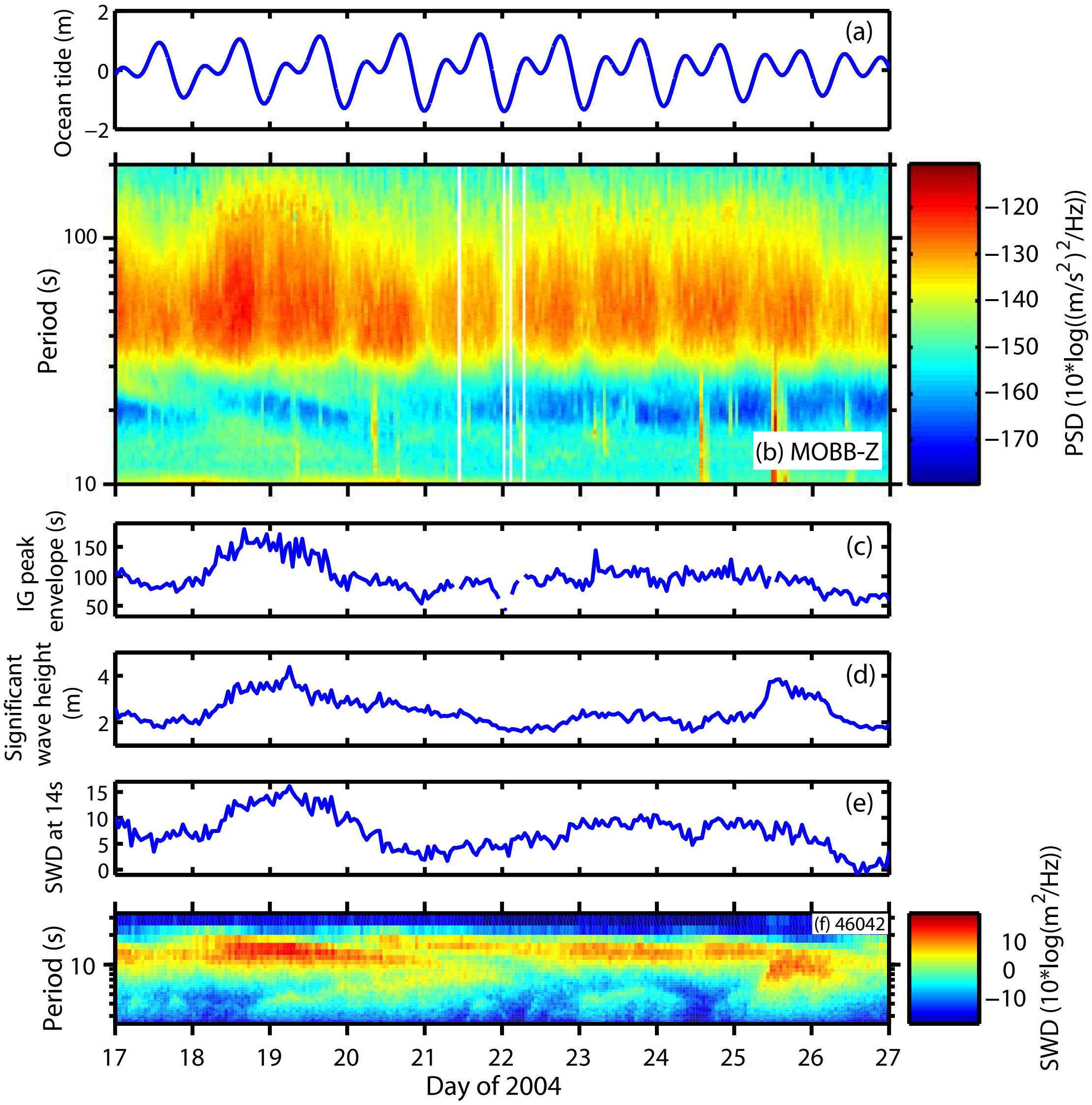

Figure 7.5: (a) Theoretical ocean tide at the MOBB location. (b) The power spectral density (PSD) for the vertical MOBB channel as a function of period and time. White lines indicate hours with some missing data. (c) The envelope of the infragravity peak presented in Figure 7.5b, taken at the long-period end, at the PSD value of -136 dB. (d) The significant wave height at the buoy 46042. (e) The spectral wave density (SWD) in the 14.3 s period bin at the buoy 46042. (f) The SWD at the buoy 46042.

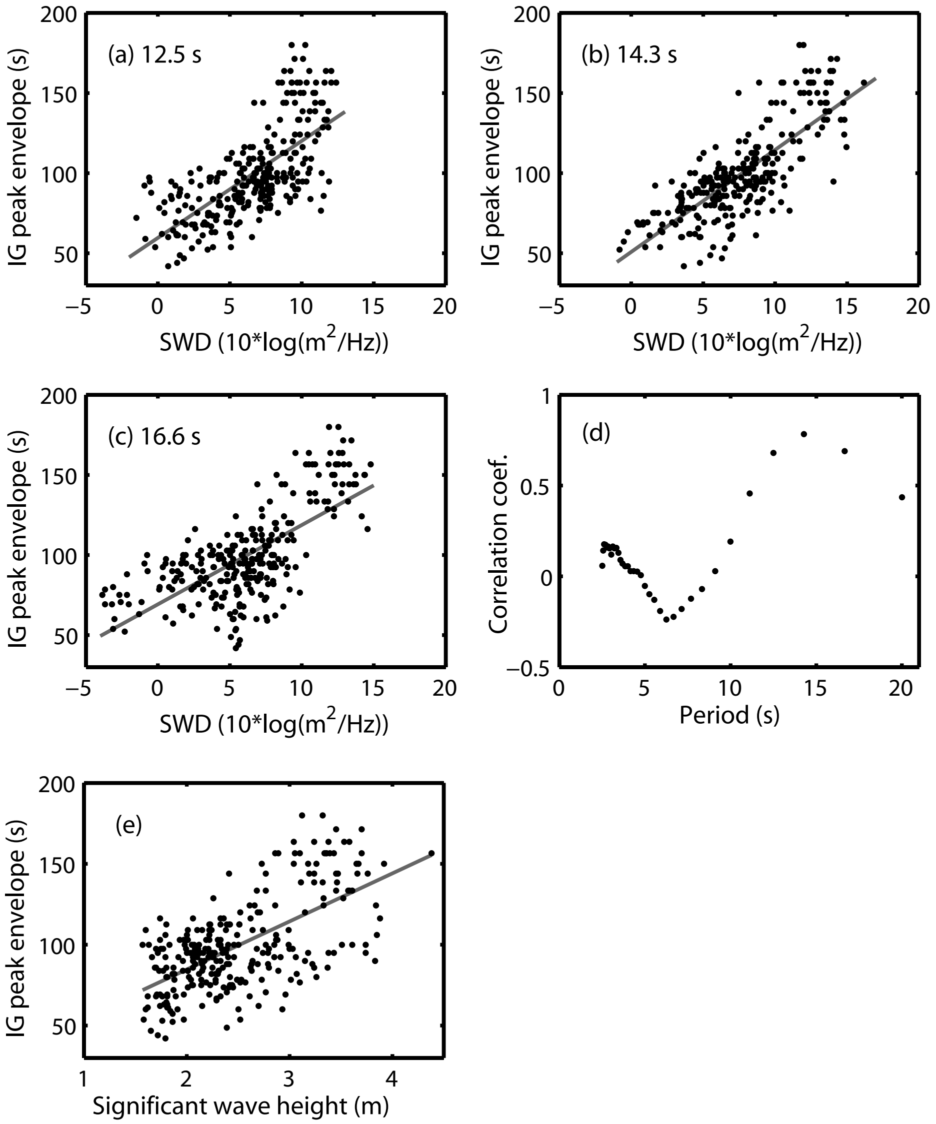

Figure 7.6: (a-c) The period of the infragravity peak envelope, taken at the long-period end, at the PSD value of -136 dB, as a function of the SWD observed at buoy 46042 in the 12.5, 14.3, and 16.6 s period bins. (d) The correlation coefficient between the period of the infragravity peak envelope and the SWD observed in the individual bins at buoy 46042, as a function of the SWD bin period. (e) The period of the infragravity peak envelope as a function of the significant wave height as observed at the buoy 46042. Gray lines show best linear fits to the data.

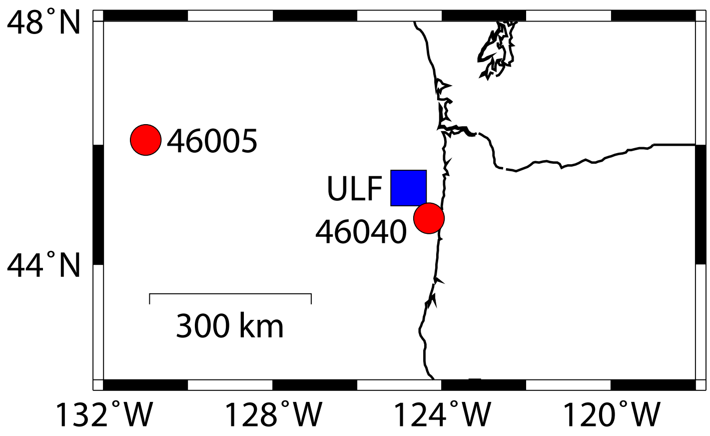

Figure 7.7: The location of the Oregon ULF station and the two closest NOAA buoys that had spectral wave density data available for the time period of the Oregon ULF/VLF experiment.

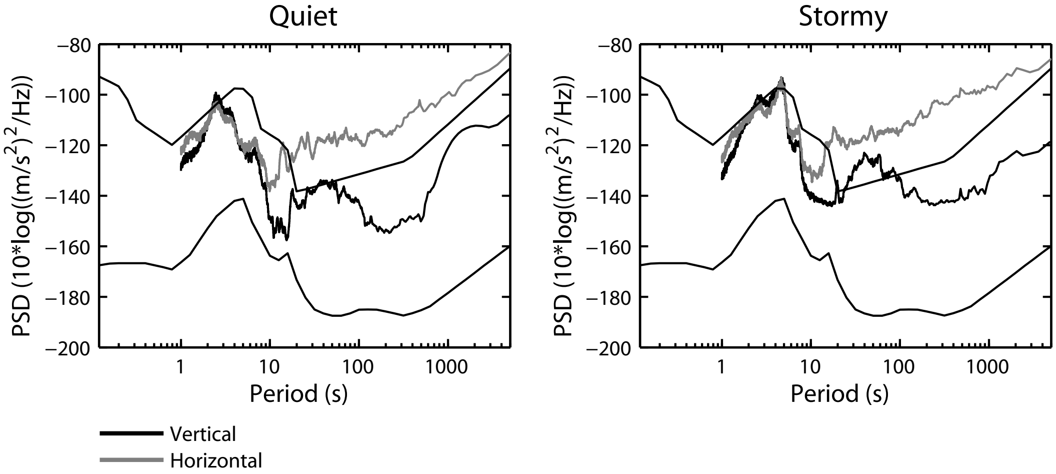

Figure 7.8: Comparison of the power spectral density (PSD) at the Oregon ULF station for a quiet day (1999, day 200, 07-11 UTC) and for a stormy day (1999, day 205, 06-10 UTC). Results obtained for the vertical (black) and for the horizontal component that was rotated 176.3° from North (gray) are shown. The USGS high- and low-noise models for land stations are shown as thin black lines [*Peterson*, 1993].

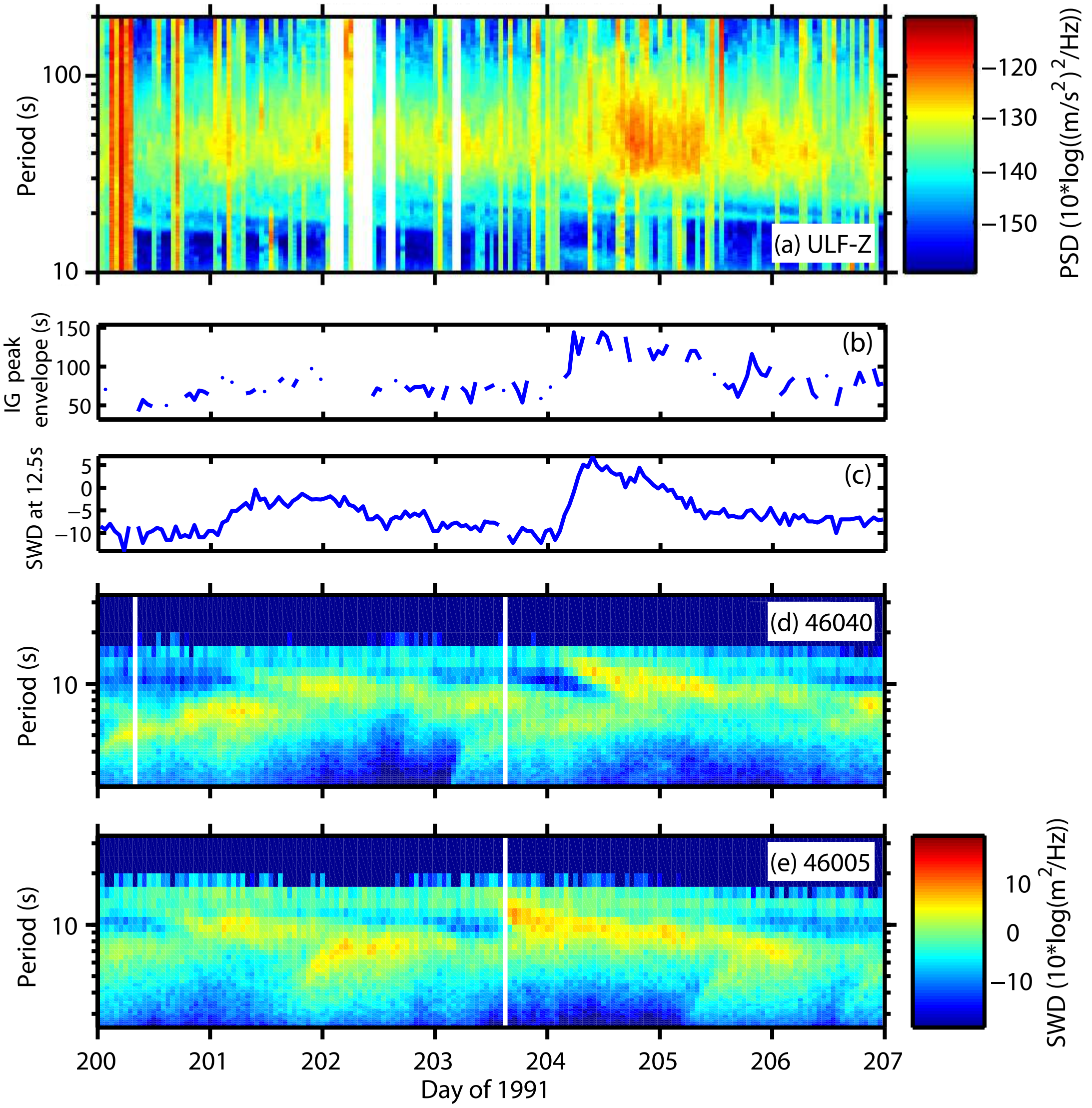

Figure 7.9: (a) The power spectral density (PSD) for the Oregon ULF vertical channel as a function of period and time. White lines indicate hours with some missing data. (b) The envelope of the infragravity peak presented in Figure 7.9a, taken at the long-period end, at the PSD value of -136 dB. (c) The spectral wave density (SWD) in the 12.5 s period bin at the buoy 46040. (d) The SWD at the buoy 46040. (e) The SWD at the buoy 46005.

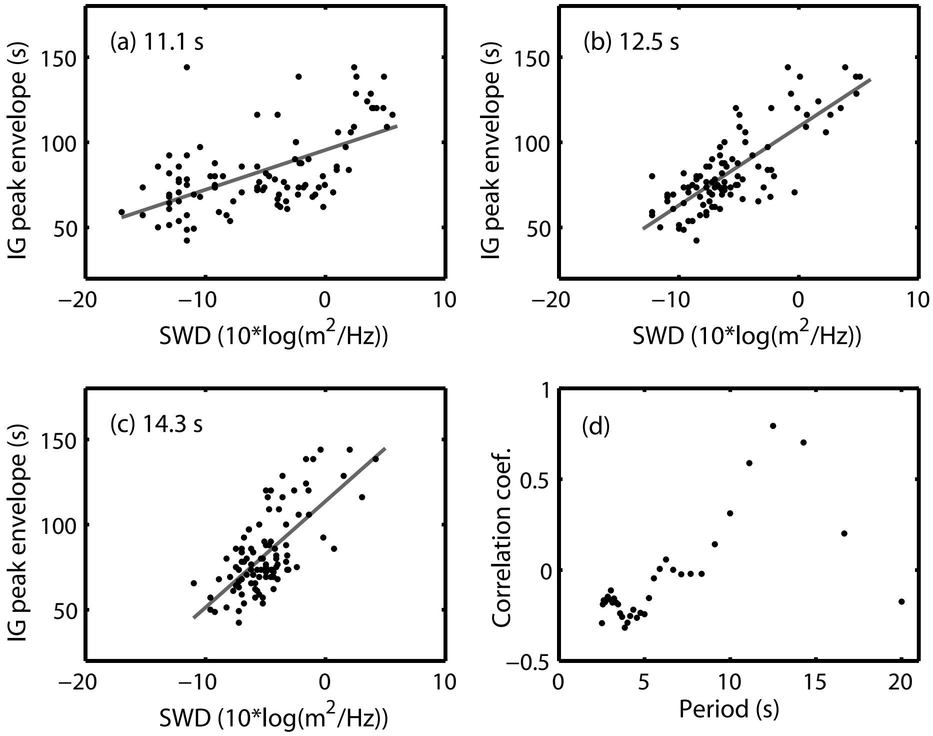

Figure 7.10: (a-c) The period of the infragravity peak envelope, taken at the long-period end, at the PSD value of -136 dB, as a function of the SWD observed at buoy 46040 in the 11.1, 12.5, and 14.3 s period bins. Gray lines show best linear fits to the data. (d) The correlation coefficient between the period of the infragravity peak envelope and the SWD observed in the individual bins at buoy 46040, as a function of the SWD bin period.

Chapter 8

Observations of infragravity waves at the ocean bottom broadband station KEBB offshore Washington

Summary

In addition to the results presented in Chapter 7, I have performed a similar analysis with the seismic data recorded at the ocean bottom broadband station KEBB, located 330 km offshore Washington, at a water depth of 2376 m. Although the station KEBB is located deeper than the 1000-m deep ocean bottom station MOBB, the infragravity waves signal can still be observed on stormy and quiet days. When compared to the energy of the short-period ocean waves recorded at the buoys in the region, infragravity waves observed at KEBB are found to be generated from shorter-period waves in the coastal region and not when the shorter-period waves pass directly above KEBB.

8.1 Introduction

The ocean bottom broadband station KEBB is part of the NEPTUNE project (www.neptune.washington.edu) whose goal is to establish a regional ocean observatory in the northeast Pacific Ocean. One of the long-term plans of the NEPTUNE project is to install a broadband seismic array that would cover the entire Juan de Fuca/Gorda/Explorer plate system. In August 2003, station KEBB was installed as the first NEPTUNE broadband station at the center of the Endeavour segment of the Juan de Fuca ridge, at the northern boundary of the Juan de Fuca plate. This was a collaborative effort between the University of Washington, Monterey Bay Aquarium Research Institute (MBARI), and University of Oregon. The KEBB is located 330 km offshore Washington, at a water depth of 2376 m (Figure 8.1). At present, KEBB is autonomous and the data are on average retrieved once every year.

The KEBB includes a broadband seismometer, a 3-component Guralp CMG 1-T, sensitive over a frequency range of 2.8 mHz (360 s) to 50 Hz. The seismometer is completely buried in sediment inside a 60 cm deep by 60 cm diameter caisson. A 20 m cable connects the sensor to a data logger and battery package [*McGill et al.*, 2003; *McGill et al.*, 2004].

8.2 Results

Locations of the KEBB and the closest NOAA as well as Canadian Marine Environmental Data Service (MEDS) buoys are shown in Figure 8.1. Despite the dense buoy coverage in the region, none of them are located as close to KEBB as buoy 46042 is to the MOBB. The closest buoy to KEBB is 46132, located 216 km to the NNE. The water depth at the locations of the buoys closest to KEBB is listed in Table 8.1.

I first compared the power spectral density (PSD) for the vertical broadband seismic data at KEBB, MOBB, and YBH. Station YBH is one of the quietest BDSN stations, located 560 km north of MOBB. Results obtained for a quiet day (2003, day 260) and for a stormy day (2003, day 281) are shown in Figure 8.2. Four hours of data (00-04 UTC) were used in the calculation. There were no significant earthquakes recorded during the two time periods. On a quiet day MOBB data show a noise "hump" between 20 and 200 s that is not present in the land (YBH) data. The KEBB data also show a noise "hump" that extends to 200 s period, but it starts at a longer period, at about 30 s. On a stormy day the noise extends to 400 s period at KEBB. The infragravity "hump" at MOBB is observed until just above 200 s period. The noise "hump" starts at longer periods at KEBB than at MOBB because KEBB is located deeper than MOBB and is shielded against pressure signal from the higher frequency infragravity waves (hydrodynamic filtering). We can predict the short-period cutoff value for the noise "hump" using the same approach as previously described in Chapter 7 (see Equations 7.1 and 7.2). For KEBB water depth H=2376 m and kH=10.1 from the MOBB example, we obtain the short-period cutoff value of 30.5 s for KEBB. This agrees well with the observed value of $\sim$30 s. The additional water column at KEBB also results in overall lower height of the noise "hump". The two sharp peaks observed at KEBB between 10 and 20 s period are present throughout the period that we analyzed (2003.260-282, 2003.310-365) and are probably due to instrumental noise.

I computed PSD for 1-hour long segments for the vertical KEBB data and compared the results to the spectral wave density (SWD) measured at the closest NOAA and Canadian MEDS buoys (see Figure 8.1). Comparison spectrograms for a 7-day period (12/20-27/2003) are presented in Figure 8.3. The infragravity peak can be observed for the vertical KEBB channel throughout the 7-day period (Figure 8.3, top panel). A sudden change of the infragravity peak width and intensity is indicated with a black line. The bottom panels in Figure 8.3 show the SWD measured at the closest buoys ordered by longitude. The storm on day 359 was approaching from the NW direction and the increased energy of the 10-20 s ocean waves can therefore first be seen on deep ocean buoy 46036, and last on buoy 46041. When the short-period ocean waves arrive at buoys 46005 and 46132, they also reach KEBB, as the line 46005-KEBB-46132 is almost perpendicular to the storm direction. But this does not result in stronger infragravity waves signal at KEBB. Instead, the infragravity waves signal at KEBB increases only when the shored period ocean waves reach the near-shore buoy 46041, located over the continental shelf. This clearly tells us that the infragravity waves are generated near the shore. Once generated, they then propagate back into the deeper ocean.

8.3 Discussion

Although KEBB is installed at more than double water depth when compared to MOBB, the observed signal due to infragravity waves is still an important noise source and post-processing will be needed to clean the observations for earthquake studies (see Chapter 9). About 77% of the world's oceans are relatively deep (over 3000 m in depth) and signal due to infragravity waves at deeper stations is expected to have smaller amplitude and start at longer periods. In addition to installing the seismic stations in deeper ocean, the noise due to infragravity waves can also be reduced by installing the seismometer in a borehole instead of just burying it in the ocean floor. Since deformation signal only slowly decays with depth, borehole installation can significantly improve the signal-to-noise ratio only if the sensor is installed at more than 1 km below the surface [*Webb & Crawford*, 1999]. At the moment such ocean bottom borehole installations are significantly more expensive than buried installations. Also, the ocean bottom station installation, maintenance, and data retrieval are all significantly more challenging and expensive in the deep ocean. We can therefore expect that the post-processing of the ocean bottom data will be an important tool to increase the signal-to-noise ratio for seismic observations in the near future.

8.4 Future work

In August 2004 two additional ocean bottom broadband seismometers were installed [*Wilcock et al.*, 2004] as part of the NEPTUNE project. One of them is located in the middle of the Explorer plate and the other near the Nootka fault zone, about 207 km NNE of the KEBB. The data from the mid-Explorer plate instrument have recently been recovered (A. Barclay, personal communication, 2005). Comparison of the data recorded at the new broadband seismic station and more recent KEBB data for the same period should enable us to learn more about the generation and propagation of the infragravity waves. Once the data from the additional ocean bottom stations become available, we plan to apply array techniques to measure the directionality and dispersion properties of the seismic signal generated by the infragravity waves.

Table 8.1: Water depth at the locations of the buoys closest to KEBB, shown in red in Figure 8.1.

Buoy	Water depth (m)
46036	3500
46132	2040
46206	73
46041	132
46005	2780

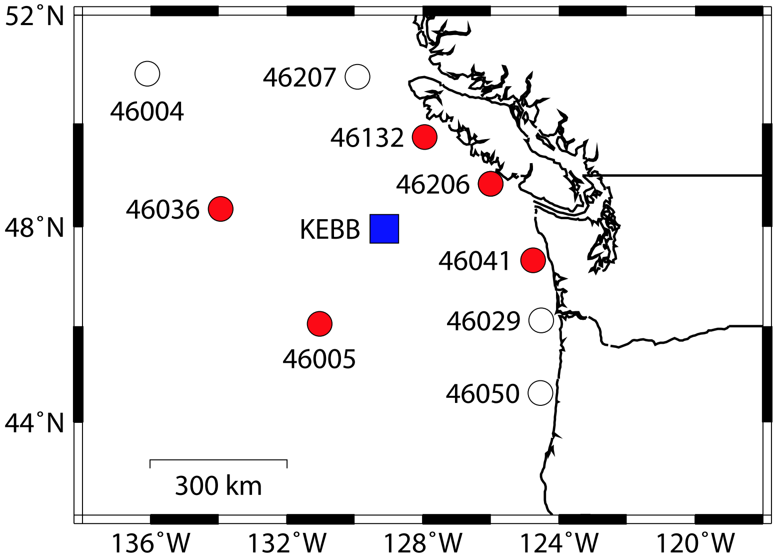

Figure 8.1: The location of the ocean bottom broadband station KEBB and some of the closest NOAA and Canadian MEDS buoys. Data from the buoys shown in red are presented in Figure 8.3

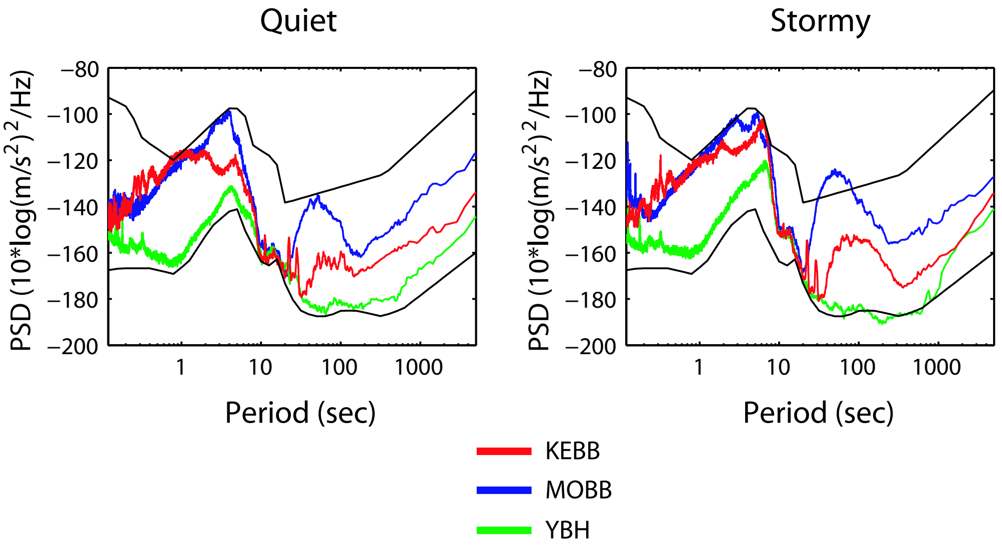

Figure 8.2: Comparison of the power spectral density (PSD) at the stations KEBB, MOBB, and YBH calculated for a quiet day (2003, day 260) and for a stormy day (2003, day 281). Results for the vertical component are shown. The USGS high- and low-noise models for land stations are shown in black [*Peterson*, 1993]. The KEBB data was provided by William Wilcock and Andrew Barclay and was collected with a grant from the W. M. Keck Foundation to John Delaney at the University of Washington to support prototype experiments for Project NEPTUNE.

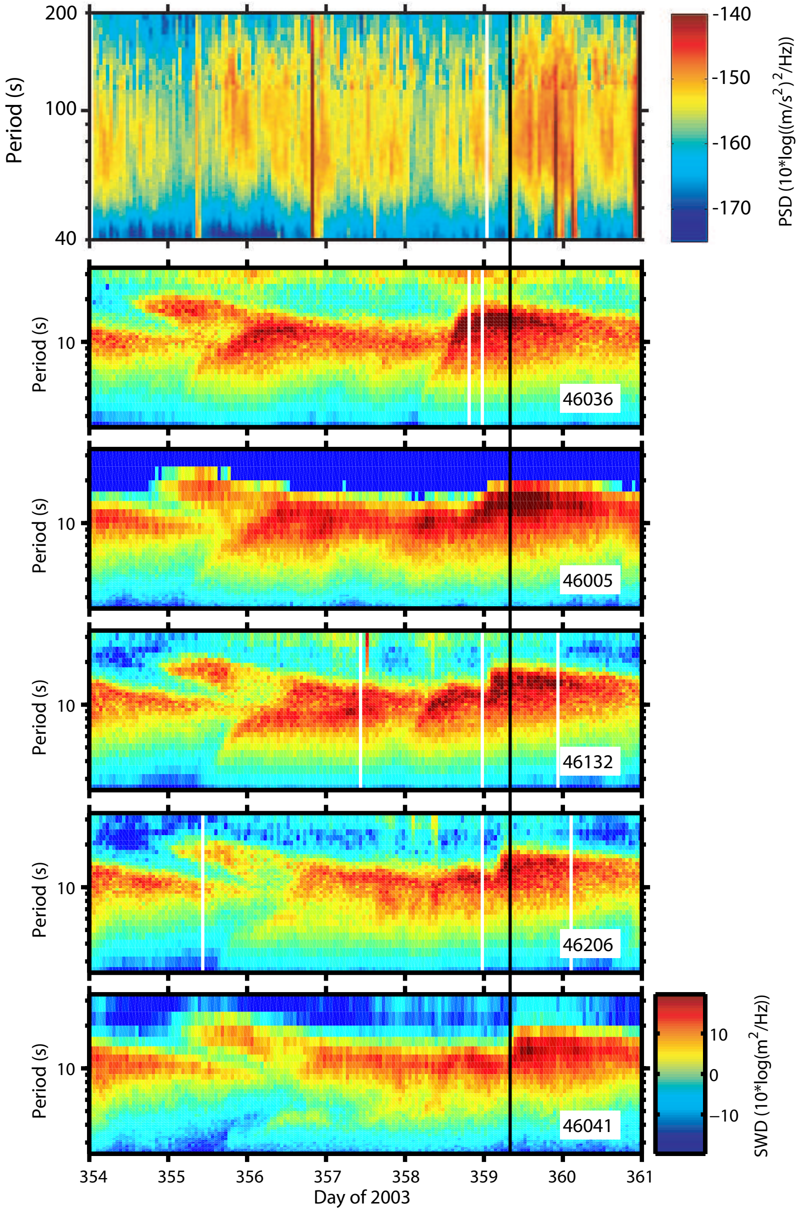

Figure 8.3: Top panel shows the power spectral density (PSD) for the vertical KEBB channel as a function of period and time. Bottom panels show the spectral wave density (SWD) calculated at 5 buoys. The vertical line indicates a sudden change of the infragravity peak width. The KEBB data was provided by William Wilcock and Andrew Barclay and was collected with a grant from the W. M. Keck Foundation to John Delaney at the University of Washington to support prototype experiments for Project NEPTUNE.

Chapter 9

Identifying and removing noise from Monterey ocean bottom broadband seismic data

Summary

When compared to the quiet land stations, ocean bottom seismic station MOBB shows increased background noise for periods longer than 20 s, in the passband of interest for the study of regional and teleseismic signals. This is mainly due to the signal from the infragravity waves and ocean currents. Observations at MOBB also show additional signal-generated noise due to reverberations in the shallow sedimentary layers as well as in the water layer. I present results of removing the long-period noise from the seismic observations by subtracting the coherent signals derived from the pressure measurements. I also present results of the modeling of the signal-generated noise in the near-surface layers and examples of removing the signal-generated noise

using a deconvolution.

9.1 Introduction

Before and during the deployment of the broadband seismometer at the ocean bottom in the Monterey Bay, a number of steps were taken to minimize the instrument generated noise as well as noise induced by the ocean currents. These included insulating the pressure vessel with Mylar insulation, filling it with argon gas, covering the seismometer package with glass beads to prevent currents in the PVC caisson, and burying the PVC caisson below the seafloor level (see Chapter 6, Figures 6.2, 6.3, and 6.4). The remaining long-period background noise observed at MOBB is primarily due to pressure forcing from infragravity ocean waves (seafloor "compliance"; see Chapter 7, Figure 7.2). Many local, regional, and teleseismic events during the past 4 years have shown that strong events are well recorded at MOBB (Figures 9.1, 9.2, and 9.3). But for most events, additional processing is needed to improve the signal-to-noise ratio.

The other type of noise observed at MOBB is signal-generated noise. It is due to reverberations of seismic waves in the shallow sedimentary layers and is particularly strong following the arrival of sharp and strong phases that are often characteristic for strong deep events. This type of noise can also be removed by post-processing by using either the empirical transfer function obtained from a nearby land station, or a synthetic transfer function by modeling the response of the shallow structure at MOBB. Both types of noise are unavoidable in buried ocean bottom installations and the only way to improve the quality of the recorded seismic data is by post-processing.

9.2 Background noise removal

9.2.1 Time-domain, frequency independent method

A simple method for the removal of the long-period noise is to subtract simultaneously recorded ocean bottom pressure signal from the vertical seismic acceleration signal in time domain. The scale factor by which the pressure signal is multiplied is frequency independent and is linearly estimated from the data. In the past, this method has been used to remove the atmospheric pressure signal from the gravimeter observations made on land for the earth tide studies [*Warburton & Goodkind*, 1977]. Later, it was proposed as a way to remove local barometric pressure from the land vertical seismic records [*Zürn & Widmer*, 1995]. The results obtained with the MOBB data show that this method can also be used to remove long-period background noise from the ocean bottom seismic data. Figure 9.4 shows the result for a 5.5-hour period for which the pressure signal was removed from the vertical seismic acceleration signal in time domain. To illustrate the successful removal of the infragravity "hump", the result shown in Figure 9.4 is presented in frequency domain. The only requirement for this method is that the pressure signal is locally recorded at the ocean bottom. The advantage of this approach is that it is very fast and easy to apply.

9.2.2 Transfer function method

In this method the pressure observations are combined with measurements of the transfer function between vertical seismic and pressure signal to predict the vertical component deformation signal. The predicted signal is then removed from the vertical seismic data in either frequency or time domain [*Webb & Crawford*, 1999; *Crawford & Webb*, 2000]. The transfer function is calculated from the records without earthquakes. Since it is only a function of structure at the MOBB location, it does not change with time and can be applied to all data from this site. Figure 9.5 shows an example of the transfer function method to remove noise from the earthquake free vertical MOBB data. Transfer function between vertical seismic and DPG signal was first computed from the 144 data windows within 2005.034-056 period (Figure 9.5a). This transfer function was then combined with the pressure measurement for 1-hour period on day 2005.035 to predict the vertical component deformation signal. This 1-hour period was not used in the transfer function calculation. The predicted deformation signal was then removed from the recorded vertical component data in frequency domain. The obtained result (Figure 9.5d) shows that most of the infragravity "hump" is removed. Also shown is coherence between the pressure and vertical seismic signal for the selected 1-hour period on day 2005.035 (Figure 9.5c). The method only works when coherence between the two channels used to compute the transfer function is high (almost 1) in the period band of interest (20 to 200 s). This means that the noise observed on the vertical seismic channel indeed results from the pressure signal. Low coherence would suggest that the observed noise comes from other sources (e.g. ocean currents).

Example of the long-period background noise removal for a period that included an earthquake is shown in Figure 9.6. The 1-hour period used in the calculation now included the $M_w6.8$ Hokkaido, Japan event. The same transfer function as described above and shown in Figure 9.5a was used. The result shows that the method successfully reveals seismic phases that were previously hidden in the long-period background noise.

9.3 Signal-generated noise removal

Signal-generated noise due to reverberations of seismic waves in the shallow sedimentary layers may be unavoidable in the buried ocean bottom installations. This type of noise is presented and discussed in Chapter 6 (see Figure 6.12). Also presented in Chapter 6 is an example of the removal of the signal-generated noise by deconvolving the empirical transfer function obtained from a nearby land station JRSC (Figure 6.13). Here I present another approach that can also be used to remove the signal-generated noise from the ocean bottom data. Instead of using the empirical transfer function, a synthetic transfer function is first obtained by 1-D modeling of the shallow structure. The response of the sedimentary layers is modeled using the propagator matrix approach [*Kennett & Kerry*, 1979]. I used a program for a plane wave incident from below on a stack of layers that was written by Lane Johnson of the Lawrence Berkeley National Laboratory. To obtain the response of the 1-D structure without a slow sedimentary layer, I used a previously published 1-D crustal model for this region [*Begnaud et al.*, 2000]. The top layer in this model is 1 km thick and has $v_p = 2.87km/s$, $v_s = 1.657km/s$, and $\rho = 2.0g/cm^3$. I then modified this model by replacing the top 350 m with a slower sedimentary layer with $v_p = 0.324km/s$, $v_s = 0.196km/s$, and $\rho = 1.3g/cm^3$, and calculated the response of the updated model. The thickness of the added sedimentary layer agrees with what is expected for the region of Smooth Ridge where MOBB is installed (sedimentary section less than 1 km total, R. Whitmarsh, personal communication, 2003). The seismic velocities used for the added sedimentary layer were taken from the USGS velocity model [*Jachens et al.*, 1997] where they were assigned to the San Francisco Bay shallow sediments. The synthetic transfer function was obtained by the spectral division of the result obtained with the 1-D model with the additional sedimentary layer and the result obtained with the original 1-D crustal model. The synthetic transfer function was than used to deconvolve the signal-generated noise from the MOBB vertical channel (Figure 9.7d). The result obtained after removing the empirical transfer function constructed using MOBB and FARB data is shown in Figure 9.7c for comparison. Results presented in Figure 9.7 show that both methods can successfully remove the signal-generated noise from the MOBB data and that the obtained results are similar to the waveforms observed at the land station (Figure 9.7b).

To test the stability of the synthetic deconvolution approach, I used the above described method with the the transfer functions for slightly perturbed 1-D structures.

Results obtained with 25 different 1-D models are shown in Figure 9.8. The top layer thickness of the models varied from 250 m to 450 m and the top layer seismic velocities were changed for up to 20% from the above used sedimentary layer values. The misfit between the cleaned MOBB and FARB waveforms was evaluated by the variance reduction that is listed in each panel. The central panel corresponds to the model described above and presented in the Figure 9.7d. The results show that models with a slightly thicker and faster, as well as slightly thinner and slower top layer also remove significant portion of the observed signal-generated noise at MOBB. The model with a 350 m thick top layer used in Figure 9.7d remained the favorite model as, in addition to a large variance reduction, it also resulted in good agreement of the amplitudes of the strongest seismic phases observed at FARB and cleaned MOBB records.

9.4 Discussion

The methods described above will be an important tool to remove noise from the seismic data recorded at the ocean bottom buried installations. Both methods used to remove long-period background noise use the pressure signal that was recorded locally at the ocean bottom. This shows that it is extremely important to have a reliable pressure sensor collocated with every ocean bottom seismometer. It is also important that the sampling rate for the DPG and other environmental data (temperature, ocean current meter) is high enough so that they can be used in the post-processing for the complete seismic frequency band.

Other studies [*Crawford & Webb*, 2000; *Stutzmann et al.*, 2001] suggest that tilt-generated seismic background noise due to ocean currents can also be an important noise source for seismic instruments that are not well leveled. Current-induced tilt noise is mainly caused by seafloor currents flowing past the instrument and by eddies spun off the back of the instrument [*Webb*, 1988; *Duennebier & Sutton*, 1995]. The MOBB sensor is buried below the seafloor and was well leveled during the installation, therefore the tilt noise should not be significant. Preliminary analysis of the MOBB data confirmed that the coherence between noise recorded on the vertical and horizontal channels is low. I tried to apply the same technique as described above to remove the pressure signal from the vertical data, but this time using the horizontal and vertical channels. I first computed the transfer function between horizontal and vertical channels and then subtracted the predicted vertical deformation from the observed vertical signal. The preliminary results show that there is almost no improvement, suggesting that the tilt noise is not important at MOBB.

9.5 Future work

We will further investigate coherence between vertical and horizontal seismic channels, as well as coherence between the seismic channels and other measured environmental variables such as temperature and current flow that are also measured at MOBB. In case high coherence between any of the above observables and either of the seismic channels is observed, we will use it to further clean the seismic data. We will also further test the stability of the transfer function between the pressure and vertical seismic channel and set up an automatic routine that will remove noise from the MOBB vertical seismic channel. Once MOBB is connected to the cable, we plan to do this type of processing in real time.

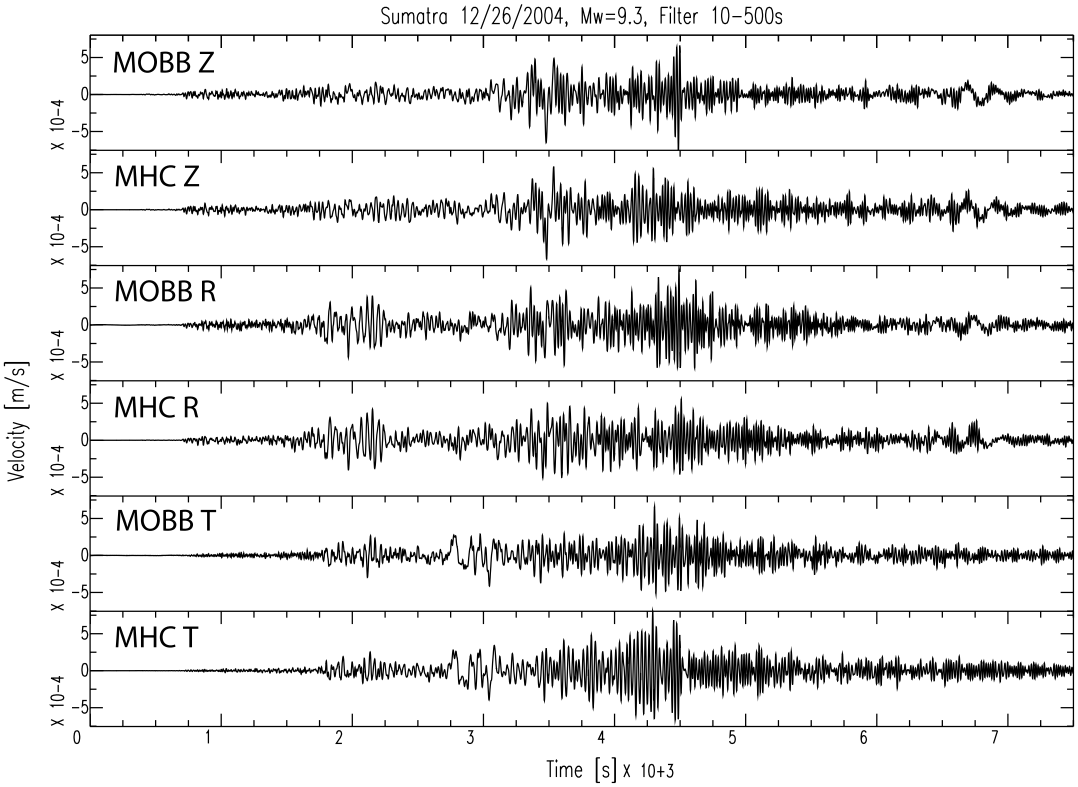

Figure 9.1: Comparison of the great Sumatra $M_w 9.3$ 12/26/2004 earthquake recorded at MOBB and MHC. Vertical, radial, and transverse components are shown. Waveforms were bandpass filtered between 10 and 500 s. Shown time window is 125 min long.

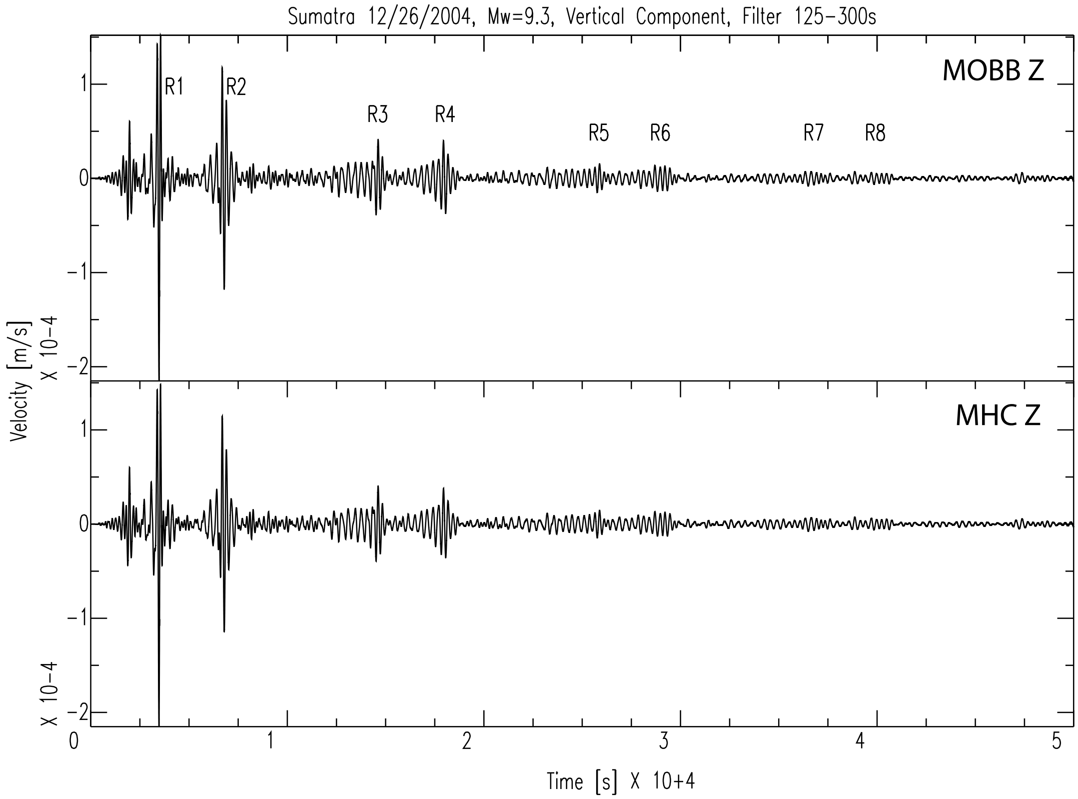

Figure 9.2: Comparison of the Rayleigh waves from the great Sumatra M_w9.3 12/26/2004 earthquake recorded on the vertical component at MOBB and MHC. Waveforms were bandpass filtered between 125 and 300 s. Shown time window is 13.9 hours long.

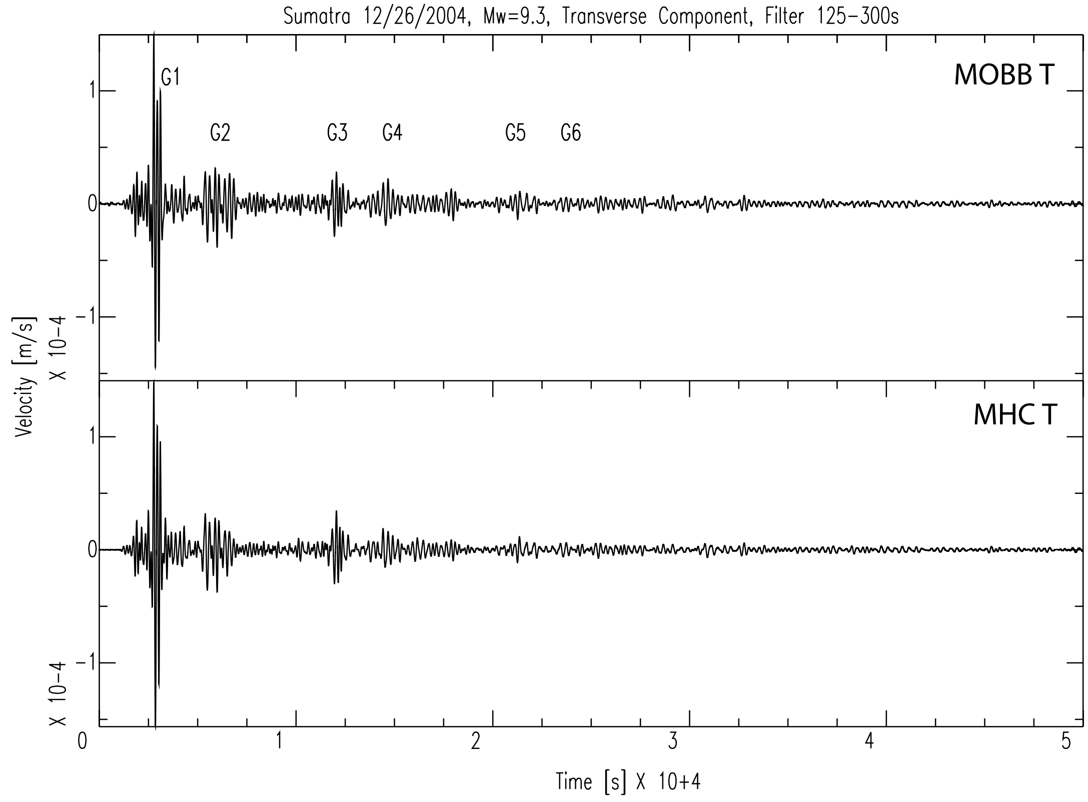

Figure 9.3: Comparison of the Love waves from the great Sumatra $M_w 9.3$ 12/26/2004 earthquake observed on the transverse component at MOBB and MHC. Waveforms were bandpass filtered between 125 and 300 s. Shown time window is 13.9 hours long.

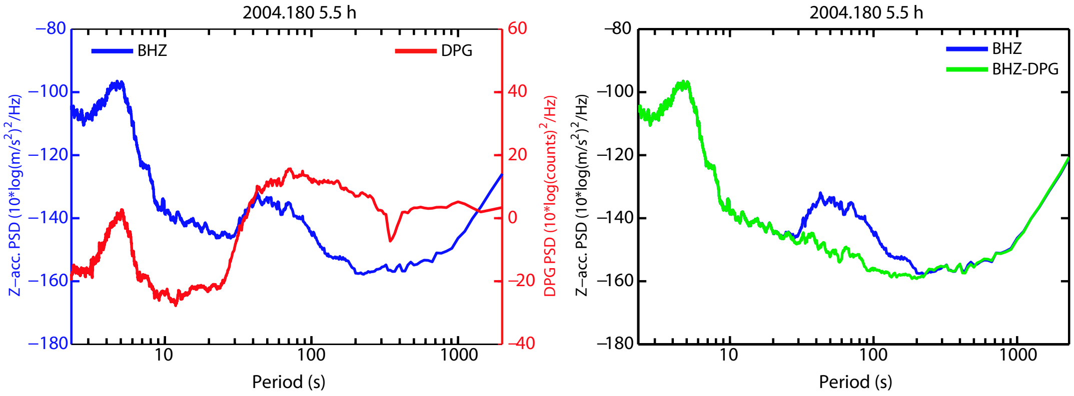

Figure 9.4: Left: Power spectral density (PSD) calculated for a 5.5-hour period without earthquakes for the vertical seismic channel (blue) and the DPG (red). At periods longer than 20 s the infragravity "hump" is observed for both datasets. Right: PSD for the vertical seismic channel before (blue) and after (green) the time-domain subtraction of the DPG signal. Most of the infragravity "hump" is removed from the seismic data.

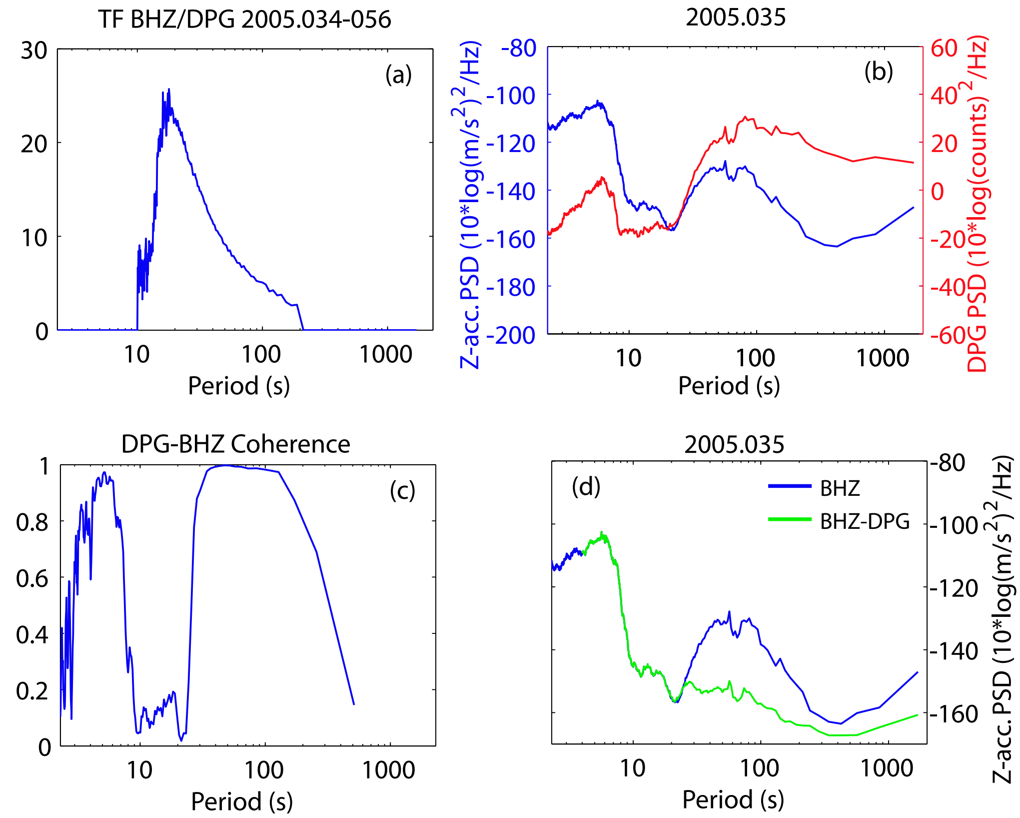

Figure 9.5: Example of the transfer function method to remove noise from the earthquake-free vertical data. (a) Transfer function between vertical seismic and DPG signal calculated from 144 1-hour data windows within 2005.034-056 period. (b) Power spectral density (PSD) for a 1-hour period without earthquakes for the vertical seismic channel (blue) and DPG (red). (c) Coherence between the vertical seismic and DPG channel for the selected 1-hour period. (d) PSD for the vertical seismic channel before (blue) and after (green) the noise removal using transfer function shown in (a).

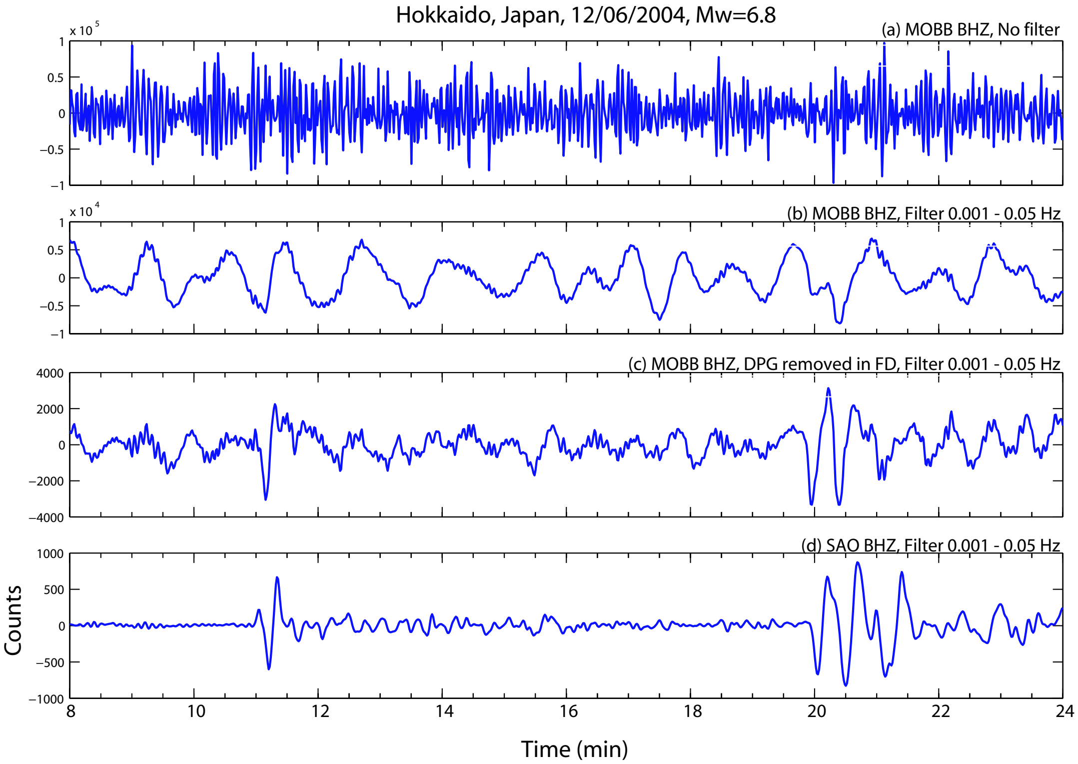

Figure 9.6: Example of the long-period background noise removal for the M_w6.8 Hokkaido, Japan earthquake using the transfer function shown in Figure 9.5a. (a) Original MOBB vertical data. (b) MOBB data bandpass filtered between 0.001 and 0.05 Hz. (c) MOBB data after removal of the coherent DPG signal and bandpass filtered between 0.001 and 0.05 Hz. (d) SAO data bandpass filtered between 0.001 and 0.05 Hz.

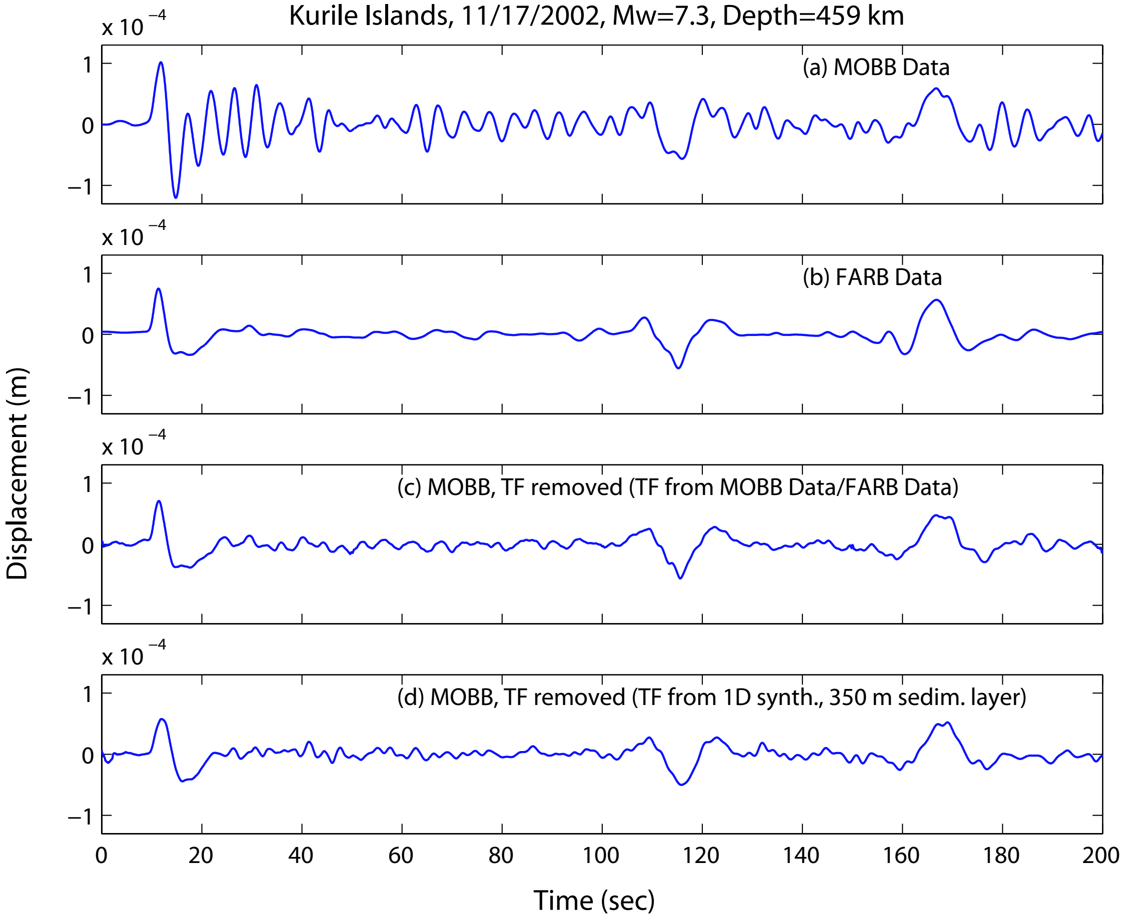

Figure 9.7: Two examples of deconvolution of signal-generated noise at MOBB for the event shown in Figure 6.12. (a) Original MOBB data. (b) Original FARB data. (c) MOBB data after removing empirical transfer function constructed using MOBB and FARB data. (d) MOBB data after removing a synthetic transfer function obtained by 1-D modeling of the shallow structure (350 m layer with $v_p = 0.324 km/s$, $v_s = 0.196 km/s$, and $\rho = 1.3 g/cm^3$

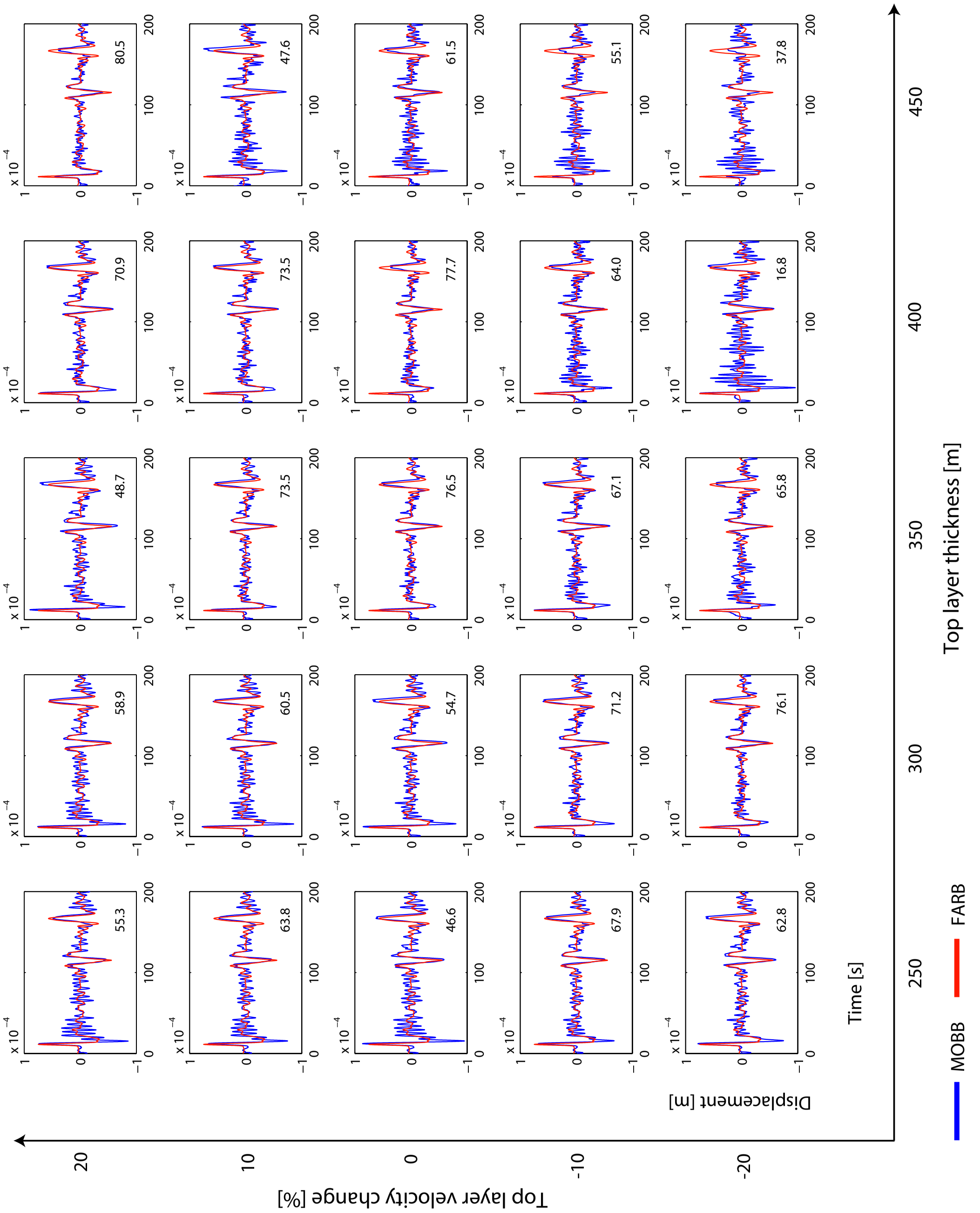

Figure 9.8: Deconvolution of signal-generated noise at MOBB for the event shown in Figures 6.12 and 9.7. The MOBB data after removing a synthetic transfer function are compared to observations at FARB. Results obtained with the transfer functions calculated for 25 different 1-D models are shown. Models varied in the top layer thickness and the top layer seismic velocities. The top layer seismic velocities used in Figure 9.7d were changed for up to 20%. Listed in each panel is the variance reduction.

Chapter 10

Summary

In this work I examined two topics that are both directly related to the goals of modern seismology - to record present day seismicity, study it to learn about the earth's structure and earthquake sources, and then model possible future events to provide reliable ground motion estimates.

The first study focused on the structure of the Santa Clara Valley (SCV) basins. Since it is well known that ground motions resulting from earthquakes are stronger and have longer duration over the basins, it is important to have a reliable velocity model for this region. I first studied the teleseismic P-waves observed during the 1998 SCV seismic experiment and found that P-wave amplification and P-wave energy are strongly correlated with the arrival-time delays. The results also showed that the arrival-time delays on the order of ±0.25 s correlate strongly with the basin depth in the available velocity models. I used finite-difference simulations with UCB and two USGS model versions to show that the observations may be reproduced by either of the 3D velocity models, although refinements to the proposed 3D structure for the SCV basins are needed. In addition I examined the microseisms that were recorded during the SCV seismic experiment. The observed seismic noise is related to the ocean wave heights measured on the offshore weather buoy. The analysis of the microseisms showed that spectral ratio of the horizontal to vertical microseisms observed at SCV seismic stations is stable with time and that the period of its dominant peak is related to basin depth. Results from two local events recorded at the SCV seismic array showed that seismic wave energy and peak ground velocities increase with the travel-time delays determined from the teleseismic events and with the basin depth from the USGS model. I calculated empirical relationships between the seismic observations and the basin depth which may be used to further revise and validate basin structure in the SCV. Also, I started to develop simultaneous inversion of the teleseismic, local earthquake, and microseism data to refine the velocity structure in the SCV basins. Synthetic tests using the teleseismic data show that the method is stable and suggest that the basin model structure can be improved.

In the second study I examined the observed seismic data from the Monterey ocean bottom broadband seismic station (MOBB) as well as from two other ocean broadband stations located offshore Oregon and Washington. The need for the extension of the seismic networks into the oceans has long been recognized, and recent technological advances have made permanent broadband ocean bottom stations possible. I used the long-period background noise observed at the buried ocean bottom stations to study the properties of the infragravity waves. I compared the infragravity waves signal from the three ocean bottom stations to the energy of the short-period ocean waves recorded at the local buoys. Results showed that infragravity waves are generated from the short-period ocean waves in the nearshore region. Observations at MOBB also showed two types of infragravity waves signal modulation. The first one is in-phase with tides which is possibly a result of the nonlinear exchange of energy between the short-period waves and tidal currents. The second one, a longer-period modulation, is found to be best correlated with the energy of the 12-14 s period ocean waves, suggesting that this waves are most important for the infragravity waves generation. I also explored ways to remove the long-period background noise from the ocean bottom seismic data. I showed that a simple approach of subtracting the simultaneously recorded bottom pressure works well. I also explored a more advanced method that is frequency dependent and uses a transfer function between vertical seismic and pressure signal to predict the vertical component deformation signal which can be removed in either frequency or time domain. Results showed that the signal-to-noise ratio for seismic observations can be improved significantly and that most of the long-period noise from the infragravity waves can be removed. In addition I showed that signal-generated noise observed at MOBB due to reverberations of seismic waves in the shallow sedimentary layers can also be removed by post-processing. I used an empirical approach in which a transfer function is first calculated using the data from a nearby land station and then removed the signal-generated noise by deconvolution. I also showed that another approach can be used that does not require data from a land station. In this case a synthetic transfer function is first obtained by modeling the 1D shallow structure at the location of the ocean bottom station. The explored methods to remove background as well as signal-generated noise from the MOBB data showed that they work well and that future MOBB type seismic stations will help us learn more about the earth's structure and earthquake sources.

Bibliography

Agnew, D. C., SPOTL: Some programs for ocean-tide loading, SIO Ref. Ser. 96-8, 35 pp., Scripps Inst. of Oceanogr., La Jolla, Calif., 1996.

Aoi, S., Boundary shape waveform inversion for estimating the depth of three-dimensional basin structures, *Bull. Seism. Soc. Am.*, **92**, 2410-2418, 2002.

Araki, E., M. Shinohara, S. Sacks, A. Linde, T. Kanazawa, H. Shiobara, H. Mikada, and K. Suyehiro, Improvement of seismic observation in the ocean by use of seafloor boreholes, *Bull. Seism. Soc. Am.*, **94**, 678-690, 2004.

Beauduin, R., J.-P. Montagner, J.-F. Karczewski, Time evolution of broadband seismic noise during the French Pilot experiment OFM/SISMOBS, *Geophys. Res. Lett.*, **23**, 2995-2998, 1996.

Begnaud, M. L. and D. S. Stakes, Constraining continental margin seismicity by extending on-shore seismograph stations to critical off-shore sites, *Bull. Seism. Soc. Am.*, **90**, 414-424, 2000.

Begnaud, M. L., K. C. McNally, D. S. Stakes, and V. A. Gallardo, A crustal velocity model for locating earthquakes in Monterey Bay, California, *Bull. Seism. Soc. Am.*, **90**, 1391-1408, 2000.

Beranzoli L., A. De Santis, G. Etiope, P. Favali, F. Frugoni, G. Smriglio, F. Gasparoni, and A. Marigo, GEOSTAR A GEophysical and Oceanographic STation for Abyssal Research, *Phys. Earth Planet. Inter.*, **108** (2), 175-183, 1998.

Bodin, P. and S. Horton, Broadband microtremor observation of basin resonance in the Mississippi embayment, Central US, *Geophys. Res. Letters*, **26**, 903-906, 1999.

Bodin, P., K. Smith, S. Horton, and H. Hwang, Microtremor observations of deep sediment resonance in metropolitan Memphis, Tennessee, *Engineering Geology*, **62**, 159-168, 2001.

Brocher, T. E., E. E. Brabb, R. D. Catchings, G. S. Fuis, T. E. Fumal, R. C. Jachens, A. S. Jayko, R. E. Kayen, R. J. McLaughlin, T. Parsons, M. J. Rymer, R. G. Stanley, and C. M. Wentworth, A crustal-scale 3-D seismic velocity model for the San Francisco Bay area, California, *EOS Trans. AGU.*, **78**, F435, 1997.

Brocher, T. M., J. McCarthy, P. E. Hart, W. S. Holbrook, K. P. Furlong, T. V. McEvilly, J. A. Hole, and S. L. Klemperer, Seismic evidence for a lower-crustal detachment beneath San Francisco Bay, California, *Science*, **265**, 1436-1439, 1994.

Brocher, T. M., Compressional and shear wave velocity versus depth in the San Francisco Bay Area, California: Rules for USGS Bay Area Velocity Model 05.0.0, *U.S. Geol. Surv. Open-File Report 2005-1317*, 2005a.

Brocher, T. M., Empirical relations between elastic wavespeeds and density in the Earth's crust, *Bull. Seism. Soc. Am.*, **95**, 2081-2092, 2005b.

Brocher, T. M., A regional view of urban sedimentary basins in northern California based on oil industry compressional-wave velocity and density logs, *Bull. Seism. Soc. Am.*, **95**, 2093-2114, 2005c.

Brocher, T., B. Aagaard, R. Simpson, and R. Jachens, The new USGS 3D seismic velocity model for northern California, *Seism. Res. Lett.*, **77**, 271, 2006.

Bromirski, P. D. and F. K. Duennebier, Seismo-acoustic signals and noise in the near-shore environment, *SOEST Report 95-03*, University of Hawaii, Honolulu, pp. 110, 1995.

Bromirski, P. D. and F. K. Duennebier, The near-coastal microseism spectrum: Spatial and temporal wave climate relationships, *J. Geophys. Res.*, **107**(B8), ESE 5-1, pp. 20, doi:10.1029/2001JB000265, 2002.

Butler, R., A. D. Chave, F. K. Duennebier, D. R. Yoerger, R. Petitt, D. Harris, F. B. Wooding, A. D. Bowen, J. Bailey, J. Jolly, E. Hobart, J. A. Hildebrand, and A. H. Dodeman, Hawaii-2 Observatory pioneers opportunities for remote instrumentation in ocean studies, *EOS Trans. AGU.*, **81**, 157, 162-163, 2000.

Catchings, R. D., G. Gandhok, M. R. Goldman, C. E. Steedman, and R. Hanson, Near-surface structure and velocities of the northeastern Santa Cruz Mountains and the western Santa Clara Valley, California from seismic imaging, *U.S. Geol. Surv. Open-File Report, in press*, 2005.

Catchings, R. D., M. R. Goldman, and G. Gandhok, Structure and velocities of the northeastern Santa Cruz Mountains and the western Santa Clara Valley, California, from the SCSI-LR seismic survey, *U.S. Geol. Surv. Open-File Report 2006-1014*, 2006.

Cerjan, C., D. Kosloff, R. Kosloff, and M. Reshef, A nonreflecting boundary condition for discrete acoustic and elastic wave equations, *Geophysics*, **50**, 705-708, 1985.

Chen, K.-C., J.-M. Chiu, Y.-T. Yang, Shear-wave velocity of the sedimentary basin in the Upper Mississippi Embayment using S-to-P converted arrivals, *Bull. Seism. Soc. Am.*, **86**, 848-856, 1996.

Chuchel, B. A. and R. C. Jachens, Preliminary isostatic residual gravity map of the San Jose 1:100,000 scale quadrangle, California, *U.S. Geol. Surv. Open-File Report 1990-0055*, 1990.

Clayton, R. and B. Engquist, Absorbing boundary conditions for acoustic and elastic wave equations, *Bull. Seism. Soc. Am.*, **67**, 1529-1540, 1977.

Collins, J. A., F. L. Vernon, J. A. Orcutt, R. A. Stephen, K. R. Peal, F. B. Wooding, F. N. Spiess, and J. A. Hildebrand, Broadband seismology in the oceans: Lessons from the Ocean Seismic Network Pilot Experiment, *Geophys. Res. Lett.*, **28**, 49-52, 2001.

COSOD II, Report of the Second Conference on the Scientific Ocean Drilling, Joint Oceanographic Institutions, Inc., Washington, D.C., 142 pp.

Cox, C., T. Deaton, and S. Webb, A deep-sea differential pressure gauge, *J. Atmos. Oceanic Technol.*, **1**, 237-246, 1984.

Crawford, W. C. and S. C. Webb, Identifying and removing tilt noise from low-frequency (<0.1 Hz) seafloor vertical seismic data, *Bull. Seism. Soc. Am.*, **90**, 952-963, 2000.

Dolenc, D., Basin structure influences on the teleseismic wave propagation in the Santa Clara Valley, California, *M.S. Thesis*, University of California, Berkeley, 2001.

Dolenc, D., D. Dreger, and S. Larsen, Basin structure influences on the propagation of teleseismic waves in the Santa Clara Valley, California, *Bull. Seism. Soc. Am.*, **95**, 1120-1136, 2005a.

Dolenc, D. and D. Dreger, Microseisms observations in the Santa Clara Valley, California, *Bull. Seism. Soc. Am.*, **95**, 1137-1149, 2005.

Dolenc, D., B. Romanowicz, D. Stakes, P. McGill, and D. Neuhauser, Observations of infragravity waves at the Monterey ocean bottom broadband station (MOBB), *Geochem., Geophys., Geosys.*, **6** (9), 1-13, doi:10.1029/2005GC000988, 2005b.

Dolenc, D., D. Dreger, and S. Larsen, 3D simulations of ground motions in Northern California using USGS SF06 velocity model, *Seism. Res. Lett.*, **77**, 300, 2006.

Dravinski, M., G. Ding, and K.-L. Wen, Analysis of spectral ratios for estimating ground motion in deep basins, *Bull. Seism. Soc. Am.*, **86**, 646-654, 1996.

Dreger, D. and B. Romanowicz, Source characteristics of events in the San Francisco Bay region, *U.S. Geol. Surv. Open-File Report 94-176*, 301-309, 1994.

Duennebier, J. K. and G. H. Sutton, Fidelity of ocean bottom seismic observations, *Mar. Geophys. Res.*, **17**, 535-555, 1995.

Dziewonski, A., R. Wilkens, and J. Firth, Proceedings of the Ocean Drilling Program, Initial Reports, **136**, 1992.

Elgar, S., T. H. C. Herbers, M. Okihiro, J. Oltman-Shay, and R. T. Guza, Observations of infragravity waves, *J. Geophys. Res.*, **97**, 15,573-15,577, 1992.

Fletcher, J. B., J. Boatwright, and A. G. Lindh, Wave propagation and site response in the Santa Clara Valley, *Bull. Seism. Soc. Am.*, **93**, 480-500, 2003.

Forsyth, D., A. Dziewonski, and B. Romanowicz, Scientific objectives and required instrumentation, in Proceedings of Ocean Seismic Network Workshop "Broadband Seismology in the Oceans: towards a five year plan", 8-18, 1995.

Frankel, A. and J. Vidale, A three-dimensional simulation of seismic waves in the Santa Clara Valley, California, from a Loma Prieta aftershock, *Bull. Seism. Soc. Am.*, **82**, 2045-2074, 1992.

Frankel, A., D. Carver, E. Cranswick, T. Bice, R. Sell, and S. Hanson, Observations of basin ground motions from a dense seismic array in San Jose, California, *Bull. Seism. Soc. Am.*, **91**, 1-12, 2001.

Gee, L., D. Neuhauser, D. Dreger, R. Uhrhammer, and B. Romanowicz, The Rapid Earthquake Data Integration Project, in International Handbook of Earthquake and Engineering Seismology, 81B, 1261-1273, 2003.

Guza, R. T. and E. B. Thornton, Swash oscillations on a natural beach, *J. Geophys. Res.*, **87**, 483-492, 1982.

Hartzell, S., D. Carver, and R. A. Williams, Site response, shallow shear-wave velocity, and damage in Los Gatos, California, from the 1989 Loma Prieta earthquake, *Bull. Seism. Soc. Am.*, **91**, 468-478, 2001.

Herbers, T. H. C., S. Elgar, and R. T. Guza, Generation and propagation of infragravity waves, *J. Geophys. Res.*, **100**, 24,863-24,872, 1995a.

Herbers, T. H. C., S. Elgar, R. T. Guza, and W. C. OŠReilly, Infragravity-frequency (0.005-0.05 Hz) motions on the shelf. Part II: Free waves, *J. Phys. Oceanogr.*, **25**, 1063-1079, 1995b.

Jachens, R. C., A. Griscom, and C. W. Roberts, Regional extent of Great Valley basement west of the Great Valley, California: Implications for extensive tectonic wedging in the California Coast Ranges, *J. Geophys. Res.*, **100**, 12769-12790, 1995.

Jachens, R. C., R. F. Sikora, E. E. Brabb, C. M. Wentworth, T. M. Brocher, M. S. Marlow, and C. W. Roberts, The basement interface: San Francisco Bay area, California, 3-D seismic velocity model, *EOS Trans. AGU.*, **78**, F436, 1997.

Kasahara, J., T. Sato, H. Momma, and Y. Shirasaki, A new approach to geophysical real-time measurements on a deep-seafloor using decommissioned submarine cables, *Earth Planets Space*, **50**, 913-925, 1998.

Kawase, H., The cause of the damage belt in Kobe: The basin edge effect, constructive interference of the direct S-wave with the basin-induced diffracted Rayleigh waves, *Seism. Res. Lett.*, **67**, 25-34, 1996.

Kennett, B. L. N., and N. J. Kerry, Seismic waves in a stratified half space, *Geophys. J. R. Astr. Soc.*, **57**, 557-583, 1979.

Kinsman, B., Wind waves: their generation and propagation on the ocean surface, 676 pp., Prentice-Hall, Englewood Cliffs, N. J., 1984.

Lachet, C., and P.-Y. Bard, Numerical and theoretical investigations on the possibilities and limitations of Nakamura's technique, *J. Phys. Earth*, **42**, 377-397, 1994.

Larsen, S. and C. A. Schultz, ELAS3D: 2D/3D elastic finite-difference wave propagation code, Technical Report No. UCRL-MA-121792, 19 pp., 1995.

Levander, A. R. (1988). Fourth-order finite-difference P-SV seismograms, *Geophysics*, **53**, 1425-1436, 1988.

Lermo, J., and F. J. Chávez-García, Are microtremors useful in site response evaluation?, *Bull. Seism. Soc. Am.*, **84**, 1350-1364, 1994.

Lindh, A. G., J. P. Eaton, M. O. Allen, J. H. Healy, S. W. Stewart, and L. Damerell, Calibration formulae and values for velocity seismometers used in the 1998 Santa Clara Valley, California seismic experiment, *U.S. Geol. Surv. Open-File Report 99-434*, 1999.

Longuet-Higgins, M. S., A theory of the origin of microseisms, *Philos. Trans. R. Soc. London, Ser. A*, **243**, 1-35, 1950.

Longuet-Higgins, M. S. and R. W. Stewart, Changes in the form of short gravity waves on long waves and tidal currents, *J. Fluid Mech.*, **8**, 565-583, 1960.

Longuet-Higgins, M. S. and R. W. Stewart, The changes in amplitude of short gravity waves on steady non-uniform currents, *J. Fluid Mech.*, **10**, 529-549, 1961.

Longuet-Higgins, M. S. and R. W. Stewart, Radiation stresses in water waves; a physical discussion, with applications, *Deep-Sea Res.*, **11**, 529-562, 1964.

McGill, P., D. Neuhauser, D. Stakes, B. Romanowicz, T. Ramirez, and R. Uhrhammer, Deployment of a long-term broadband seafloor observatory in Monterey Bay, *Eos Trans. AGU*, **83** (47), Fall Meet. Suppl., F1008, 2002.

McGill, P. R., W. S. Wilcock, D. S. Stakes, A. H. Barclay, T. M. Ramirez, and D. R. Toomey, A long-term seismic array on the Endeavour segment of the Juan de Fuca ridge, *Eos Trans. AGU*, **84** (46), Fall Meet. Suppl., B12A-0748, 2003.

McGill, P. R., D. S. Stakes, T. M. Ramirez, W. S. Wilcock, A. H. Barclay, D. R. Toomey, D. T. Durant, E. E. Hooft, T. L. Mulder, and J. P. Ristau, First results from the deployment of a buried broadband seismometer on the Endeavour segment of the Juan de Fuca ridge, *Eos Trans. AGU*, **85** (47), Fall Meet. Suppl., T21C-0546, 2004.

Montagner, J. P. and Y. Lancelot, Editors, Multidisciplinary observatories on the deep seafloor, Report of International Ocean Network Workshop, Marseille, France, 01/11-01/13, 1995, published by INSU/CNRS, IFREMER, ODP-France, 1995.

Montagner, J. P., B. Romanowicz, and J. F. Karczewski, A first step toward an oceanic geophysical observatory, *Eos Trans., AGU*, **75**, 150-151, 1994a.

Montagner, J. P., J. F. Karczewski, B. Romanowicz, S. Bouaricha, P. Lognonne, G. Roult, E. Stutzmann, J. L. Thirot, J. Brion, B. Dole, D. Fouassier, J.-C. Koenig, J. C. Savary, L. Floury, J. Dupond, A. Echardour, and H. Floc'h, The french pilot experiment OFM-SISMOBS: first scientific results on noise level and event detection, *Phys. Earth Planet. Inter.*, **84**, 321-336, 1994b.

Munk, W. H., Surf beats, *Eos Trans. AGU*, **30**, 849-854, 1949.

Nakamura, Y., A method for dynamic characteristics estimation of subsurface using microtremor on the ground surface, *Q. Rep. Railway Tech. Res. Inst. Tokyo*, **30**, 25-33, 1989.

Okihiro, M. and R. T. Guza, Infragravity energy modulation by tides, *J. Geophys. Res.*, **100**, 16,143-16,148, 1995.

Olsen, K. B. and G. T. Schuster, Causes of low-frequency ground motion amplification in the Salt Lake Basin: the case of the vertically incident P wave, *Geophys. J. Int.*, **122**, 1045-1061, 1995.

Olsen, K. B., J. C. Pechmann, and G.T. Schuster, Simulation of 3D elastic wave propagation in the Salt Lake Basin, *Bull. Seism. Soc. Am.*, **85**, 1688-1710, 1995.

OMD Workshop Committee, Ocean Mantle Dynamics Implementation Plan, Report of a Community Workshop, Snowbird, Utah, 18-20 September 2002, 2003.

Peterson, J., Observation and modeling of seismic background noise, *U. S. Geol. Surv. Tech. Rept.*, **93-322**, 1-95, 1993.

Pitarka, A., K. Irikura, T. Iwata, and T. Kagawa, Basin structure effects in the Kobe are inferred from the modeling of ground motions from two aftershocks of the January 17, 1995, Hyogo-ken Nanbu earthquake, *J. Phys. Earth*, **44**, 563-576, 1996.

Pratt, T. L., T. M. Brocher, C. S. Weaver, K. C. Creager, C. M. Snelson, R. S. Crosson, K. C. Miller, and A. M. Tréhu, Amplification of seismic waves by the Seattle Basin, Washington State, *Bull. Seism. Soc. Am.*, **93**, 535-545, 2003.

Press, W. H., FORTRAN numerical recipes, Cambridge England, New York, NY, Cambridge University Press, 1999.

Purdy, M., Editor, Broadband Seismology in the Oceans: Towards a five year plan, Report of Ocean Seismic Network Workshop published by Joint Oceanographic Institutions, 1995.

Purdy, G. M. and A. M. Dziewonski, Proc. Workshop on Broad-Band Downhole Seismometers in the Deep Ocean, Woods Hole, MA, Apr. 26-28, 1988, Joint Oceanogr. Inst. and U.S. Sci. Advisory Comm., 1988.

Rhie, J. and B. Romanowicz, Excitation of Earth's continuous free oscillations by atmosphere-ocean-seafloor coupling, *Nature*, **431**, 552-556, 2004.

Rodgers, A., A. Petersson, S. Nilsson, B. Sjogreen, and K. McCandless, Ground predictions using the USGS seismic velocity model of the San Francisco Bay Area: Evaluating the model and scenario earthquake predictions, *Seism. Res. Lett.*, **77**, 281, 2006.

Romanowicz, B., D. Neuhauser, B. Bogaert, and D. Oppenheimer, Accessing Northern California Earthquake Data Via Internet, *Eos Trans., AGU*, **75**, 258-261, 1994.

Romanowicz, B., D. Stakes, D. Dolenc, D. Neuhauser, P. McGill, R. Uhrhammer, and T. Ramirez, The Monterey Bay broadband ocean bottom seismic observatory, *Ann. Geophys.*, 2006 (in press).

Romanowicz, B., D. Stakes, J. P. Montagner, P. Tarits, R. Uhrhammer, M. Begnaud, E. Stutzmann, M. Pasyanos, J.-F. Karczewski, S. Etchemendy, and D. Neuhauser, MOISE: A pilot experiment towards long term sea-floor geophysical observatories, *Earth Planets Space*, **50**, 927-937, 1998.

Romanowicz, B., D. Stakes, R. Uhrhammer, P. McGill, D. Neuhauser, T. Ramirez, and D. Dolenc, The MOBB Experiment: A prototype permanent off-shore ocean bottom broadband station, *Eos Trans., AGU*, **84** (34), 325, 331-332, 2003.

Schulte-Pelkum, V., P. S. Earle, and F. L. Vernon, Strong directivity of ocean-generated seismic noise, *Geochem., Geophys., Geosys.*, **5** (3), 1-13, doi:10.1029/2003GC000520, 2004.

Schwartz, D. P., D. Pantosti, K. Okumura, T. J. Powers, and J. C. Hamilton, Paleoseismic investigations in the Santa Cruz mountains, California: Implications for recurrence of large-magnitude earthquakes on the San Andreas fault, *J. Geophys. Res.*, **103**, 17,985-18,001, 1998.

Simila, G. W., V. A. Gallardo, K. C. McNally, M. L. Begnaud, and D. S. Stakes, New investigation of significant Monterey Bay area earthquakes (M>4.0, 1926-79) utilizing data from a 1998 deployment of PASSCAL Ref-Teks and master-event methods, *Eos Trans., AGU*, **79** (45), F589, 1998.

Snodgrass, F. E., G. W. Groves, K. F. Hasselmann, G. R. Miller, W. H. Munk, and W. H. Powers, Propagation of ocean swell across the Pacific, *Philos. Trans. R. Soc. London, Ser. A.*, **259**, 431-497, 1966.

Stakes, D., B. Romanowicz, J. P. Montagner, P. Tarits, J. F. Karczewski, S. Etchemendy, D. Neuhauser, P. McGill, J.-C. Koenig, J. Savary, M. Begnaud, and M. Pasyanos, MOISE: Monterey Bay Ocean Bottom International Seismic Experiment, *Eos Trans., AGU*, **79**, 301-309, 1998.

Stephen, R. A., F. N. Spiess, J. A. Collins, J. A. Hildebrand, J. A. Orcutt, K. R. Peal, F. L. Vernon, and F. B. Wooding, Ocean seismic network pilot experiment, *Geoch., Geophys., Geosyst*, **4** (10), 1-38, doi:10.1029/2002GC000485, 2003.

Stidham, C., Three-dimensional crustal structure influences on wave propagation and generation of strong ground motion in the greater San Francisco Bay region, *Ph.D. Thesis*, University of California, Berkeley, 1999.

Stidham, C., M. Antolik, D. Dreger, S. Larsen, and B. Romanowicz, Three-dimensional structure influences on the strong-motion wavefield of the 1989 Loma Prieta earthquake, *Bull. Seism. Soc. Am.*, **89**, 1184-1202, 1999.

Stutzmann, E., J.-P. Montagner, A. Sebai, W. C. Crawford, J.-L. Thirot, P. Tarits, D. Stakes, B. Romanowicz, J.-F. Karczewski, J.-C. Koenig, J. Savary, D. Neuhauser, and S. Etchemendy, MOISE: A prototype multiparameter ocean-bottom station, *Bull. Seism. Soc. Am.*, **91**, 885-892, 2001.

Sutton, G. H., F. K. Duennebier, and B. Iwataki, Coupling of ocean bottom seismometers to soft bottom, *Mar. Geophys. Res.*, **5**, 35-51, 1981.

Sutton, G. H., W. G. McDonald, D. D. Prentiss, and S. N. Thanos, Ocean-bottom seismic observatories, *Proc. IEEE*, **53**, 1909-1921, 1965.

Suyehiro, K., T. Kanazawa, N. Hirata, M. Shinohara, and H. Kinoshita, Broadband downhole digital seismometer experiment at site 794, Proc. O.D.P. 127/128, 1061-1073, 1992.

Suyehiro, K., J. P. Montagner, A. M. Dziewonski, and B. Romanowicz, The International Ocean Network Structure, Proceedings ION/ODP International Workshop, "Multidisciplinary observatories on the deep seafloor", Marseille, 61-72, 1995.

Suyehiro, K., E. Araki, S. Amasao, and T. Kanazawa, Deep sea borehole observatories ready and capturing seismic waves in the western Pacific, *Eos Trans., AGU*, **83**, 624-625, 2002.

Tanimoto, T., The oceanic excitation hypothesis for the continuous oscillation of the Earth, *Geophys. J. Int.*, **160**, 276-288, 2005.

Thatcher, W., G. Marshall, and M. Lisowski, Resolution of fault slip along the 470-km-long rupture of the great 1906 San Francisco earthquake and its implications, *J. Geophys. Res.*, **102**, 535-5367, 1997.

Tu, T., D. O'Hallaron, and J. Lopez, The Etree Library: A system for manipulating large octrees on disk, *School of Computer Science, Carnegie Mellon University, Technical Report CMU-CS-03-174*, 2003.

Tucker, M. J., Surf beats: Sea waves of 1 to 5 min. period, *Proc. R. Soc. London, Ser. A*, **202**, 565-573, 1950.

Uhrhammer, R., B. Romanowicz, D. Neuhauser, D. Stakes, P. McGill and T. Ramirez, Instrument testing and first results from the MOBB Observatory, *Eos Trans., AGU*, **83** (47), Fall Meet. Suppl., F1008, 2002.

Uhrhammer, R. A., D. Dolenc, B. Romanowicz, D. Stakes, P. McGill, D. Neuhauser, and T. Ramirez, MOBB: Data analysis from an ocean floor broadband seismic observatory, *Eos Trans., AGU*, **84** (46), Fall Meet. Suppl., F1137, 2003.

von Seht, M. I., and J. Wohlenberg, Microtremor measurements used to map thickness of soft sediments, *Bull. Seism. Soc. Am.*, **89**, 250-259, 1999.

Warburton, R. J. and J. M. Goodkind, The influence of barometric pressure variations on gravity, *Geophys. J. R. Astr. Soc.*, **48**, 3, 281-292, 1977.

Webb, S. C., Long-period acoustic and seismic measurements and ocean floor currents, *IEEE J. Ocean Eng.*, **13**, 4, 263-270, 1988.

Webb, S. C., The equilibrium microseism spectrum, *J. Acoust. Soc. Am.*, **92**, 2141-2158, 1992.

Webb, S. C., Broadband seismology and noise under the ocean, *Rev. Geophys.*, **36**, 105-142, 1998.

Webb, S. C. and W. C. Crawford, Long-period seafloor seismology and deformation under ocean waves, *Bull. Seism. Soc. Am.*, **89**, 1535-1542, 1999.

Webb, S. C., X. Zhang, and W. Crawford, Infragravity waves in the deep ocean, *J. Geophys. Res.*, **96**, 2723-2736, 1991.

Wentworth, C. M., T. E. Fumal, T. M. Brocher, and E. E. Brabb, The areal distribution of geologic materials and their seismic velocities, San Francisco Bay area, California, *EOS Trans. AGU.*, **78**, F436, 1997.

Wilcock, W. S., A. H. Barclay, P. R. McGill, D. S. Stakes, T. M. Ramirez, D. R. Toomey, D. T. Durant, E. E. Hooft, T. L. Mulder, and J. P. Ristau, Local earthquakes on the Endeavour segment of the Juan de Fuca ridge: First seismic results from the Keck seismic/hydrothermal observatory, *Eos Trans. AGU*, **85** (47), Fall Meet. Suppl., B13A-0180, 2004.

Working Group on Northern California Earthquake Potential, Database of potential sources for earthquakes larger than magnitude 6 in northern California, *U.S. Geol. Surv. Open-File Report 96-705*, 1996.

Working Group on California Earthquake Probabilities, Earthquake probabilities in the San Francisco Bay region: 2002-2031, *U.S. Geol. Surv. Open-File Report 03-214*, 2003.

Yamanaka, H., M. Takemura, H. Ishida, and M. Niwa, Characteristics of long-period microtremors and their applicability in exploration of deep sedimentary layers, *Bull. Seism. Soc. Am.*, **84**, 1831-1841, 1994.

Zürn, W. and R. Widmer, On noise reduction in vertical seismic records below 2 mHz using local barometric pressure, *Geophys. Res. Lett.*, **22**, 3537-3540, 1995.